AN ABSTRACT OF THE DISSERTATION OF

Nisha Puri for the degree of Doctor of Philosophy in Civil Engineering presented on June 3, 2019.

Title: Progress Monitoring and Quality Assessment/Quality Control of Construction Projects using Lidar and BIM.

Abstract approved: _____

Yelda Turkan

The construction industry is a key contributor to the Gross Domestic Product (GDP) of many countries around the world and is valued at more than $10 trillion globally. Schedule, cost and quality are the main performance measures of construction projects. The primary goal for project stakeholders in the construction industry is to ensure that a project is delivered on time and on budget, while meeting the project specific quality standards. However, cost and schedule overruns, and rework have become the costly standard for most construction projects. In particular, transportation construction projects are very sensitive to cost and schedule overruns due to the magnitude of risk and uncertainty involved. The inaccuracies, inconsistencies, and delays associated with manual collection of project progress data further contribute to the inefficient tracking of resources, activities, and cost, consequently causing issues to be overlooked and leaving them unresolved. Another major issue in the construction industry is related to the assessment of the quality of work in a timely fashion in order to avoid rework. Focusing on measuring the quality of concrete slabs, several concrete surface waviness assessment methods have been developed to overcome the disadvantages of one assessment method over the other. Floor surface waviness assessment over multiple

one-dimensional (1D)-survey lines may not accurately reflect the actual condition or waviness of an entire floor. Thus, it can be concluded that the current practices for performing project quality control and progress tracking are prone to errors, labor-intensive, and time-consuming, and there is a need to develop novel, technology supplemented methodologies to improve current project quality control and progress tracking practices.

This dissertation proposes two technology-supplemented frameworks for project progress tracking and dimensional quality control, and is comprised of three manuscripts. The first manuscript presents a framework that uses mobile lidar data and four dimensional- (4D-) design models for tracking the progress of bridge construction projects. The framework is capable of determining the completion of individual bridge elements in an accurate and efficient manner, and the progress information is reported as Percentage of Completion (POC). The second manuscript presents a framework that enables assessment of a concrete surface in two-dimensional (2D) domain using the synergy between Terrestrial Laser Scanning (TLS) and Continuous Wavelet Transform (CWT). 2D CWT analysis provides information not only about the periods of the surface undulations, but also the location of such undulations. The third manuscript presents a sensitivity analysis of the impact of various TLS point cloud scanning resolutions on surface waviness results. Furthermore, the surface waviness results obtained using TLS and Unmanned Aerial Vehicles (UAV)-based laser scanning are compared and analyzed.

Progress Monitoring and Quality Assessment/Quality Control of Construction Projects using Lidar data and BIM

by

Nisha Puri

A DISSERTATION

submitted to

Oregon State University

in partial fulfillment of
the requirements for the
degree of

Doctor of Philosophy

Presented June 3, 2019
Commencement June 2019

Doctor of Philosophy dissertation of Nisha Puri presented on June 3, 2019

APPROVED:

Major Professor, representing Civil Engineering

Head of the School of Civil and Construction Engineering

Dean of the Graduate School

I understand that my dissertation will become part of the permanent collection of Oregon State University libraries. My signature below authorizes release of my dissertation to any reader upon request.

Nisha Puri, Author

ACKNOWLEDGEMENTS

I would not have made it this far without the love, support, guidance and mentorship of several individuals throughout this four-year journey and would like to express my sincere gratitude towards them. First, I would like to thank my advisor, mentor and friend, Professor Yelda Turkan, for her mentorship and for providing me with an enriching research experience. I truly appreciate her guidance, support and tremendous patience during this learning process. I will forever cherish our outdoor adventures in Oregon. She is my role model and I aspire to become like her.

I would also like to thank Professor John Gambatese and Professor Michael Olsen for their invaluable mentorship and guidance, without which I would not have come this far. I would like to thank my minor advisor, Professor Sinisa Todorovic for instilling a sense of confidence in me and for encouraging me to push my boundaries. I would also like to thank Professor Prasad Tadepalli for his valuable time and support.

I would like to acknowledge the funding from Oregon Department of Transportation (ODOT) Project SPR-811 and the agreement with ODOT that provided the mobile lidar to OSU. I would like to acknowledge the support of Leica Geosystems for providing the equipment and software used in this research as well. I would also like to thank the NSF's NHERI RAPID facility for their help and cooperation in data collection.

I would like to thank Andrew Senogles, Chase Simpson, Erzhuo Che, Jake Dafni, Marian Jamieson and Wylie Ferron for their valuable time in helping me with data collection. I would like to thank Erzhuo also for providing with the code for subsampling point clouds that was used for the analysis included in Chapter 6.

I am grateful to my colleagues in the School of Civil and Construction engineering for their friendship, encouragement and support. I would like to thank my Nepali friends for being my family away from home. I will cherish our memories and the time we spent together.

No words can express the love and support from a family. I thank my parents for giving me the gift of life. I acknowledge my strong and wonderful mother for always inspiring me to be brave. I thank her for making me the person I am today. My parents have taught me things no person, no book or experiences will ever teach me. I acknowledge my brother, Manish, for being my closest friend and mentor, and for always putting a smile on my face when I needed it the most.

Finally, I thank Ashrant Aryal, for an incredible friendship. His virtue inspires me to improve myself each day and I am grateful to be his girlfriend. I thank him for always being here by my side through it all. I treasure our almost decade-long relationship, and hope that it has a wonderful future in store for us.

CONTRIBUTION OF AUTHORS

Chapter 4 is based on the research conducted for ODOT research project SPR #811: Project Progress Tracking Using Lidar And 4D Information Models. Dr. Michael J. Olsen and Dr. John A. Gambatese provided their invaluable guidance for completing this project.

Dr. Frédéric Bosché and Dr. Enrique Valero provided their invaluable suggestions for improving the paper, and assisted with the data processing and writing in section 5.3.3.2 in Chapter 5.

TABLE OF CONTENTS

Page

TABLE OF CONTENTS (Continued)

Page

TABLE OF CONTENTS (Continued)

Page

TABLE OF CONTENTS (Continued)

Page

LIST OF FIGURES

Figure Page

LIST OF FIGURES (Continued)

Figure Page

LIST OF FIGURES (Continued)

Figure Page

LIST OF FIGURES (Continued)

Figure Page

LIST OF TABLES

Table Page

LIST OF APPENDIX FIGURES

Table Page

LIST OF APPENDIX TABLES

Table Page

LIST OF APPENDIX TABLES (Continued)

Table Page

LIST OF APPENDIX TABLES (Continued)

Table Page

DEDICATION

I dedicate this dissertation to my family. I hope I can continue to make you happy and proud. I think of you, always.

Executive Summary

Emerging technologies are transforming several industries with improvements in product quality, increase in production rates and reduction in long-term costs. The construction industry is also increasingly adopting novel technologies and new construction techniques to improve productivity and efficiency of construction practices. The integration of these tools and technologies into construction practices is speeding up the process of digitalization in the construction industry. The potential impact resulting from introducing various innovative tools and technologies into existing construction practices can be broadened if efficient methodologies are designed for their implementation in various areas. In fact, the Construction Industry Institute (CII) [1] and the National Research Council (NRC) of the National Academies [2] have emphasized the identification and prioritization of technology-centric solutions to advance productivity and increase efficiency in the construction industry. In 2017, the McKinsey Global Institute reported that there is a correlation between the level of digitalization and the productivity increase in several sectors [3]. Furthermore, a number of unique challenges arising in the construction industry due to the increasing complexity of construction projects has necessitated the integration of information technology into traditional construction practices.

The construction industry is a key contributor to the Gross Domestic Product (GDP) of several countries and is valued at more than $10 trillion globally [4]. With schedule, cost and quality as the main performance measures of construction projects, the primary goal for project stakeholders in the construction industry is to ensure that a project is delivered on time and on budget, while meeting the project specific quality standards. However, cost and schedule overruns, and rework have become the standard for most construction projects. In fact, according to Klynveld Peat Marwick Goerdeler's (KPMG's) 2015 Global Construction Survey, only 25% of projects were completed within 10% of the specified deadlines, and 31% of projects were completed within 10% of the budget. Similarly, repair,

demolition, removal, and replacement of defective concrete elements entail costs that could amount to as much as 12% of the project contract value [5–8].

Accurate as-built data collected from on-going construction projects assists project field engineers with tracking the progress of construction work. The comparison of as-planned status against the as-built status of construction enables the involved parties to determine project performance. Periodic monitoring of project performance enables timely identification of discrepancies between the schedule baseline and the actual project schedule. The rapid identification of any discrepancies allows necessary measures to be taken to minimize the impact of a delay on the construction workflow. In transportation projects, the traditional means of acquiring as-built data from a construction site prevents involved parties from receiving the required information from the site in a timely manner. The delay in the communication of information ultimately causes subsequent delays in implementing necessary courses of action targeted toward improving the workflow. Similarly, failure to communicate project performance with all involved parties in an effective and timely manner lead to delays and cost-overruns in construction work [9]. Furthermore, manually collected progress tracking information may not be readily available for analyzing project performance. Thus, it can be concluded that the traditional methods of measuring progress in transportation projects are inconsistent and prone to error. While the use of light detection and ranging (lidar) and BIM for progress monitoring in vertical construction projects has been investigated by several researchers [10]–[19], previous frameworks developed for building construction are not directly applicable to horizontal construction projects due to the differences in the physical design and construction methods between building and horizontal construction projects. The implementation of such frameworks in horizontal construction projects may not necessarily provide accurate progress information. The majority of the previously developed progress tracking frameworks deliver object detection results for completed construction components in terms of Boolean variables. In other words, in a given time frame, a component in the building structure is reported as either fully constructed or not constructed. In practice, the completion status of some components requires to be reported

in terms of percentage of completion (POC). For instance, in bridge replacement projects, it is a common practice to have one of the lanes operating while construction work proceeds on the other lane. This practice may result in only a section of the bridge deck being completed, as opposed to the entire deck. In such a scenario, an accurate progress report would reflect the progress of the bridge deck placement in terms of POC. In addition, a progress tracking framework for such projects should take the formwork placed into account for partially completed elements. Furthermore, road construction projects may consist of several design layers, and the progress of these layered surfaces should also be reported. Misclassification of road design layers can potentially arise from registration errors, which needs to be addressed.

One of the other major difficulties in the construction industry is related to the quality assessment of work in a timely fashion in order to avoid rework. The primary causes of rework include poor workmanship, failure to detect the imperfections in newly constructed surfaces during the early stages of construction, and lack of timely communication [20]. The traditional processes of performing quality control and progress tracking are labor-intensive and time-consuming. Focusing on measuring the quality of concrete slabs, several concrete surface waviness assessment methods have been developed to overcome the disadvantages of one assessment method over the other. For example, the F-number method was developed to overcome the disadvantages of the Straightedge method, and the Waviness Index (WI) method was developed to overcome the disadvantages of the F-number method. The sparseness of measurements associated with each of these methods prevents from achieving a better understanding of how elevations and undulations change across the surface. Assessing waviness over multiple one-dimensional (1D)-survey lines, as is done with traditional methods, may not accurately reflect the actual condition or waviness of the entire floor. Using 3D point clouds obtained using terrestrial laser scanning (TLS) and as-designed geometry information from Building Information Modelling (BIM), Bosché and Guenet [21] developed an approach based on BIM and TLS data to assess whether the geometry of as-is elements adhere to the specified surface flatness tolerances. An experiment was conducted to compare the results obtained using the proposed method

with the ones obtained from the digitally encoded Straightedge and F-number methods. The digital application of Straightedge and F-Number, as presented in [18], significantly reduces the time required for data collection and analysis, compared to traditional methods. However, in current practice, surface flatness is analyzed along sparsely surveyed 1D survey lines, which delivers results limited in spatial and wavelength resolution. Bosché and Biotteau [22] developed a method that applied 1D Continuous Wavelet Transform (CWT) to TLS data to characterize surface undulation periods, which addresses the limitation of previous works in wavelength resolution, i.e. the approach examines surface waviness at a wider range of wavelengths or characteristic periods. However, it remains based on measurements along 1D lines that do not enable an analysis of flatness in all possible directions, and provide results with limited spatial resolution.

The first study in this dissertation, Chapter 4, discusses a technology-supplemented progress monitoring approach. The main research question for the study was 'How can we report the progress of horizontal construction projects in terms of percentage of completion?' To answer this question, a framework was designed and tested using the data collected from a bridge construction project near Albany, Oregon. The framework implements as-built data obtained using mobile lidar technology, which enables rapid collection of data while ensuring the safety of the data collector. The proposed framework utilizes point cloud data and 4D design models to identify deviations of the performed work from the planned work. The framework was tested using as-built data acquired from an on-going bridge construction project, and Percentage of Completion (POC) for the as-built bridge elements are calculated and compared with the as-planned POC. The differences between these two POC values for each element, on a particular scan date, are used for assessing the performance of the proposed framework. The difference between as-built and as-planned POC values ranged from -7% to 6% for most elements, which shows that the developed framework enables tracking the completion of individual bridge elements in an accurate and efficient manner.

The second study in this dissertation is described in Chapter 5. The main research question this study attempts to answer is ‘How can the traditional methods of measuring surface waviness along 1D lines be extended to measuring surface flatness along the 2D surface and provide a more comprehensive assessment of surface geometry?’. The methodology presented in Chapter 5 presents a compliance-checking algorithm for detecting elements where their dimensions exceed specified construction tolerances. It also enables assessment of a concrete surface in 2D using the synergy between TLS and CWT analysis. 2D CWT analysis provides information not only about the periods of the surface undulations, but also the location of such undulations. The validity of the methodology is established by running a test on point clouds obtained from a warehouse project near Gresham, Oregon. A rigorous comparison between one of the existing floor waviness measurement methods, the waviness index method, and the proposed method is made. The results showed that the proposed methodology delivers accurate results that enable the localization of surface undulations of various characteristic periods.

Chapter 6 presents a comparative analysis of floor waviness measurement results obtained using UAV-based (mounted with a 3D laser scanning sensor) and TLS-based technologies. One of the major drawbacks in using 3D dense point clouds is related to storing and processing large volumes of point cloud data. Using lower resolution settings during scanning can save time and cost. However, a sensitivity analysis is required to understand the data quality requirements for localization of surface defects. The main research question for this study is ‘How does the resolution of point clouds affect the localization of surface defects?’ The TLS data from two projects are used to investigate how the quality of surface waviness results are affected by the scanning resolution. The point cloud data were analyzed at scanning resolutions of 0.02°, 0.04°, 0.06°, 0.08° and 0.1°, which are typical resolution settings for most commercially available TLS systems. The findings showed that for the Magruder Hall Expansion Project, using only one scan (in our case Scan 2) ensured that the CWT results matched the ground truth results, for scanning resolutions ranging from 0.02° through 0.08°. If scans are collected from two scanning locations, scanning resolutions ranging from 0.02° through 0.1° can be used. Each of the

scanning locations for the two scans may be as far as 12.46 m from the furthest point in the slab. Table 6.3 shows that this distance could have been 18.5 m but a conservative distance was chosen to ensure accurate results. Note that the scanner is setup within the boundaries of the slab surface. The results from the Vista Logistic Park Project has shown that using four scans (in our case Scan 1, Scan 2, Scan 3 and Scan 4) ensured that the CWT results matched the ground truth results for scanning resolutions ranging from 0.02° through 0.08°. Each of the scanning locations for the four scans may be as far as 22.69 m from the furthest point in the slab. Note that the scanner is setup within the boundaries of the slab surface. Furthermore, the results obtained from analyzing UAV-based point cloud data and TLS point cloud data for measuring floor flatness shows that comparable results are obtained for the scales of 30, 60 and 75. However, UAV-based point cloud did not produce acceptable results for scales of 15 and 30. Thus, it was concluded that UAV-based point cloud data on its own does not ensure localization of all kinds of surface undulations and TLS should be the preferred choice.

Chapter 7 summarizes the results of the three studies described in the dissertation. The research questions defined in Chapter 3 for each research study are validated, and limitations are discussed. In summary, two novel technology-centric frameworks have been developed to overcome the disadvantages associated with traditional methods of progress tracking and dimensional quality control. A framework that utilizes the synergy between lidar and BIM technologies to precisely track the progress of construction projects is developed. Another framework based on lidar technology is designed to implement 3D geometric information obtained from construction sites and provide information that supports dimensional quality control processes. Furthermore, sensitivity analysis was performed to analyze the surface waviness results obtained from point clouds with different resolutions. A comparison between surface waviness results obtained using TLS and UAV-based point clouds was also performed. Chapter 7 provides conclusions for the studies performed in this dissertation. Future research directions are also discussed.

1 Introduction and Motivation

1.1 Progress Tracking in the Construction Industry

The investment in transportation infrastructure in the United States is estimated to reach $278.1 billion in 2019 [23]. Every four years, the American Society of Civil Engineers (ASCE) releases a comprehensive assessment of the U.S. infrastructure as a “report card”. The most recent report card that ASCE published in 2017 issued an overall grade of D+ (poor) for the nation’s infrastructure, and C+ (mediocre) for bridges. The report estimated that 188 million trips were taken daily across deteriorating roads, bridges and highways [24]. Based on their assessment, the current state of transportation infrastructure resulted in increased travel times and a number of accidents on roads [25]. Ultimately, these conditions has a negative impact on the cost of delivered goods and personal income [25]. Frequent inspection of existing transportation infrastructure and performing necessary repair work in a timely manner can ensure good conditions of roads and bridges. In addition to performing comprehensive inspections regularly after the construction phase, proper measures implemented during the construction phase also help ensure good quality. During the pre-construction phase, the various parties involved in a project collectively define the milestones of the project based on the expected duration of completion and the available budget. Under the constant pressure of completing the required work within a given time period while monitoring the available budget, the quality of work performed may be compromised [26]. Transportation construction projects often experience significant cost overruns and schedule delays [27]–[29]. In addition, failure to communicate the project performance with all involved parties in an effective and timely manner may lead to delays and cost-overruns in construction work [9].

Systematic collection of accurate and detailed data from on-going construction projects is important for monitoring project progress. The acquired data can be processed to generate information about the status of completion of various activities. This information can be used by various parties involved in the project for decision-making and to find effective solutions to overcome any delays. Timely identification of construction delays is possible if such information is collected frequently and with sufficient detail from the construction site. Construction progress monitoring is traditionally a labor-intensive process. Foreman daily or weekly reports are primarily used to record the amount of work performed on site. While such reports are versatile and provide several types of information including the availability of resources, potential risks, inventory checklists and incidents occurred, they fail to capture three-dimensional (3D) geometric information of the work that has been completed. Obtaining 3D geometric information is a crucial component of a progress monitoring process as it ensures that the information collected regarding the as-built status is not subjective. 3D geometric information serves as a mirror of the work that has been completed on site within a certain period of time. Moreover, substantial delays may be experienced before foremen daily or weekly reports are analyzed and any important information is relayed to concerned parties. The overall process may prevent corrective actions from taking place in a timely manner and contribute toward schedule delays. Thus, it is essential that such reports are supplemented, if not replaced, with as-built 3D geometric information to minimize the delays occurring in a construction project.

Obtaining reliable progress information pertaining to on-site activities would enable identification of issues that may cause delays in the completion of these activities. Progress information acquired using current manual-based progress measurement workflows are prone to errors and are time consuming [30]. Additionally, multiple site visits may be required if the collected data is inaccurate or incomplete. Therefore, the inefficiencies associated with manual-based progress measurement methods indicates the need for adopting new technologies for project progress monitoring.

1.2 Dimensional Quality Control in the Construction Industry

As-built dimensions of cast-in-place concrete elements often differ from the dimensions originally specified in as-designed plans [31]. Dimensional Quality Control (QC) verifies that elements are constructed in compliance with the specified dimensional tolerances. For instance, when combining precast and cast-in-place elements, checking dimensional tolerance of all elements is necessary for ensuring acceptable performance of joints and interfacing materials [32]. In addition, failure to detect the imperfections in newly constructed surfaces during the earlier stages of construction causes delays in carrying out necessary repair works [20]. The repair, demolition, removal and replacement of defective concrete elements entail additional costs that could amount to as much as 12% of the project contract value [3-6]. Thus, upon the completion of concrete elements, it is crucial to carry out inspections in a timely manner. Furthermore, traditional inspection procedures related to dimensional QC are labor intensive and time consuming.

Focusing on concrete slabs, several factors influence the dimensional quality of cast-in-place concrete slabs, such as sweltering temperatures, placement and finishing techniques that are applied during construction. Proper regulation and control of these factors are essential for achieving specified levels of waviness and levelness. The defects resulting from the waviness of concrete slabs not only create aesthetic issues but also affect the efficiency of lift trucks and very narrow aisle (VNA) vehicles. Even if waviness present in slabs is not immediately noticeable, the waviness of the concrete slabs in industrial facilities, such as large warehouses, must be strictly examined since failing to detect waviness and deviations from the specified tolerances can greatly affect the operational activities that the floor is designed to handle [22]. Figure 1.1 illustrates how irregularities on the floor affect the stability of VNA trucks. Variations in elevation between the left and right wheels (d) of a VNA truck results in static lean (s) of VNA trucks. The static lean can potentially increase up to ten times due to the waviness present in concrete slabs [33].

$$\frac{d}{D} = \frac{s}{H} \rightarrow s = \frac{d \cdot H}{D}$$

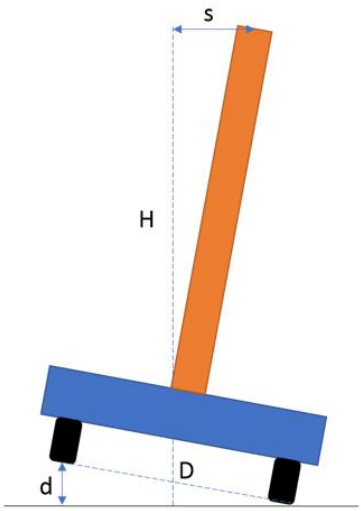

s - Static lean of a VNA truck in mm for D=1.2 m		d - Difference in elevation between the left and right wheels of a fork lift truck [mm]									
		3	4	5	6	7	8	9	10	11	12
H - height of racking [m]	6	15	20	25	30	35	40	45	50	55	60
	7	18	23	29	35	41	47	53	58	64	70
	8	20	27	33	40	47	53	60	67	73	80
	9	23	30	38	45	53	60	68	75	83	90
	10	25	33	42	50	58	67	75	83	92	100
	11	28	37	46	55	64	73	83	92	101	110
	12	30	40	50	60	70	80	90	100	110	120
	13	33	43	54	65	76	87	98	108	119	130
	14	35	47	58	70	82	93	105	117	128	140
	15	37	50	63	75	87	100	113	125	137	150
	16	40	53	67	80	93	107	120	133	147	160
	17	42	57	71	85	99	113	128	142	156	170
	18	45	60	75	90	105	120	135	150	165	180

Figure 1.1 The effect of difference in elevation between the wheels on the static lean for a VNA

The methods for measuring concrete slab waviness, which are currently prevalent in the construction industry, require intensive human intervention, are tedious and time-consuming, and yet are based on sparse measurements. These methods entail the surveying of 1D lines for differences in elevations and characterizing undulations of specific periods.

The Straightedge method involves laying a 10-ft (3.05 m) Straightedge across a survey line on the floor and measuring the distance between the Straightedge and the floor using a stainless steel slip gauge [31]. While the results obtained with this method are easily comprehensible, the process of laying out the Straightedge over large surface areas is labor-intensive and engenders random errors in the measurements [34]. In addition, this time-intensive method provides information about the deviations between as-built and as-designed points only at relatively few measured points.

The introduction of the F-numbers method was aimed towards eradicating random errors in measurements, via the use of instruments that enable measurement of elevation differences at fix intervals to produce more accurate results. It provides the results in the form of two numbers: Floor Flatness (FF) and Floor Levelness (FL). FF describes the

flatness associated with the measured floor surface point, whereas FL describes the levelness of the measured floor surface point. As described in the ASTM E1155-14 standard [35], the measurements are carried out at intervals of 1-ft along each survey line, and the measurements collected from multiple survey lines are statistically processed to generate FF and FL numbers that describe the conditions of the entire floor surface. In addition, results produced from the F-number method are in the form of flatness numbers (FF and FL values) that are hard to comprehend.

The Waviness Index (WI) method, as described in ASTM E1486-14 [36], was developed later because the F-number method provides information only about the floor undulations with periods of 1.5 to 4-ft (0.46 – 1.22 m) and 15 to 80-ft (4.6 – 24.4 m). In contrast, the WI method identifies various periods of floor undulations between 2-ft and 10-ft, which correspond to the periods of surface undulation that affect the operation of forklifts [37][22][38]. The results obtained using the WI method are expressed in inches and are relatively easier to comprehend.

Despite having a significant advantage over the Straightedge and the F-number methods, the WI method shares similar drawbacks with those methods. Sparse measurements yielded by the three methods fail to ensure that the collected data is an accurate representation of the geometric features of the surface. Although results may be repeatable with a certain error, they fail to capture the geometric details of the entire 2D floor surface and essentially do not impart information about the waviness of the 2D surface. Data collection from large surface areas using these methods demands significant amount of time and manual labor. Since these methods require measurement tools to be manually moved across the surface of the floor, the results obtained are prone to human error. Random errors, which potentially arise due to possible carelessness exerted while handling the measurement instruments, contribute toward inaccuracies in measurements. Moreover, the inability to retrieve similar results between different measurement sessions is one of the prominent drawbacks of these methods. And finally, applying these methods to measure the floor waviness of large floor areas, such as warehouse projects, is quite difficult. It is important

to note that warehouse projects typically have floor surface areas that are larger than 4,000 m2. Consequently, using these methods for such projects generate results that are not repeatable. In addition, the obtained results are limited in the orientation of the defects and the range of wavelength. Furthermore, the inability to explicitly reveal the location of those undulations remains a disadvantage for these methods [22].

1.3 Tolerance Issues in the Architecture, Engineering and Construction (AEC) Industry

There are a number of unique challenges arising in the construction industry due to the increasing complexity of construction projects, which has necessitated the integration of information technology into traditional construction practices. Building Information Modelling (BIM) is one of these technologies that has revolutionized the traditional ways of information retrieval and management in the construction industry [39][40][41]. BIM enables 3D parametric representation of building elements and facilitates "a more integrated design and construction process that results in better quality buildings at lower cost and reduced project duration [40]." In addition, the traditional way of using 2D drawings for documenting as-designed and/or as-built state of buildings are slowly being replaced by BIM [42]. The quality of as-built information acquired from project sites heavily affects the work that they are being used for. For the purposes of dimensional compliance checking and control as well as renovations, it is extremely important to have access to data that is very accurate. Terrestrial Laser Scanning (TLS) is a popular technology used in today's construction industry for acquiring accurate as-built information of the existing conditions [43][44][45][46].

In current practice, upon completion of a project, as part of quality control contract requirements, a contractor highlights the changes made during the construction on paper-based as-designed plans and submits them to the owner. Often, as-built plans of cast-in-place concrete elements fail to accurately reflect the geometrical attributes of elements that were originally specified in the as-designed plans [31]. Due to the changes made during

the construction phase, the dimensions and locations of an element specified in the as-designed plans may be different from the ones present in its as-built plan. Accordingly, it is impossible to perfectly align the as-built and as-designed plans with each other. However, potential rework as a result of those discrepancies can certainly be minimized by specifying appropriate tolerances, which would make construction work easier for contractors, superintendents, foremen and inspectors while help keeping project on schedule and within budget [47].

As-built information collected from construction projects is vital for decision making in various stages of a project's lifecycle including dimensional quality control and assessment [48][49][50], project progress monitoring [51][45][13] and facilities/asset management [52][53][54][55][41]. Renovation/restoration/remodeling activities require the use of as-built information to meticulously plan the dimensional features and locations of new installations and assign working groups accordingly. Modern non-contact based measurement systems enable capturing as-built data with millimeter level accuracy while decreasing the time required for data collection. An owner can heavily benefit from the accurate information about the discrepancies present between the as-built and as-designed models, which would help them assess dimensional tolerance compliance during construction. Accurate as-built 3D models can further be used for maintenance purposes and other possible future works during Operations and Maintenance (O&M) phase. At the same time, accurate as-built information could also support contractor's tasks during project closeout such as creating 2D drawings or 3D models as part of the submittal documents.

Various sources in the literature describe the failure design - construction integration as one of the prime reasons for such discrepancies [56][57][58] and focus on eliminating the sources of errors prior to construction. Several codes have been established to ensure the dimensional compliance of as-built elements, but it can be inferred that the defect can only be corrected after they occur [31]. Possible solutions for each perspective exist. In order to efficiently carry out post construction assessment, a tolerance compliance checking

framework could be devised. It has the advantage of carrying out timely and accurate measurements, but would not solve the core problem of why the problems exist in the first place. This approach could be extended to as-built modelling from available data to assess the existing conditions during renovation work involving removal of components or installation of new ones. A compliance checking framework could be devised so that prior to construction, owners, designers and contractors could establish acceptable tolerances, integrate that information in as-designed BIM, and then begin construction. This could help eliminate problems related to explicitly specified tolerance information on 2D paper-based plans and make the process easier by integrating all related information into a single digital platform.

The traditional way of using 2D drawings for documenting as-designed and/or as-built state of buildings are slowly being replaced by BIM [42]. The quality of as-built information acquired from project sites heavily affects the work that they are being used for. For the purposes of dimensional compliance checking and control as well as renovations, it is extremely important to have access to data that is very accurate. Terrestrial Laser Scanning (TLS) is a popular technology used in today's construction industry for acquiring accurate as-built information of the existing conditions [43][44][45][46].

In current practice, upon completion of a project, as part of quality control contract requirements, a contractor highlights the changes made during the construction on paper-based as-designed plans and submits them to the owner. Often, as-built plans of cast-in-place concrete elements fail to accurately reflect the geometrical attributes of elements that were originally specified in the as-designed plans [31]. Due to the changes made during the construction phase, the dimensions and locations of an element specified in the as-designed plans may be different from the ones present in its as-built plan. Accordingly, it is impossible to perfectly align the as-built and as-designed plans with each other. However, potential rework as a result of those discrepancies can certainly be minimized by specifying appropriate tolerances, which would make construction work easier for

contractors, superintendents, foremen and inspectors while help keeping project on schedule and within budget [47].

As-built information collected from construction projects is vital for decision making in various stages of a project's lifecycle including dimensional quality control and assessment [48][49][50], project progress monitoring [51][45][13] and facilities/asset management [52][53][54][55][41]. Renovation/restoration/remodeling activities require the use of as-built information to meticulously plan the dimensional features and locations of new installations and assign working groups accordingly. Modern non-contact based measurement systems enable capturing as-built data with millimeter level accuracy while decreasing the time required for data collection. An owner can heavily benefit from the accurate information about the discrepancies present between the as-built and as-designed models, which would help them assess dimensional tolerance compliance during construction. Accurate as-built 3D models can further be used for maintenance purposes and other possible future works during Operations and Maintenance (O&M) phase. At the same time, accurate as-built information could also support contractor's tasks during project closeout such as creating 2D drawings or 3D models as part of the submittal documents.

Various sources in the literature describe the failure in design - construction integration as one of the primary reasons for such discrepancies [56][57][58] and focus on eliminating the sources of errors prior to construction. Several codes have been established to ensure the dimensional compliance of as-built elements, but it can be inferred that the defect can only be corrected after they occur [31]. Possible solutions for each perspective exist. In order to efficiently carry out post construction assessment, a tolerance compliance checking framework could be devised. It has the advantage of carrying out timely and accurate measurements, but would not solve the core problem of why the problems exist in the first place. This approach could be extended to as-built modelling from available data to assess the existing conditions during renovation work involving removal of components or installation of new ones. A compliance checking framework could be

devised so that prior to construction, owners, designers and contractors could establish acceptable tolerances, integrate that information in as-designed BIM, and then begin construction. This could help eliminate problems related to explicitly specified tolerance information on 2D paper-based plans and make the process easier by integrating all related information into a single digital platform.

2 Background

2.1 Construction Progress Tracking

2.1.1 Progress Tracking in Vertical Construction Projects

Construction industry, compared to other non-farm industries, has been relatively slow in adopting new technologies and tools into its practices [59]. However, within the last decade, the construction industry has started adopting novel remote sensing and information technologies into its practices at a faster rate to increase the level of automation. The traditional way of recording as-built information and construction updates in highway construction projects is using Daily Work Reports (DWR) [60], which is time consuming and prone to errors. Therefore, several technologies including lidar, photogrammetry, radio-frequency identification (RFID), ultra-wideband (UWB) and BIM have been tested by several researchers for construction progress monitoring. The analysis of as-built data obtained using these technologies yields accurate progress information that is not subjective. In other words, progress information will not be misinterpreted by individuals based on their level of experience. UWB technology is commonly used for real-time location and orientation estimation in indoor and outdoor environments across various disciplines, mainly in the military and communications [61]. High accuracy localization is an important property of UWB technology, which enables UWB to be used for resource tracking. Teizer et al. [62] experimented with the applicability of the technology for tracking the location of individual steel beams in construction projects. The study concluded that UWB is an effective tool that can be used to monitor resources during the construction phase of a project. Furthermore, UWB technology was tested in real-life construction environment and the results showed that it is capable of delivering accurate positioning results in large and spacious outdoor environments [63]. Although such systems are capable of offering high precision positioning data, several factors have potentially hindered the widespread use of this technology for progress monitoring purposes. Systems using UWB technology have been commonly used for tracking

individual resources. On a construction site, it is impractical to use such tags on cast-in-place elements. In addition, the time required for the installation of such systems requires significant human effort, especially when used in large construction projects.

RFID is a wireless data collection system that is capable of uniquely identifying and tracking objects. It can be used in construction sites to automatically identify components that have been installed [64]. A study described in [65] developed a structural steel component tracking system called Comp-TRAK. The tracking system utilized RFID tags attached to components establish their location and orientation in the construction site. Similarly, Chin et al. [66] used RFID technology to correctly identify structural steel members prior to their installation at a given location. The data collected using RFID technology was integrated into 4D CAD to monitor the as-built status of the installation process. Similar to UWB, RFID technology enables tracking of a single component by providing single point coordinates for each element, and shares similar disadvantages, thus it is not practical to use them for monitoring the progress of cast-in-place concrete elements.

Capturing site photographs on a daily basis is one of the methods of recording as-built progress information. Traditionally, site photographs are collected and stored as a visual record of on-going progress. However, 2D information captured in these photographs fail to provide 3D geometric information about the as-built status of construction projects. Consequently, several research efforts have been directed toward processing the obtained photographs to generate 3D point clouds using photogrammetry and computer vision techniques together so that they can be compared with 3D design models and used for automated progress monitoring. Structure-from-Motion (SfM) is one of the most commonly used techniques for this purpose. Images are collected from a construction site on a daily basis using consumer grade [13] or UAV –mounted (Unmanned Aerial Vehicles-mounted) cameras [67][68]. The images are taken from various angles with 95% or more overlap to enable the creation of a 3D as-built point cloud model after applying SfM technique [69]. SfM technique can be used to extract 3D geometry information of the

elements of the structure of interest, as described in [13]. The approach involves identifying keypoints or interest points in a set of collected images. A keypoint detection algorithm, such as Scale Invariant Feature Transform (SIFT), can be used for detecting interest points. It is possible to obtain both the interest points and the descriptors associated with each of the points using the SIFT algorithm. The descriptor part is essential for correctly matching the detected interest points across images. Furthermore, in [13], the researchers used Random sample consensus (RANSAC) to refine the matching feature results by removing false matches. The intrinsic and extrinsic camera parameters are estimated and a 3D point cloud is reconstructed in the next step. The output point cloud data is aligned with the 4D information model (3D models combined with project schedule) to generate visual information about the on-going progress on site. This manual process can be significantly improved by using a Building Information Modelling (BIM) model to assist the existing SfM approach [70][71]. Photogrammetry offers significant advantages over previously discussed technologies for monitoring the construction progress of cast-in-place elements. It provides a 3D geometric representation of the construction site, and the progress monitoring results can be visualized in augmented reality environment [13]. Another study quantified the economic benefits of using high-resolution cameras for progress monitoring [72].

Lidar technology enables collection of 3D geometric information from a construction site at mm-level accuracy. The horizontal and vertical resolutions of the output scans can be specified in the TLS device before the scanning process. In addition, it is possible to control the density of the point cloud. Several studies have shown that TLS point clouds can be compared with 4D design BIM for project progress tracking [17][18][16][18]. The first step involves developing the 3D model using the 2D drawings if there is not a readily available 3D model of the structure of interest, and then the project schedule is linked to the 3D model, resulting in a 4D model. The 3D model and the point cloud data are then superimposed by performing a coarse registration. This step can be performed either manually [51][73] or by using a local region-based method [16]. The registration can be further tuned by using an Iterative Closed Point (ICP) algorithm before proceeding with

the object recognition step. The constructed elements are identified by applying an object-matching method to the aligned dataset, i.e. 3D design BIM and the as-built point cloud data [16][17]. In real work environments, the detection results may contain false positives or negatives due to the presence of occlusions, reinforcement bars or formwork. The method developed in [74][69] correctly classifies elements under such conditions. The actual progress completed can then be determined by computing the ratio of the actual work performed to the planned work. The obtained progress information can then be used to automatically update the as-planned schedule [16]. Lidar-based progress tracking methods have been well explored for the building construction projects. However, their application to monitoring horizontal construction projects has been limited and requires further investigation.

2.1.2 Progress Monitoring in Horizontal Construction Projects: CIM Practices

Technological advancements are constantly leveraged in academia and industry to develop innovative solutions to tackle inefficient construction practices. The adoption rate of technologies for improving construction processes is increasing exponentially in the vertical (building) construction industry. On the other hand, the horizontal construction industry is lagging behind in the adoption of various technologies into its practices. The Federal Highway Administration (FHWA) initiative known as Every Day Counts (EDC) encourages representatives from private industry, local governments and state transportation departments to promote new technologies and develop innovative solutions. The EDC-2 initiative was quite an important landmark as it promoted the use of 3D design models in an industry which predominantly relies on 2D paper-based drawings. Extending these efforts into the EDC-3 initiative, the use of 4D and 5D design models and lidar was encouraged for recording the as-built status of transportation projects. Several studies have focused on developing frameworks for mobile lidar data processing for transportation asset management and safety-related applications such as pavement segmentation [75], identifying crosswalks [76], road markings [77] and edges extraction [78] in mobile lidar point clouds automatically, and improving mobile lidar trajectory reconstruction and

segmentation [79]. The costs of integrating 3D models into project delivery processes for highway construction projects have also been have also examined [80]. The adaptation and implementation of a wide range of technologies to improve transportation construction processes is termed as Civil Integrated Management (CIM). In the light of several efforts and initiatives made to promote the use of technological tools and innovation, the adoption of such technologies in the horizontal construction industry increased by 180% from 2009 to 2012 [81].

2.1.3 Technologies used for as-built data collection

The adoption and implementation of various tools and technologies for improving construction practices is slowly gaining momentum in horizontal construction projects, compared to vertical construction projects. GPS, RFID sensors and photographs collected using UAV have been used to measure the productivity and monitor resources in transportation projects [82][83][84][85]. Similarly, the application of lidar technology is limited to measuring quantities of earthwork materials [86]. Vick and Brilakis [87] developed an approach for automatically detecting road design surfaces. The novel approach developed by the authors can be used for progress monitoring of road construction projects to improve project performance. The approach utilized UAV-derived images to obtain as-built data and a 3D BIM for obtaining as-planned information. It showed good performance when tested on unlabeled as-built point cloud. One of the drawbacks of this approach is that misclassification can be encountered in regions of wearing surface layer. Misclassification may occur if the registration error is larger than the thickness of the road design layers. In this scenario, the accuracy of detection can potentially be improved using lidar technology instead of UAV-derived images for as-built data collection.

While the efficacy of using lidar and BIM for progress monitoring in vertical construction projects has been validated by several researchers [10]–[19], the state-of-the-art frameworks developed in this pursuit remain to be tested on horizontal construction

projects. The adoption of such frameworks in horizontal construction projects may not necessarily provide accurate progress information. Most of the frameworks deliver object detection results for completed construction components in terms of Boolean functions. In other words, in a given time frame, a component in the building structure is reported as either fully constructed or not constructed. In practice, the completion status of some building components requires to be reported in terms of percentage of completion. For instance, in bridge replacement projects, it is a common practice to have one of the lanes operating while construction work proceeds on the other lane. This practice may result in only a section of the bridge deck being completed, as opposed to the entire deck. In such a scenario, an accurate progress report would reflect the progress of the bridge deck placement in terms of percentage of completion. In addition, a progress tracking framework for such projects should take the formwork placed into account for partially completed elements. In addition, misclassification of road design layers, which can potentially arise from registration errors, should be addressed in the framework.

2.2 Dimensional Quality Control: Surface Flatness Measurement using TLS

2.2.1 Dimensional Tolerances for Floor Flatness and Waviness

The dimensions of newly constructed and existing building elements can vary, slightly or significantly, from the dimensions specified in the design documents [31]. Tolerances, or allowable deviations in those dimensions, are typically specified during the design phase for different measures such as length, width, thickness, perpendicularity, or verticality. ACI 117-90 Standard Document, for example, provides a comprehensive list of tolerance criteria for cast-in-place concrete elements, such as vertical, lateral, and level alignments, and cross-sectional dimensions. The specified dimensional tolerances are an output of economical and practical considerations [88]. The role of QC inspectors is to ensure that the specified tolerance values are achieved as construction progresses. Inaccuracies in the geometry of concrete elements during construction arise from improper establishment of a

reference system for controlling the alignment, manual measurements, poor workmanship and in some cases, the method used for measurement [89].

2.2.2 Terrestrial Laser Scanning (TLS) Point Clouds for Project Control

Acquisition of accurate project as-built data is crucial for dimensional quality control measurements, so that informed decisions can be made in a timely manner. TLS is a modern surveying technology that has been gaining popularity increasingly in the Architectural, Engineering, Construction and Facilities Management (AEC&FM) industry. The versatility of the Terrestrial Laser Scanning (TLS) technology has been tested in various fields of AEC&FM. For example, TLS has been used for assessing the conditions of remote environments where human access is difficult or dangerous [90], for generating BIMs that represent the as-built conditions of building facilities [91], as well as construction progress control [15–19].

2.2.3 TLS Point Clouds for Quality Control

The use of TLS for dimensional QC is gaining interest due to its ability to rapidly provide inspectors with project as-built data in the form of both dense and accurate 3D point clouds (sub mm to mm-level accuracy) [93]. Using TLS not only solves the problems associated with accuracy and repeatability, but also enables the acquisition of data that represents the geometry of entire surfaces, thereby addressing the data sparsity limitations of existing surveying methods. Focusing on flatness measurement, compared to existing measurement tools employed in current standard flatness measurement methods, TLS thus offers an efficient way of collecting dense as-built data covering entire slab surface.

Regarding the processing of TLS data for QC, Fuchs et al. [94] and Shafer and Weber [95] developed deformation monitoring algorithms to find the differences in positions of TLS data points with respect to a reference surface. In [96], a color map generated from the TLS data was used to assess the flatness of facades in a multi-story building and the additional costs arising from placing excess mortar on these facades was evaluated based on the

volumetric quantities derived from TLS data. In [97], a methodology that identifies the geometric irregularities in precast concrete elements by comparing as-built data obtained from TLS and as-designed data obtained from BIM was developed. Tang et al. [8] developed three algorithms which helped in finding the difference in elevation of the points in the point cloud with respect to a plane taken from a BIM model or a plane specified by the user. The method described in [98] used an elevation map where each interval in height were represented with different colors. This approach represented the height of each point with respect to a reference plane obtained from a BIM model. All these methodologies and existing approaches detected areas where different degrees of deviations occurred, however they have failed to characterize the waviness or the periods of surface undulations.

2.2.4 Wavelet Transform for Surface Characterization

Wavelet Transform (WT) has a wide range of applications in engineering, some of which include seismic signal analysis [99], sound pattern analysis [100] and quantum mechanics [101]. WT is also widely used in the area of surface texture characterization, where it is used to break down the 2D profiles of surfaces into the roughness and waviness components [102]. WT has been applied to characterize surface roughness and waviness in several studies, and it has many applications in the field of point cloud processing such as point cloud de-noising and rock surface roughness quantification [31–33]. A technique using 1D WT for characterizing different types of surfaces was introduced by Chen et al. [106]. Josso et al. [107] performed 2D multi-scaled decomposition using images instead of profiles. Stępień and Makieła [108] applied 2D WT to analyze the deviations of cylindrical surfaces. Jiang et al. [109], Coiffman and Maggioni [110] and Hussein et al. [111] described the concepts of lifting wavelets and diffusion wavelets and used them for surface filtering. WT can be extended from 1D analysis to multi-dimensional signals as well [22][112]. Some applications of 2D CWT include characterizing the wavelengths of landslide areas and identifying the regions having high risk of landslides using topographic images [113]. Additional information about the different types of wavelets and the application of wavelet transform, can be found in [114] and [115]. And, as reviewed above,

the CWT has been previously suggested in [22] for use in construction surface flatness assessment.

2.2.5 Continuous Wavelet Transform and TLS for surface flatness measurement

The continuous wavelet transform (CWT) of a given function is the inner product of the function with the scaled and shifted versions of the mother wavelet [114]. The output of the inner product is the wavelet coefficient at a specific time or location and scale [115]. In order for a function, $\psi(t) \epsilon L^2(\mathbb{R})$, to qualify as a mother wavelet, it has to satisfy a condition known as the admissibility condition as stated below [116]:

$$0 < C\psi := \int_{-\infty}^{\infty} \frac{|\psi(\omega)|}{|\omega|} d\omega < \infty \quad (2.1)$$

where, C_ψ is the admissibility condition and ω is the angular (or radian) frequency.

This condition can also be written as [116]:

$$\Psi(0) = \int_{-\infty}^{\infty} \psi(t)dt = 0 \quad (2.2)$$

This implies that the function $\psi(t)$ has to move above and below the t-axis in a wave-like manner with decaying properties. Figure 2.1 demonstrates such properties with the example of a typical wavelet function commonly known as the Mexican Hat wavelet.

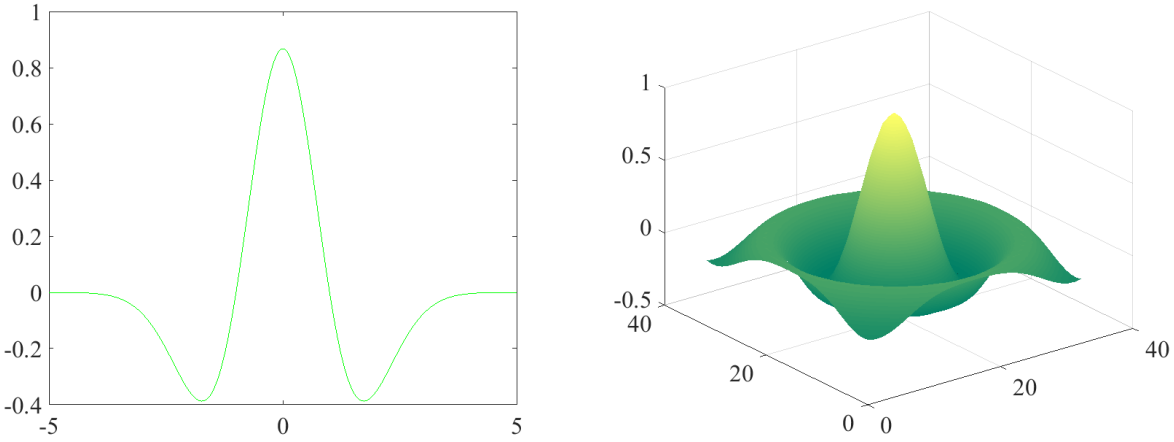

Figure 2.1 1D (left) and 2D (right) Mexican Hat Wavelet

CWT can be used to describe the time and frequency components of a temporal signal in detail. 1D CWT involves taking the original function and displaying the output function in terms of two variables, which are time and scale. The spectral information about a 2D signal for any scale s and location (x, y) is given by the 2D CWT [117], that is an extension of the 1D CWT and can be represented as follows [118]:

$$CWT\ (a,b,s) = \frac{1}{s}\int_{-\infty}^{\infty}\int_{-\infty}^{\infty} g(x,y)\,\psi_{abs}(x,y)\,dxdy \qquad (2.3)$$

where, $\psi_{abs}(x,y)$ is the mother wavelet, g(x,y) is the continuous 2D signal, s is the scale (dilating parameter) and (a,b) represents the location (translating parameter).

Different values of the translating and dilating parameters of the mother wavelet help in describing the different frequencies of undulations present in the surface [119]. The convolution of ψ and g provides the wavelengths (or periods) of the undulations present in the surface. The coefficients CWT (a, b, s) quantify the degree of correlation between the wavelet ψ and the function g at each point. In this way, apart from analyzing signals in time and frequency, the CWT can be extended to analyze signals, together in space and scale (space-scale analysis).

Different wavelets can be used as the mother wavelet to detect different types of undulations. The selection of an appropriate type of wavelet determines how efficiently the different components of a signal are extracted [120]. The geometric shapes of the wavelet is considered an important criteria when selecting the type of mother wavelet. The resemblance between the shape of the wavelet and the geometric features of a signal provides a cue for the selection of an appropriate wavelet. The defects present in as-built or as-is concrete surfaces resembles waves in the form of small bumps and dips, and the shape of 2D Mexican Hat wavelet closely resembles the shape of the surface undulations present on concrete surfaces, as shown in Figure 2.1. The Mexican Hat wavelet is a real and isotropic wavelet that is good for detecting contour features [121][122]. The use of

different values of the translation and scale parameters of the mother wavelet enable the detection of undulations corresponding to different characteristic periods in the point cloud data. Therefore, it is chosen as the mother wavelet in this study. 2D Mexican Hat wavelet in spatial domain is depicted as follows:

$$\psi(\mathrm{x,y}) = \frac{1}{2\pi}(2 - x^2 - y^2) * e^{-\frac{1}{2}(x^2+y^2)} \quad (2.4)$$

Using 3D point clouds obtained from TLS and as-designed geometry information from BIM, Bosché and Guenet [21] developed an approach based on BIM and TLS data to assess whether the geometry of as-is elements adhere to the specified surface flatness tolerances. An experiment was conducted to compare the results obtained using the proposed method with the ones obtained from Straightedge and F-number methods. The digital application of Straightedge and F-Number, as presented in that study, significantly reduces the time required for data collection and analysis, compared to traditional methods. However, flatness analysis remains conducted along sparsely surveyed 1D survey lines, which delivers results limited in spatial and wavelength resolution. Bosché and Biotteau [22] developed a method that applies 1D CWT to TLS data to characterize surface undulation periods. That approach addresses the limitation of previous works in wavelength resolution, i.e. the approach examines surface waviness at a wider range of wavelengths or characteristic periods. However, the study remains based on measurements along 1D lines that do not enable an analysis of flatness in all possible directions, and still provide results with limited spatial resolution.

2.3 Dimensional Quality Control: Point Cloud Data Quality Analysis for Surface Flatness Measurement

Lidar technology has a wide range of applications in the civil engineering industry, such as quantifying erosion rates and surface deformation [123], to landslide inventorying and mapping hazards [124], structural health monitoring [43], [125]–[127], road roughness quantification [128]–[132] and survey and maintenance of historic buildings [133]–[135].

In the construction industry, lidar is primarily used for as-built documentation that supports progress tracking [3]–[7], facility management [8]–[13], dimensional quality control [22], [48], [49], [136]–[138] in construction projects. In the area of dimensional quality control, lidar technology is commonly used for acquiring as-built data, owing to its ability to capture millions of points with mm-level accuracy. The acquired data is processed with the help of a multitude of algorithms, based on the desired applications. Few of the applications include assessing the flatness of the exterior facades using a color map derived from TLS point clouds [96], visualizing the elevation differences across a floor using elevation map generated from point cloud data [8] and assessing the dimensional compliance of concrete elements using BIM and TLS-based point cloud data [21]. Lidar-based point clouds, with the application of the Continuous Wavelet Transform (CWT), were also used in the assessment of floor waviness in [22], [137]. The study in [137] demonstrated the efficacy of applying the two-dimensional CWT (2D CWT) to lidar-based point cloud data for assessing the waviness of concrete surfaces. The comparative analysis between results obtained using the framework and those obtained using the Waviness Index (WI) method showed that the framework accurately identifies regions on the floor where surface waviness of different characteristics may exist. The framework utilized TLS-derived point cloud data to assess the surface waviness of concrete floors.

Unmanned Aircraft Vehicles (UAVs) are exponentially gaining popularity for collecting as-built data from construction sites. UAVs mounted with photographic cameras, thermal cameras and lidar sensors or “pucks” have been widely used for survey data collection. Compared to TLS, UAV-mounted lidar sensors are capable of collecting data from large survey areas in a non-intrusive manner with limited occlusions [38][39]. For instance, a person standing in front of the laser scanner can create a larger obstruction during data collection using TLS, compared to UAV-based scanning. Moreover, using TLS for collecting as-built data from working surfaces may hinder on-going operations and may interrupt workers on the surface. Thus, a comparison of the results of floor waviness obtained using point clouds derived from TLS and UAV. Additionally, a sensitivity

analysis of floor flatness measurement results must be performed to identify the appropriate scanning resolution of point clouds that are suited for surface waviness measurements.

3 Research Objective and Questions

The overarching goal of this research is to advance the body of knowledge in the area of utilizing remote sensing technologies, namely terrestrial and mobile lidar, and BIM to address the inefficiencies in existing construction practices in the field of dimensional quality assessment, quality inspection and progress tracking in the AEC industry.

A comprehensive literature review on construction progress tracking and dimensional quality control is included in Chapter 2 The main findings of the literature review are that the traditional data collection methods from construction sites pose several challenges for collecting as-built data that is accurate and comprehensive, and BIM and lidar technologies could potentially be leveraged to design better solutions to overcome the existing issues. Leveraging this knowledge, two main research questions were posed:

1. What are the existing inefficient practices for as-built data collection in the fields of dimensional quality assessment, quality inspection and progress tracking in the construction?
2. How can technology-supplemented as-built data collection improve dimensional quality assessment, quality inspection and progress tracking processes?

Further delving into the topic, specific objectives and research questions were identified and included in Chapters 4, 5 and 6 of the dissertation, and are listed below.

3.1 Objective 1

The state-of-the-art frameworks developed for progress monitoring of vertical construction are not directly applicable on horizontal construction projects. The adoption of such frameworks in horizontal construction projects may not necessarily provide accurate progress information. Most of the developed frameworks deliver object detection results for completed construction components in terms of Boolean variables. In other words, in a

given time frame, a component in a building structure is reported as either fully constructed or not constructed. In horizontal construction projects, work completed is often reported in terms of percentage of completion (POC) rather than checking the presence or counting the number of components. However, an accurate progress report would reflect the progress of bridge elements in terms of percentage of completion. In addition, a progress tracking framework for such projects should consider the formwork placed for partially completed elements. Therefore, the main objective of Chapter 4 is to develop a solution to address the inefficiencies associated with the existing methods for accurately reporting progress information for bridge construction projects.

The secondary objectives are listed below:

1. Explore the current progress tracking practices in horizontal and vertical construction projects, and identify existing gaps in knowledge in the field of progress tracking.
2. Develop a framework utilizing mobile laser scanning (MLS) data and four-dimensional (4D) BIM for bridge construction progress tracking.

Chapter 4 addresses the flowing research questions:

1. How can we report the progress of horizontal construction projects in terms of percentage of completion?
2. How can the synergy between MLS data and 4D BIM be defined to identify the built status of each element and road design layer in bridge construction projects?

3.2 Objective 2

The F-number and WI methods are the state-of-the-art practices in measuring the waviness of concrete slabs. To overcome the challenges associated with the implementation of these methods, newer technologies, such as terrestrial laser scanning (TLS), can be leveraged to measure surface waviness in a more efficient manner. The ability of a TLS device to accurately capture the geometric information from concrete surfaces provides an

opportunity to reconsider the assessment of surface waviness using traditional measurement instruments. Therefore, the objective of Chapter 5 is to develop a methodology that uses TLS to obtain accurate waviness information about newly constructed and existing concrete surfaces in an efficient manner. It aims to understand how traditional floor flatness measurement methods impact the accuracy of the data, and develops a framework to address these concerns.

Secondary objectives include:

1. Analyze how the inefficiencies associated with traditional surface waviness measurement methods could potentially be addressed using TLS data.
2. Develop a framework that utilizes TLS data to overcome the identified inefficiencies associated with the traditional floor flatness measurement methods.

Chapter 5 addresses the following research questions:

1. How can the traditional surface waviness measurement methods along 1D lines be extended to measure surface flatness along 2D surfaces to provide a more comprehensive assessment of surface geometry?
2. What tools and concepts can be applied to process data obtained using TLS to detect surface undulations in concrete slabs, and provide surface waviness results that strongly correlate with the results obtained using traditional methods?

3.3 Objective 3

The main objective of Chapter 6 is to compare the accuracy of floor waviness measurement results obtained using UAV-based (mounted with a 3D laser scanning sensor) and TLS-based technologies, and to determine whether UAS-based technology could produce comparable results that can be used in practice. The accuracy of the depth maps generated using as-built data obtained with an UAV and TLS are compared. Chapter 6 aims to

advance the application of TLS and UAV-based laser scanning in the field of dimensional quality assessment. The secondary objectives are listed below:

1. Perform a sensitivity analysis of floor flatness results obtained using TLS point clouds of various resolutions
2. Compare the results obtained using TLS and UAV-based point clouds.

Chapter 6 addresses the following research questions:

1. Can UAV and TLS-based 3D point cloud data produce comparable results for surface waviness detection of concrete slabs?
2. Do different resolution of point clouds affect the localization of surface defects?

4 Bridge Construction Progress Monitoring using Lidar and 4D Design Models

4.1 Summary

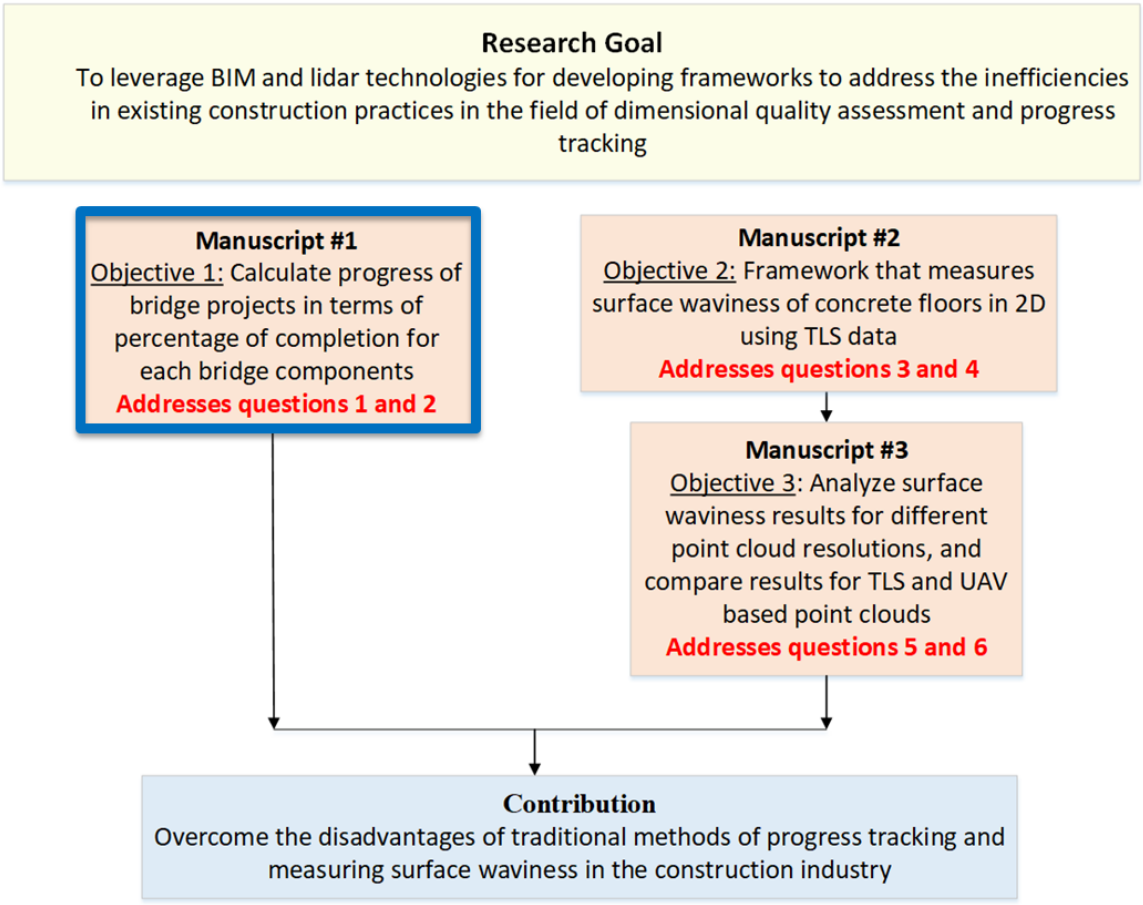

Figure 4.1 Overall research goal and contribution

The objective of this Chapter, as shown in Figure 4.1, is to overcome the shortcomings of the state-of-the-art techniques for monitoring bridge construction projects. The framework presented in this manuscript provides improvements over the existing semi-automated / automated progress techniques developed for measuring the progress of vertical construction projects in two main areas:

1. Incremental construction progress reporting as opposed to conventional binary classification of constructed elements.

2. Accurate classification of a road design layer (Asphalt Concrete Wearing Surface (ACWS))

The proposed framework is based on an algorithm that computes the percentage of completion for each bridge element in the laser scan data collected on a given date. In addition, the classification of a road design layer is performed accurately using the framework. The framework is expected to facilitate the wider adoption of new technologies for tracking horizontal construction projects' progress. State Department of Transportations (DOTs), which are in the midst of adopting BIM for infrastructure, can utilize 3D project design models together with lidar data for tracking the progress of bridge construction projects. This enables state DOTs to take full advantage of the lidar (terrestrial or mobile) data, which could be used for several other applications throughout the project lifecycle such as asset management [141].

4.2 Methodology

In this paper, a semi-automated methodology for monitoring bridge construction projects is proposed. The methodology is built upon the semi-automated comparison between project as-built data (3D point clouds) and 4D project design model (3D design model combined with project schedule) for determining the project status. To mimic the current progress monitoring process, as-built (lidar) data was collected from a bridge construction site on a weekly or biweekly basis depending on the type and duration of an activity scheduled for a given time frame. The raw data collected using mobile lidar system requires an initial pre-processing step. The pre-processed data is used together with the 4D project design model of the bridge to determine the status of a particular activity during construction.

The process involves identifying model elements in the 3D model that have been completed, are in the process of construction and remain to be completed. First, the point cloud data and 3D model are coarsely registered in the same coordinate system. To fine

tune the registration, an iterative process is implemented, where the distance between the 3D point cloud (registered scan) and 3D model is minimized at the end of each iteration. The object recognition process is implemented after the fine registration process to determine construction progress. Figure 4.2 demonstrates the semi-automated bridge progress monitoring methodology proposed in this study.

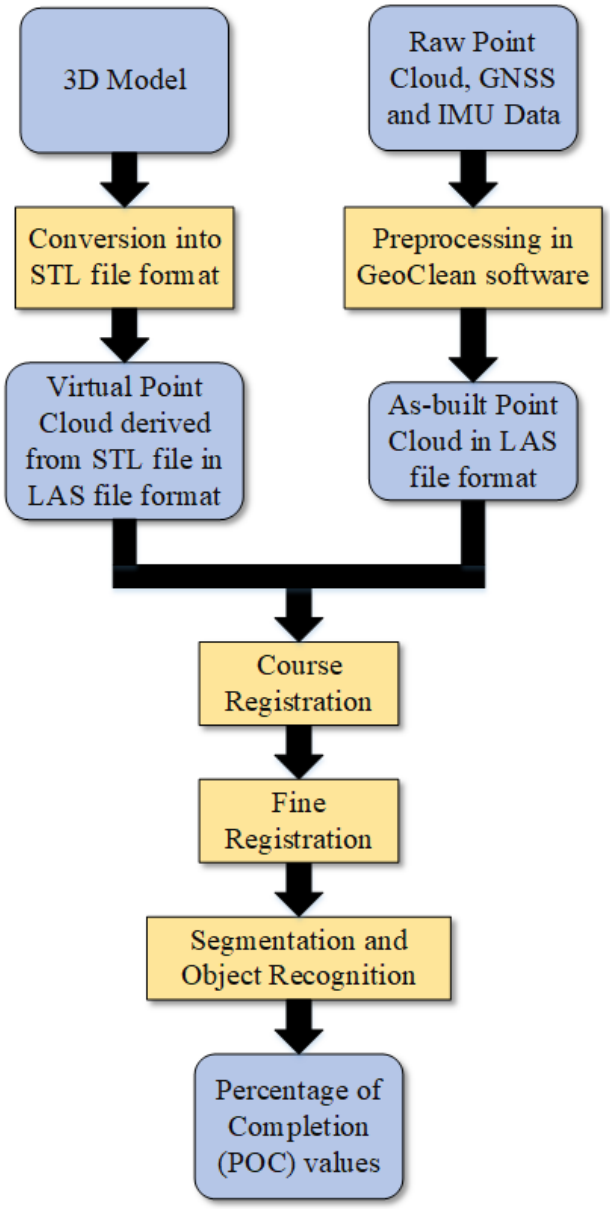

Figure 4.2 Proposed framework for project progress tracking

4.2.1 Data Preprocessing

The data extracted from the mobile lidar system is processed using Global Navigation and Satellite System (GNSS) and inertial measurement unit (IMU) data to generate the point cloud data representing the geometric as-built status of the bridge project. The GNSS data is obtained from the closest permanent GNSS station to the project site. This data helps account for the errors occurring due to ionospheric disturbance and various systematic errors. Typically, this data is available in the form of Receiver Independent Exchange (RINEX) files from the Oregon Real Time Network maintained by the Oregon Department of Transportation (ODOT), the National Geodetic Survey Continually Operating Reference Stations (CORs), or the Plate Boundary Observation (PBO) network maintained by UNAVCO. Point cloud data is generated processing the raw mobile lidar data consisting of ranges, angles and timestamps referenced to the origin of the scanner, GNSS and IMU data. The data collected using the mobile lidar system may be combined with terrestrial lidar data depending on the project requirements. The point cloud dataset, which can be stored in several formats such as LAS and E57, can then be used for further processing.

4.2.2 Data Processing

Data processing comprises of coarse registration, fine registration, segmentation, object recognition and percentage of completion (POC) calculation steps. The as-built data that was saved in LAS file format is coarsely registered with the virtual point cloud of the design model, which is derived from the STL file format of the as-planned 4D model (3D design model (Figure 4.3) + project schedule). The coarse registration process is facilitated by the selection of corresponding pair of points in the virtual point cloud and as-built point cloud. The efficiency of the coarse registration process can be improved by developing the 3D model in the same coordinate system as the as-built point cloud. The fine registration step, based on the ICP algorithm developed in [142] is applied to fine-tune the registration. The segmentation, object recognition and POC calculation steps are then applied to the finely registered as-built and virtual point clouds.

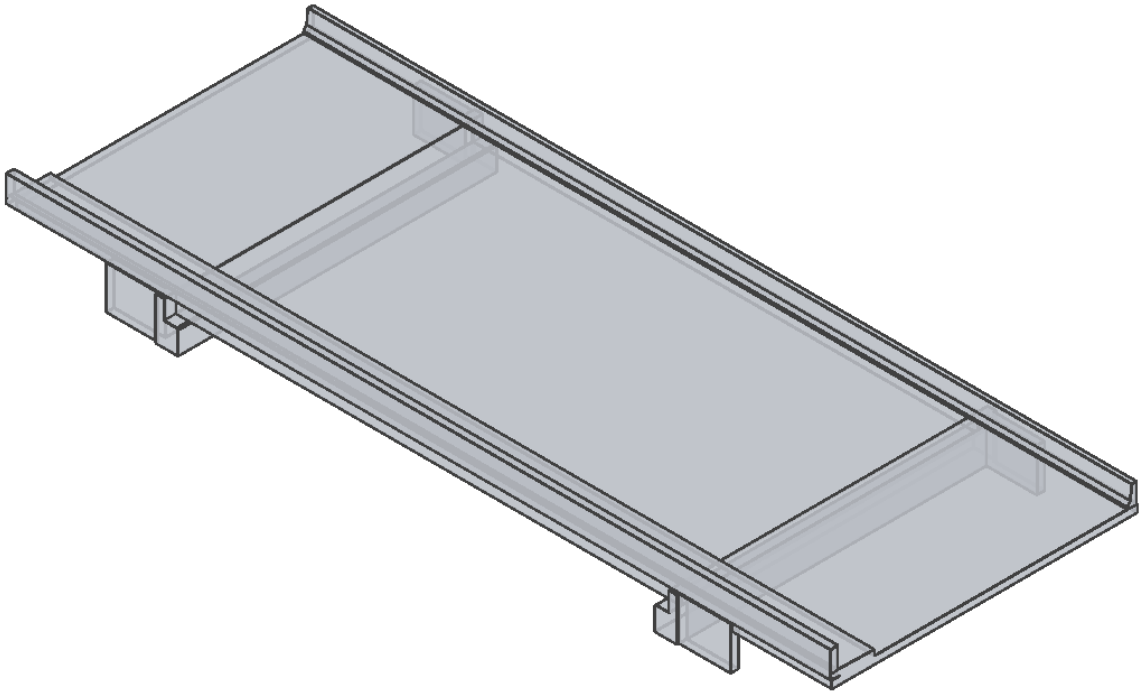

Figure 4.3 3D model of Truax Creek Bridge, developed from its 2D design drawings

4.2.3 Registration of as-built data with the 3D design model

4.2.3.1 Coarse Registration

The preprocessed point cloud data is aligned with the 3D as-planned (design) model to facilitate the identification and comparison of bridge components in the point cloud dataset and the as-planned model. The initial step requires converting the 3D bridge model developed by the researchers using Revit Software into STereoLithography (STL) file format. The next step is to manually identify and select corresponding points in the 3D design model (virtual point cloud) and the 3D as-built point cloud for the coarse registration step, i.e. aligning the two datasets in the same coordinate system. Note that the as-built point cloud is fixed and the virtual point cloud is moving during the entire registration process.

4.2.3.2 Fine Registration

After the coarse registration process, a nearest neighbor algorithm is implemented to find points in the as-built point cloud, that are nearest to the query points in the virtual point cloud. The nearest neighbor algorithm finds one point in the as-built point cloud for every query point of the virtual point cloud, and is equivalent to a one-to-one matching process. In the following step, the points in the as-built point cloud that exceed a predefined threshold (7 cm) are discarded. A threshold that corresponds to the noise present in the as-built data is selected. The resulting point cloud has fewer number of points as only the points that correspond to the elements in the 3D model are retained. Next, an iterative closest point (ICP) algorithm is implemented to better align the point cloud and the 3D design model, which is necessary for accurate object recognition. The process involves minimizing the Euclidean distance between the selected pair of points between the as-built point cloud and the 3D design model (virtual point cloud) in a series of iterative processes, governed by either a maximum threshold distance or the maximum number of iterations. The output of the coarse and fine registration steps are subsampled versions of the as-built and virtual point clouds, which contain points corresponding to the actual work performed on site. The virtual point cloud obtained in this step has equal or smaller number of points than the original virtual cloud. This is because process of obtaining the nearest neighbor points eliminates points that do not correspond to the as-built point cloud obtained for a certain date.

A composite transformation matrix, combining both transformation matrices obtained from the coarse and fine registration steps, was obtained and used in segmentation and object recognition steps. A summary of the coarse and fine registration steps are shown in Figure 4.4.

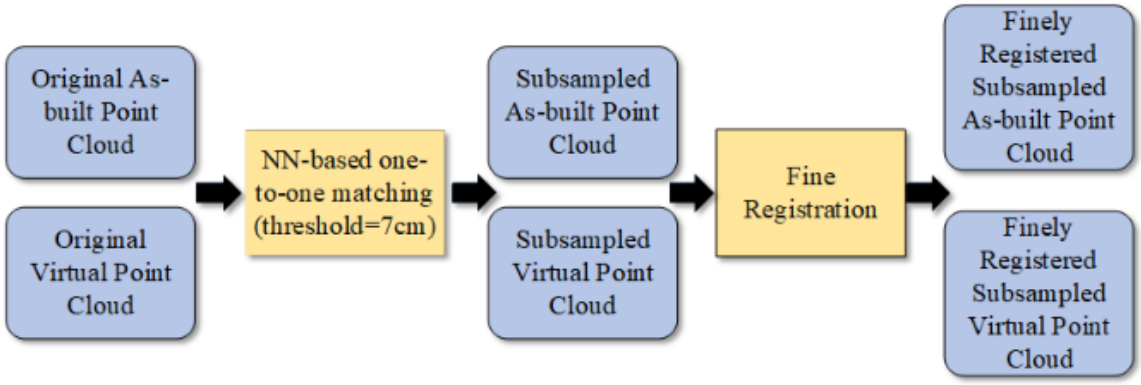

Figure 4.4 Overview of the fine registration step

4.2.4 Registration of as-built data with each element in the 3D design model

Correspondence between each bridge element in the 3D model and the subsampled as-built point cloud is established in this step. This is achieved by repeating the coarse and fine registration process for each virtual point cloud corresponding to each bridge element in the 3D model. The process is simpler compared to the registration process discussed in the previous step because it involves directly applying a composite transformation matrix to the virtual point clouds of each bridge element. The composite transformation matrix, comprised of the transformations for the coarse and fine registrations, is obtained from the registration process between the virtual point cloud (derived from the STL file) and the as-built point cloud collected for a particular date, in the previous step.

To register as-built data with each single element in the 3D design model, each bridge element needs to be exported as a separate STL file, and virtual point clouds for each of those elements should be generated. The next step requires to apply the composite transformation matrix to each of these elements separately. During this process, the elements undergo processes of coarse and fine registrations, similar to the previous registration step between the entire STL model and the as-built point cloud. This step enables keeping a track of the element that is registered, and assigning a percentage of completion to that element.

4.2.5 Segmentation and Object Recognition

The subsampled virtual point cloud and finely registered virtual point cloud of each of the individual bridge elements obtained in the previous step are used for segmentation. The STL file of each bridge element carries the label of each bridge element, which is passed onto the corresponding virtual point cloud of each bridge element. Generating STL files, and thus, virtual point clouds for each bridge element, helps keep track of the POC values of each bridge element on a given scan date.

The segmentation process involves finding the nearest neighbor of each query point in the finely registered virtual point cloud of an individual bridge element within the segmented subsampled virtual point cloud for a given scan date. The process is carried out using the same threshold (7 cm) used in the registration step. A virtual point cloud of an individual element that accurately represents the as-built status of that element on a given scan date is obtained from the one-to-one matching process. For a given bridge element, the one-to-one matching process between the segmented subsampled virtual point cloud and the finely registered virtual point cloud of the element yields a fragment of the segmented subsampled virtual point cloud that accurately represents the as-built status of that element for a given date. This fragment of the segmented subsampled virtual point cloud for a bridge element is an indicator that the bridge element is detected as constructed or under construction. The percentage of completion is calculated in the next step.

It is important to note that at any given scan date, if a bridge element has not been constructed, or if a constructed bridge element is occluded from the scanner's view, no overlapping region exists between subsampled virtual point cloud and finely registered virtual point cloud of an individual bridge element, therefore it is not detected.

4.2.6 Asphalt Concrete Wearing Surface (ACWS) Detection

The detection and POC calculation of bridge elements relies upon the accuracy of the registration between the as-built point cloud and the virtual as-planned point cloud. However, adopting this approach for the detection of road design layers in the as-built point clouds may not yield accurate results. The inaccuracies in detection may result from registration error, construction errors, or due to noise inherent in the instrument. The output of coarse registration and fine registration steps described in Sections 4.2.3 may not be accurate if the sum of these errors exceed the thickness of the ACWS layer. Consequently, the object recognition step in 4.2.5 might misclassify a road design layer in the presence of multiple road design layers. Hence, a new approach is required for identifying road design layers, specifically the upper layer which is typically 2.5 – 5 cm in thickness.

Power Spectral Density (PSD) is used for distinguishing between the road design layers. PSD has been widely used in the area of texture and material classification, determining roughness and pavement friction evaluation [143]–[147]. PSD quantifies the power of each frequency content of a signal, and it is calculated using the square of the magnitude of the Fourier Transform. Initially, depth maps of the surfaces are created. The depth maps are converted from the spatial domain to the frequency domain using Fourier Transform. The wavelengths that are present in the 2D spatial "signal" are then identified.

The Fourier Transform of a 2D signal, f(x,y) can be represented as [148]:

$$F(u,v)=\int_{-\infty}^{+\infty} f(x,y)e^{-I\,2\pi(ux+uy)}\,dx\,dy \qquad (4.1)$$

where, f is the frequency in Hertz.

The spectral density, C(q) is given by [149]:

$$C(q)=\frac{1}{U}*\frac{a^2}{M*N*(2\pi)^2}|F(u,v)|^2 \qquad (4.2)$$

where U is the normalization constant, a is the interval size of the depth map, M and N represent the size of the depth map and X(f) is the Fourier Transform.

The area under the power spectral density curve calculated over all wavelengths is given by [143]:

$$RMS^2 = \frac{(2\pi)^2}{M*N*a^2} \sum_M \sum_N |C(q)|^2 \quad (4.3)$$

where RMS (Root Mean Square) represents the total energy level across a frequency range in the form of a single value.

Typically, the RMS parameter characterizes surface roughness. The scope of this study is limited to detecting only the ACWS layer, and the RMS values for the road surface before and after placing the ACWS layers will have different values. Thus, in our case, the RMS is simply considered as a parameter whose value is used to distinguish one surface from another. Point cloud data obtained using a TLS can be used for roughness analysis purposes because it is more accurate compared to mobile laser scanning (MLS) data, and the use of the RMS roughness parameter for identifying multiple road design layers will be discussed in future work.

After the detection of a road design layer, the POC calculation step in Section Percentage of Completion can be used for determining the progress status of the ACWS layer, similar to other bridge elements.

4.2.7 Percentage of Completion

The detection of a particular bridge in the object recognition step enables assigning a percentage of completion (POC) to that element. The status of completion of an element can be determined using the POC values. The process of segmentation described in the previous step generates a point cloud that accurately represents the geometric as-built status on a given date for each virtual point cloud of an individual bridge element. The alignment between the overall virtual point cloud of the bridge and the virtual point cloud of the individual element reveals the geometric faces of a bridge element that overlap in the two scans. The face containing the maximum number of overlapping points are chosen and a

convex hull of the face is constructed in both point clouds. The percentage of completion (POC) for an element e at a given date d is computed using the following formula:

$$POC_{e,d} = \frac{A}{A'} * 100\ \% \quad (4.4)$$

where, A is the area of the convex hull of one of the common faces in the segmented virtual point cloud of one as-built element. A' is the area of the convex hull of the same face as in A.

The output of the one-to-one matching process between the segmented subsampled virtual point cloud and the finely registered virtual point cloud of the element for a given scan date shows whether the construction of an element has started on that day. If the element was not detected in the segmented subsampled virtual point cloud, an empty output is obtained. A non-empty output signifies that an element was detected. Precedence relationships representing the dependencies of construction of one element on the other is developed to verify the POC calculated for all elements at a given scan date. The calculation of POC for all possible cases are summarized below:

1. If an element is recognized, $POC_{e,d}$ is the maximum value between the existing POC (if it exists) and the POC calculated using Equation 4.4 for that day. Note that the element may have an existing POC if one of its successors is more than 80% complete (using the information from the precedence relations). Majority of the bridge elements in this project were either 30%, 50% or 100% complete on different scan dates. In some cases, the elements that are fully constructed (100% complete) may be inaccurately reported to be 85% or 90% complete. In such cases, it would still be safe to assume that the predecessor of the bridge element is 100% complete if its successor is anywhere above 50% complete. As a conservative estimate, 80% was chosen. If the $POC_{e,2}$ is lower than the $POC_{e,1}$ for an element, $POC_{e,2}$ is set to the value of $POC_{e,1}$, and so on. This can be observed when the fully completed element is occluded from the scanner's view.

2. If an element is not recognized for reasons discussed above, $POC_{e,d}$ is set to the maximum value between zero and the existing POC (if it exists). Again, note that

the element may have an existing POC if one of its successors is more than 80% complete.

3. $Date_i$ represents the date the scans were collected, where $Date_1$ represents the first day of scanning. Once the POCs for all elements for a particular scan date $Date_i$ are computed, the results are verified using the precedence relations. If the $POC_{e,d}$ reaches over 80% at a given date, the POCs for all other elements that are its predecessors during construction are set to 100%. This may also occur when a fully completed element is not visible to the scanner (occluded elements).

The segmentation, object recognition and POC calculation steps are summarized in Figure 4.5.

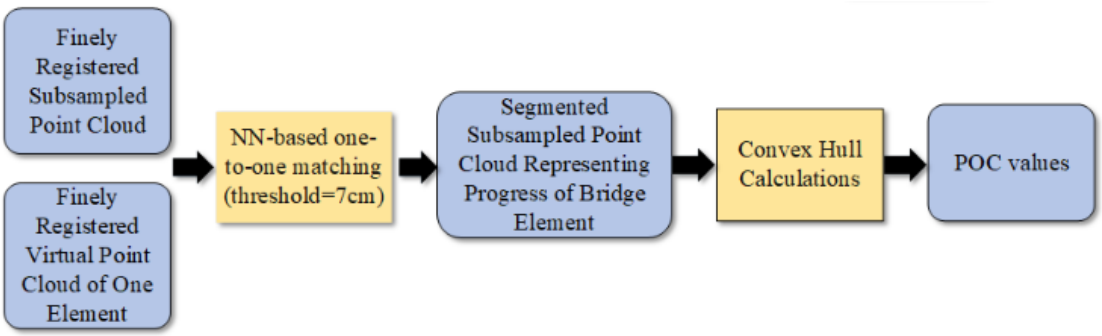

Figure 4.5 Overview of segmentation, object recognition and POC calculation steps

4.3 Experimental Results

The selection of a suitable bridge construction project was important for this study. To be suitable for data collection, the project had to meet the following requirements. 1) The project must be preferably in the initial stages of construction, so that the construction of each bridge element can be captured. 2) The data collection cycles should be tentatively based on the provided construction schedule. This is important to make sure that the as-built data for each bridge element is captured. If a particular data collection cycle is too long, the construction of some bridge elements may not be captured. In this study, the

Truax Creek Bridge Replacement project located in Albany, OR was selected for the case study. The bridge replacement project involved demolishing the existing bridge structure and building a new one. When the data collection commenced, the northbound lane had been completed, but was not yet open to traffic. The traffic was operating on the southbound lane. The new bridge structure is approximately 108 feet in length and 42 feet in width. The construction site is shown in Figure 4.6. Depending on the work scheduled for a particular week, the scans were collected from the construction site on a weekly or bi-weekly basis.

Figure 4.6 Study site, Truax Creek Bridge in Albany, OR. Left: Google Maps showing the location of the bridge. Right: Photo showing the southbound lane near its completion date.

A TOPCON IP-S2 mobile mapping system was used to collect as-built data from the site. The mapping system consists of an IMU, GNSS sensor and a HDL-64E S2.2 lidar scanner developed by Velodyne. The lidar scanner generates 1.3 million points per second, capturing data from targets up to 100 m away, across a 360° horizontal field of view and a 30° vertical field of view. On average, three passes were made along the length of the bridge construction site to capture as much detail as possible. At the end of each data collection cycle, the progress made on the project from the start of construction until the scan date is captured.

4.3.1 Data Preprocessing

The GNSS data was obtained from the National Geodetic Survey (NGS) Continuously Operating Reference Station (CORS) website in the form of RINEX files. The files were downloaded in .gz format, which were imported into GeoClean software. The configuration of the base profile used in processing the GNSS data is presented in Table 4.1. The output file was generated in *.las file format in grid coordinate system (XYZ coordinates).

Table 4.1 Base profile entry configuration in GeoClean

Antenna Type	Dorne Margolin with chokerings, Model 70
Coordinate Type (IGS08 Epoch 2005)	ECEF
X [m]	-2498423.869
Y [m]	-38028020.840
Z [m]	4454737.819

4.3.2 Registration

The 3D model of the Truax Creek Bridge structure was developed using the 2D design drawings obtained from the Oregon Department of Transportation (ODOT). The model was developed in Autodesk Revit software in Revit (.rvt) file format and exported into stereolithography (STL) format. However, the properties of the output STL file, including triangle count, could not be modified during the export. Thus, the exported STL file was imported into Gmsh, an open source software that allows further tessellation of the model, i.e. increase the triangle count. At the end of this process, another STL file of the model including 2,949,120 triangles was obtained. It is important to note that higher triangle count enables better one-to-one point matching process. The STL model is comprised of a tessellation of triangles that represent the geometric faces of the bridge elements in the 3D model. The .las files exported from the Geoclean software (original as-built point cloud), and the STL file of the bridge model (original virtual point cloud derived from it), are both

imported into CloudCompare software for coarse registration. The original virtual point cloud derived from the STL file of the model, and the original as-built point cloud collected on 06/22/2017 are shown in Figure 4.7 and Figure 4.9 respectively. Five points in the original as-built point cloud and the original virtual point cloud were selected for the coarse registration step. Figure 4.8 and Figure 4.10 show the output subsampled virtual point cloud and the subsampled as-built built cloud, obtained at the end of the one-to-one matching process, respectively.

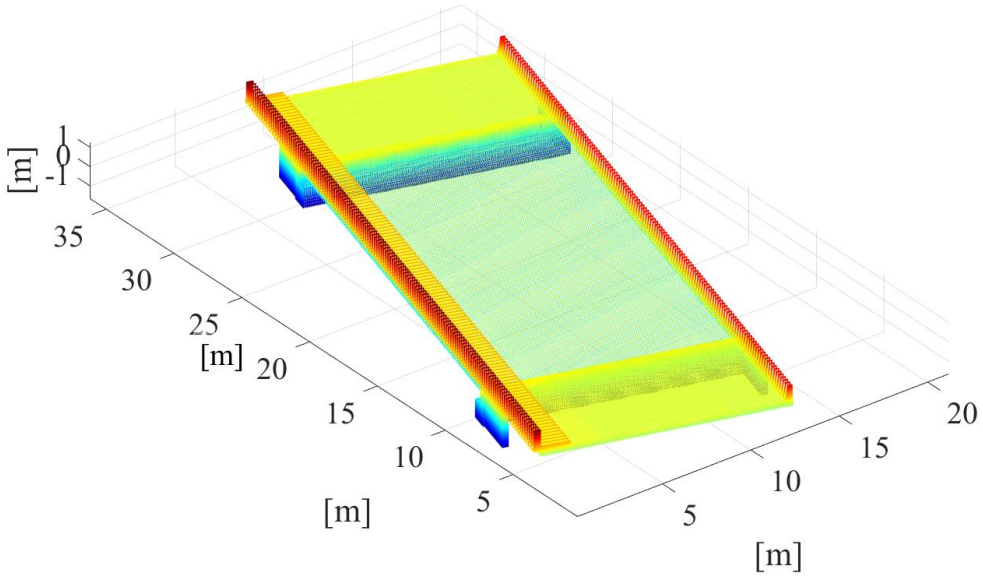

Figure 4.7 Original virtual point cloud derived from the STL model.

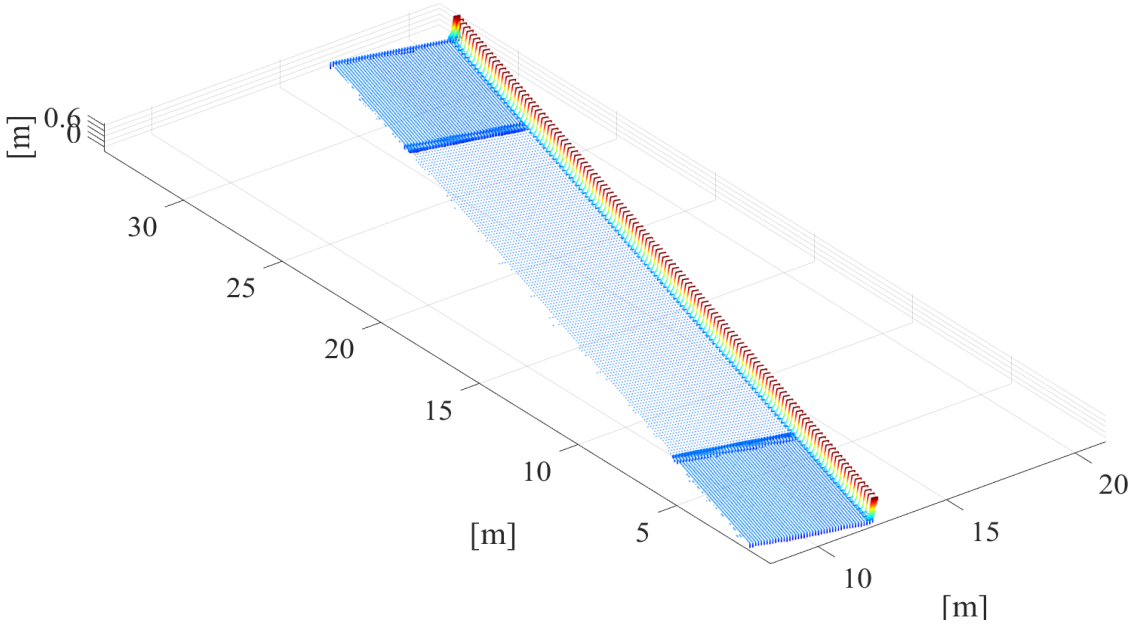

Figure 4.8 Subsampled version of the original virtual point cloud obtained from the STL model.

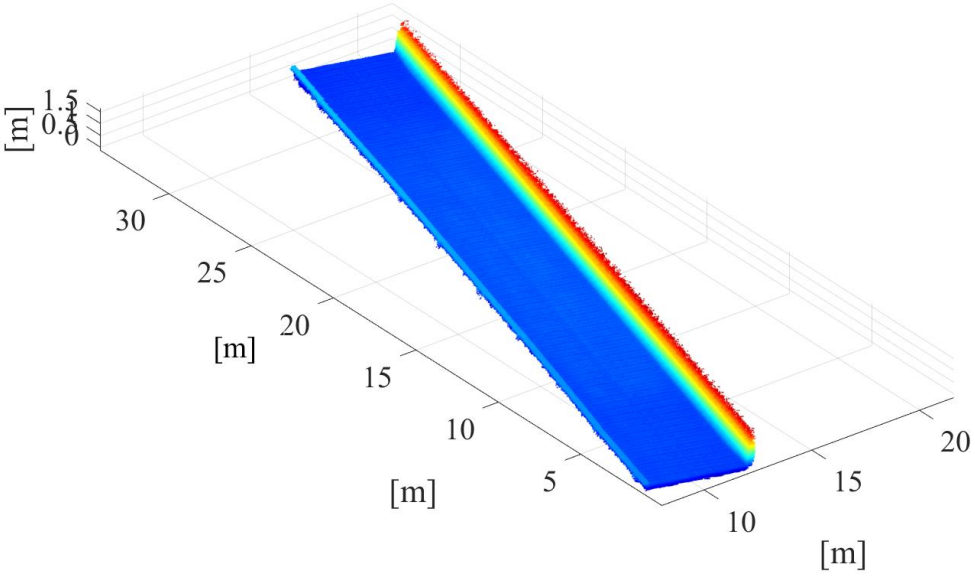

Figure 4.9 Original as-built point cloud scan collected on June 22, 2018.

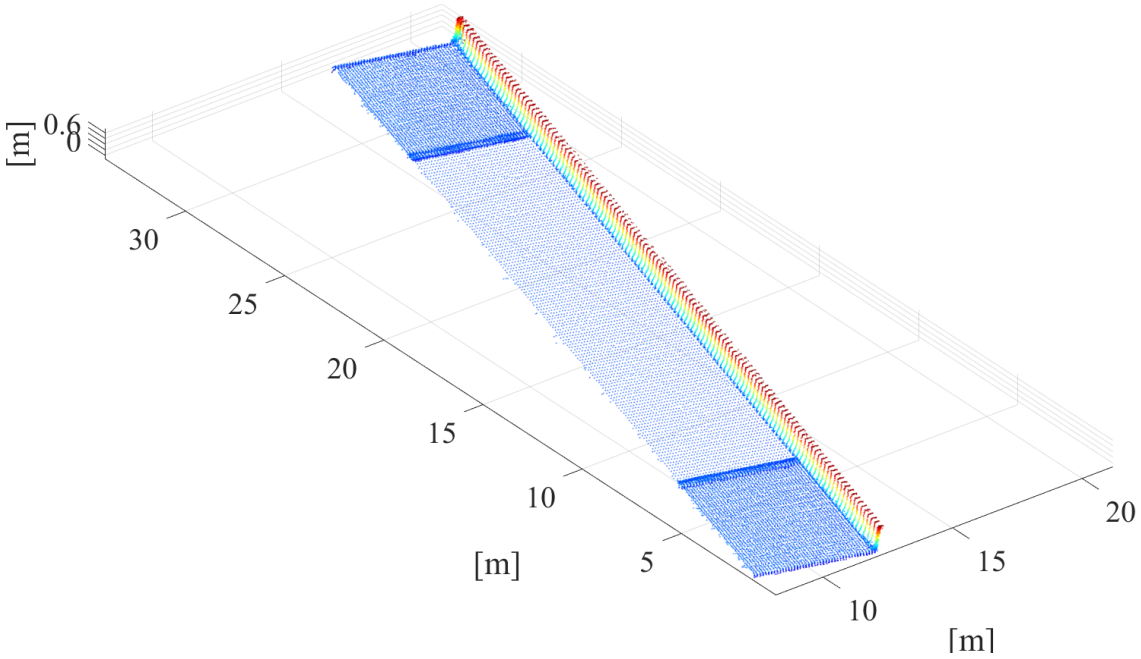

Figure 4.10 Subsampled version of the as-built point cloud collected on June 22, 2018.

To further improve the registration results, upon the completion of the coarse registration process, the original as-built point cloud and the original virtual point cloud are finely registered using pairs of points in both point clouds. For a pair of points, one point belongs to the original virtual point cloud (query point), and the other point belongs to the original point cloud that is nearest to the query point. After this step, each of the points in the original virtual point cloud is matched with a corresponding point in the original as-built point cloud. When implementing this process, 7 cm was chosen as the threshold distance to account for the noise levels of the velodyne lidar system and construction errors. A slice of the alignment between the as-built (red, green and yellow colored points) and virtual point cloud (white colored points) is shown in Figure 4.11. From the distance between a pair of points in the as-built and virtual point clouds, it is evident that the scan data contains noise that is approximately 3-4 cm (1 sigma (σ)). Thus, 7 cm was chosen as the threshold to account both for noise in the as-built data and construction errors.

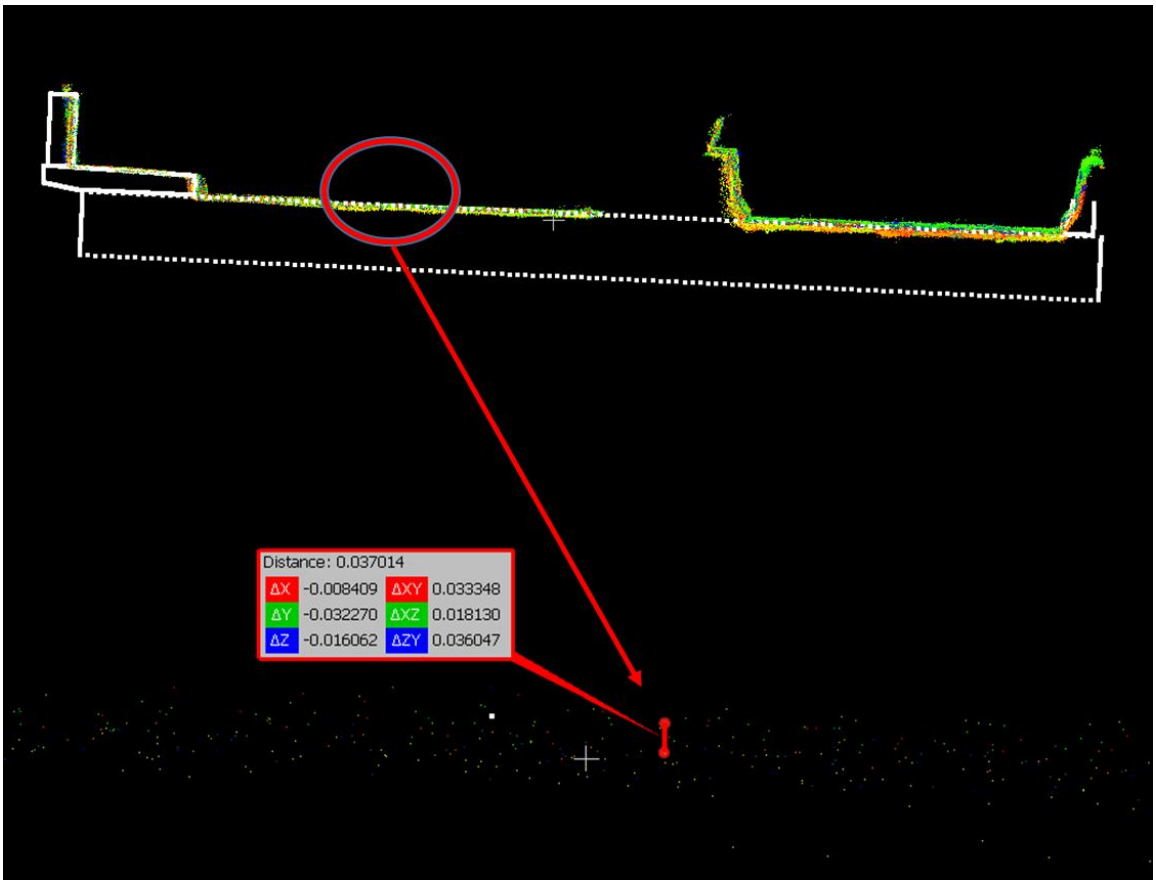

Figure 4.11 A section of the aligned as-built (red, green and yellow colored points) and virtual point clouds (white colored points) (scan date: October 22, 2018)

Upon identifying the nearest neighbors, a filtered as-built point cloud was generated, which is a subsampled version of the original as-built point cloud that is free from noise. This one-to-one matching process simultaneously generates a subsampled version of the original virtual point cloud, which contains the same number of points as the subsampled version of the original as-built point cloud. Following this step, the subsampled as-built point cloud was registered (fixed) with the subsampled virtual point cloud (moving) using an ICP algorithm. A point-to-point based distance minimization metric was defined to facilitate the fine registration process. The algorithm was designed to terminate when the error between three consecutive iterations is less than 1*10^-6. Table 4.2 presents the registration results for the scans collected from the bridge construction site over a period of three months. Following this step, a composite transformation matrix, comprised of

coarse and fine registration transformation matrices, was applied to the virtual point clouds of the 14 individual elements of the 3D model.

Table 4.2 RMS errors for the coarse and fine registrations

Scan Date	Number of Points in Original As-built Point Cloud	Number of Points after NN matching (before fine registration)	Fine registration RMSE [m]
6/22/2018	3,669,647	179,247	0.021
7/6/2018	3,983,640	257,160	0.028
7/13/2018	2,275,266	280,656	0.031
7/24/2018	5,151,269	350,009	0.030
8/1/2018	4,257,637	386,029	0.029
8/14/2018	6,082,413	351,194	0.030
8/22/2018	2,775,230	308,500	0.031
9/4/2018	6,327,087	375,488	0.024
10/22/2018	3,522,971	273,200	0.031

4.3.3 Segmentation and Object Recognition

The segmentation process is facilitated by finding the nearest neighbor of each query point in the finely registered virtual point cloud of an individual bridge element, within the segmented subsampled virtual point cloud for a given scan date. The nearest neighbor search, similar to the previous step, is also carried out using the same predefined threshold, 7 cm. Figure 4.12 shows the result of the segmentation process applied to the bridge deck using the scan collected on June 22, 2018. The virtual point cloud of an individual bridge element and the fragment of the segmented subsampled virtual point cloud are used to determine common pairs of geometric faces corresponding to the bridge elements. For this project, using a mobile lidar for data collection ensured that the upper face of the as-built bridge elements were scanned. For this reason, the upper face, containing maximum number of points that overlapped in the virtual point cloud of an individual bridge element

and the fragment of the segmented subsampled virtual point cloud, was chosen for POC calculations in the next step. The convex hull for the two sets of point clouds was then calculated. The resulting convex hull for these point clouds are shown in Figure 4.13.

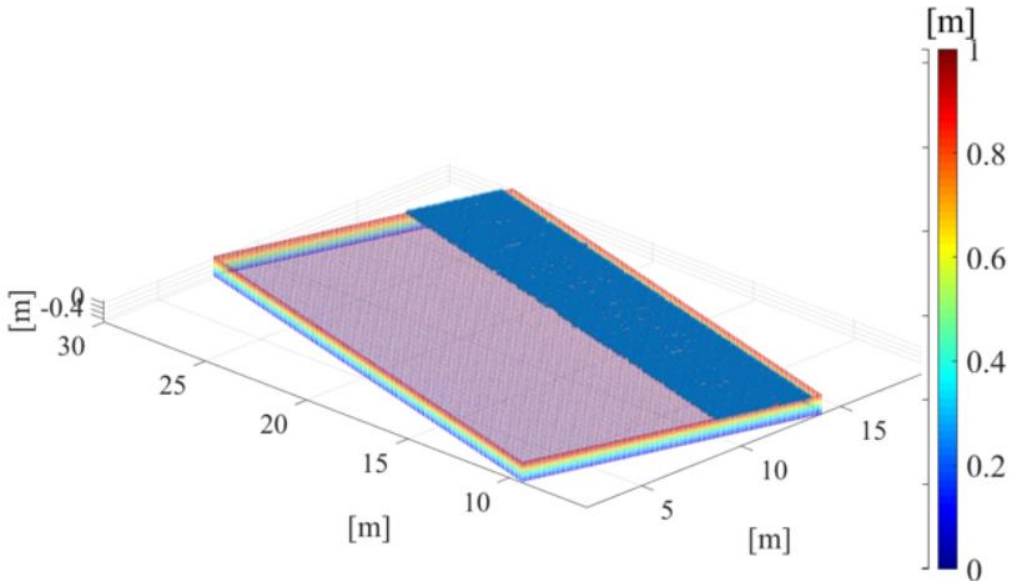

Figure 4.12 Fraction of the segmented subsampled virtual point cloud (shown in blue dots) obtained at the end of segmentation process between the subsampled virtual point cloud and the virtual point cloud of the bridge deck (scan date: June 22, 2018)

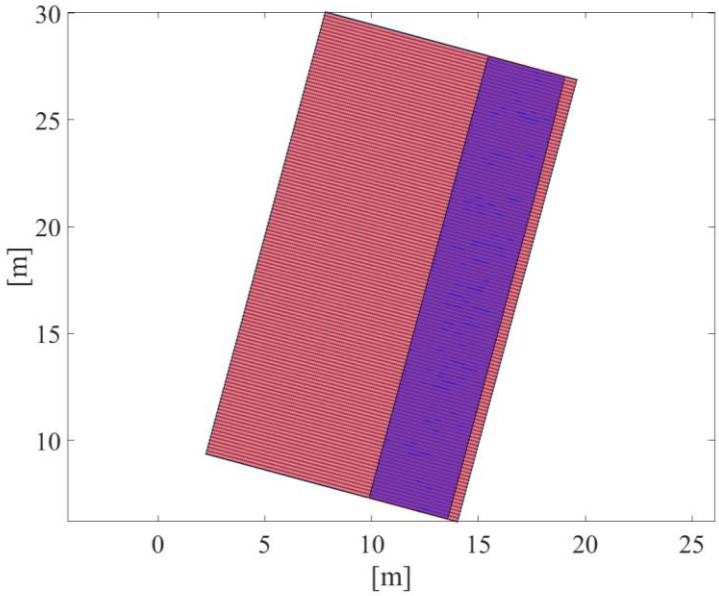

Figure 4.13 Convex hull for both point cloud datasets for the bridge deck (scan date: June 22, 2018)

4.3.4 ACWS Detection

The road surface on the southbound lane was manually extracted for the unpaved and paved surfaces using the as-built point clouds collected on August 22, 2018 and October 22, 2018 respectively. Each of the as-built point clouds were divided into six sections, generating a total of six point clouds for the unpaved road and another six point clouds for the paved road. The reason for creating sections is to evaluate the PSD for all of these sections individually, and to validate that the RMS values for the paved road sections are significantly different from the RMS values for the unpaved road sections. Next, a depth map was generated from each of the as-built point clouds of the two road surfaces, a total of 12 depth maps, using a sampling interval of 4 cm. The sampling interval value was determined based on a manual inspection of the point cloud data, which revealed that the point spacing in the as-built point clouds along the x-y plane is approximately 2-3 cm. Note that the point spacing can be improved significantly to mm-level by using a terrestrial laser scanner for data collection. Figure 4.14 and Figure 4.15 represent the PSD data obtained after analyzing the twelve profiles.

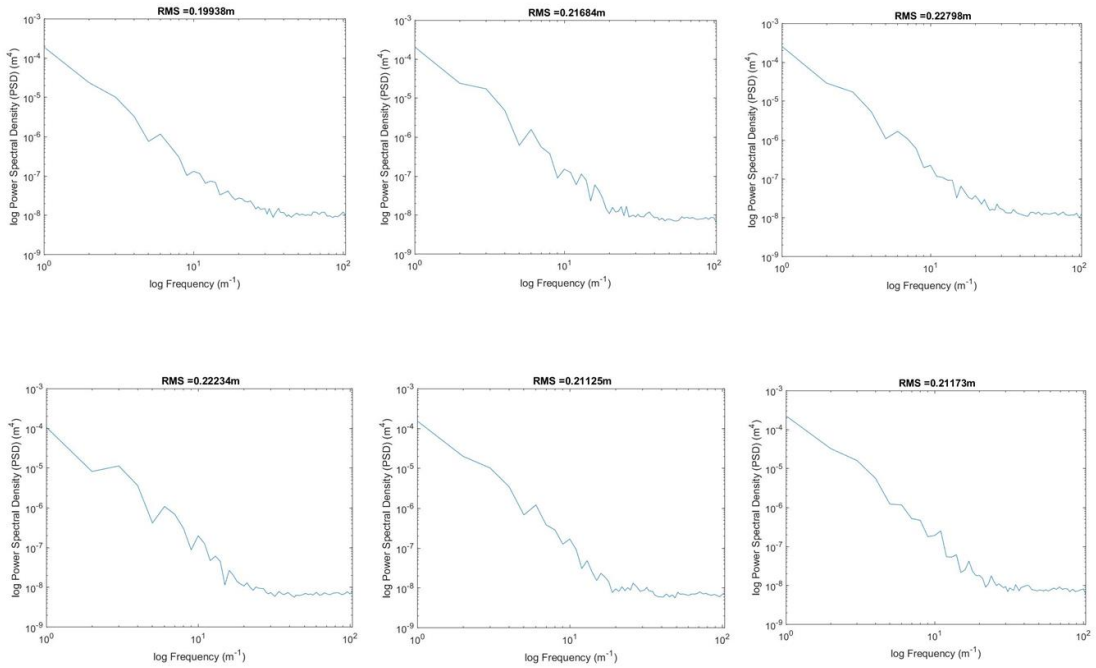

Figure 4.14 PSD data for the six sections of the unpaved road (scan date: 22nd October, 2018)

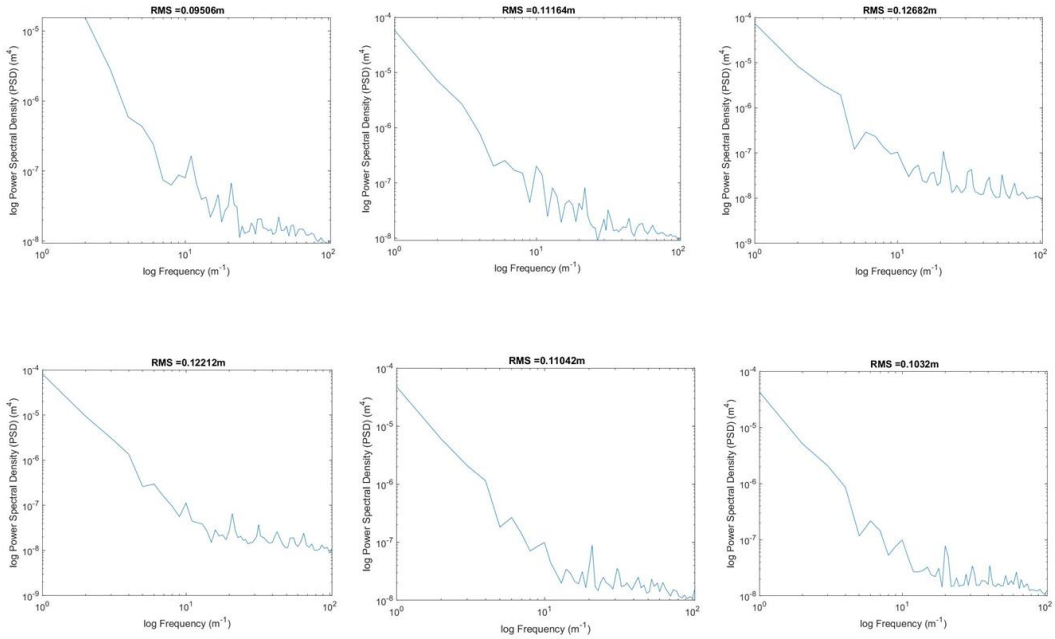

Figure 4.15 PSD data for the six sections of the paved road (scan date: 22nd August, 2018)

The RMS values obtained for the unpaved road surfaces are higher than those obtained for the paved road surfaces. A lower RMS value indicates a smoother surface, which is similar to our case since paved surfaces are smoother than the unpaved surfaces. An independent samples t-test was conducted to compare RMS values of paved and unpaved road surfaces. There was a significant difference in scores for paved (M=0.11, SD=0.01) and unpaved road (M=0.22, SD=0.01) conditions; t (10) = 16.47. From these results, it can be concluded that the two road surfaces have been distinguished from one another. Specifically, the results suggest that PSD can be used to analyze road design layers and distinguish layers based on the characterization of surface properties.

4.3.5 POC calculation

The as-planned and as-built POC for the bridge project are shown in Table 4.3 and Table 4.4 respectively. The as-planned POC values in Table 4.3 were calculated manually by referring to the obtained schedule. The purpose of preparing the as-planned POC is to help in validating the accuracy of the POC calculations.

Table 4.3 As-planned POC (%)

Scheduled progress (%)	**6/22**	**7/6**	**7/13**	**7/24**	**8/1**	**8/14**	**8/22**	**9/4**	**10/22**
'Abutment_N'	30	30	50	100	100	100	100	100	100
'Abutment_S'	30	30	50	100	100	100	100	100	100
'BridgeEndPanel_N'	30	30	30	30	100	100	100	100	100
'BridgeEndPanel_S'	30	30	30	30	100	100	100	100	100
'Deck'	30	30	30	100	100	100	100	100	100
'Parapet_E'	100	10	100	100	100	100	100	100	100
'Parapet_W'	0	0	0	0	0	50	50	100	100
'Sidewalk'	0	0	0	0	0	100	100	100	100
'Wingwall_NL'	0	0	0	100	100	100	100	100	100
'Wingwall_NR'	100	10	100	100	100	100	100	100	100
'Wingwall_SL'	0	0	0	100	100	100	100	100	100
'Wingwall_SR'	100	10	100	100	100	100	100	100	100
'ACWS'	0	0	0	0	0	0	0	0	100

Table 4.4 As-built POC

Actual progress (%)	**6/22**	**7/6**	**7/13**	**7/24**	**8/1**	**8/14**	**8/22**	**9/4**	**10/22**
'Abutment_N'	31	35	35	100	100	100	100	100	100
'Abutment_S'	35	35	35	100	100	100	100	100	100
'BridgeEndPanel_N'	36	36	36	36	93	100	100	100	100
'BridgeEndPanel_S'	35	35	35	35	98	100	100	100	100
'Deck'	34	34	34	97	100	100	100	100	100
'Parapet_E'	99	100	100	100	100	100	100	100	100
'Parapet_W'	0	0	0	0	0	3	70	70	94
'Sidewalk'	0	0	0	1	5	100	100	100	100
'Wingwall_NL'	0	0	100	100	100	100	100	100	100
'Wingwall_NR'	100	100	100	100	100	100	100	100	100
'Wingwall_SL'	0	0	84	100	100	100	100	100	100
'Wingwall_SR'	100	100	100	100	100	100	100	100	100
'ACWS'	0	0	0	0	0	0	0	0	97

The differences between corresponding as-planned POC values in Table 4.3 and as-built POC values in Table 4.4, are shown in Table 4.5. The error values marked in yellow represent errors due to the limitations inherent in the convex hull algorithm that calculates overlapping area between the faces of the virtual and as-built point clouds, and the POC is defined as the ratio of these two. The planned POC may reflect an element to be 100% complete but the as-built POC may reflect it to be 96% complete. Practically, if such values are obtained, it can be interpreted as the slab being complete. The errors ranging from -6% to 7% in the yellow cells are the result of including or excluding a few as-built points belonging to these elements. This is likely to occur during the segmentation step since not all points (especially the ones on boundaries) are classified as belonging or not belonging to a particular element. Addition of a few points, depending on their location, can significantly impact the convex hull results, and consequently, the POC values. Note that for ACWS, the POC values are zero from scan dates June 22, 2018 through September 4, 2018, as shown Table 4.4. This is because the framework detects the ACWS layer only after the deck is 100% complete. A visual inspection of the as-built scans belonging to these dates reveal that the corresponding values in Table 4.5 are reasonable. In addition, Table 4.6 shows the differences in as-built POC (manual-based) and as-built POC (framework-based) for all the bridge elements for different scan dates (in terms of percentage), and the values help validate the performance of the framework. The as-built POC (manual-based) values are calculated by manually measuring the dimensions of the as-built point in CloudCompare software. The definitions are provided below:

- As-built POC (manual-based)
  - POC based on Actual Progress
  - Calculated based on the manual measurements performed on the as-built point cloud
- As-built POC (framework-based)
  - POC based on Recognized progress
  - Calculated using the POC calculation formula
- As-planned POC (schedule-based)
  - POC based on Scheduled progress

– Calculated based on project schedule

Table 4.5 Differences in POC for all the bridge elements on different scan dates (%)

Differences in POC (%)	**6/22**	**7/6**	**7/13**	**7/24**	**8/1**	**8/14**	**8/22**	**9/4**	**10/22**
'Abutment_N'	-1	-5	15	0	0	0	0	0	0
'Abutment_S'	-5	-5	15	0	0	0	0	0	0
'BridgeEndPanel_N'	-6	-6	-6	-6	7	0	0	0	0
'BridgeEndPanel_S'	-5	-5	-5	-5	2	0	0	0	0
'Deck'	-4	-4	-4	3	0	0	0	0	0
'Parapet_E'	2	0	0	0	0	0	0	0	0
'Parapet_W'	0	0	0	0	0	-3	-20	30	6
'Sidewalk'	0	0	0	-1	-5	0	0	0	0
'Wingwall_NL'	0	0	-10	0	0	0	0	0	0
'Wingwall_NR'	0	0	0	0	0	0	0	0	0
'Wingwall_SL'	0	0	6	0	0	0	0	0	0
'Wingwall_SR'	0	0	0	0	0	0	0	0	0

Table 4.6 Differences in as-built POC (manual-based) and as-built POC (Framework-based) for all the bridge elements on different scan dates (%)

Differences in POC (%)	**6/22**	**7/6**	**7/13**	**7/24**	**8/1**	**8/14**	**8/22**	**9/4**	**10/22**
'Abutment_N'	-2	2	-12	0	0	0	0	0	0
'Abutment_S'	5	5	-11	0	0	0	0	0	0
'BridgeEndPanel_N'	-1	-1	0	0	0	0	0	0	0
'BridgeEndPanel_S'	-2	-2	0	0	0	0	0	0	0
'Deck'	-2	-2	-4	-3	0	0	0	0	0
'Parapet_E'	-2	0	0	0	0	0	0	0	0
'Parapet_W'	0	0	0	0	0	0	-23	-30	-6
'Sidewalk'	0	0	0	1	5	0	0	0	0
'Wingwall_NL'	0	0	12	0	0	0	0	0	0
'Wingwall_NR'	0	0	0	0	0	0	0	0	0
'Wingwall_SL'	0	0	-2	0	0	0	0	0	0
'Wingwall_SR'	0	0	0	0	0	0	0	0	0

The framework used in this study produced unacceptable results, i.e. POC values, for some of the elements. These values are highlighted in the red cells. For example, for the scan that was collected on July 13, 2018, the northbound abutment (Abutment_N) and the

southbound abutment (Abutment_S) both show 15% error. Referring to the as-built scans, the formwork was set in place for both abutments on that date. The planned POC (Table 4.4) shows a value of 50%. This value was set to 50% from 35% on the previous scan date to indicate that installation of the formwork amounted to an additional increase in progress. Note that the right half (approximately 35%) of both abutments had been constructed by this date. The framework calculates the POC based on the area of the convex hull spanned by the outermost points of the upper most face of the bridge element. The convex hull algorithm discards points that are disconnected from the main cluster of points that accurately represent the as-built status of the element. Figure 4.16 shows that the points encircled in blue are sparser compared to the points encircled in yellow. Thus, only the ones in yellow are considered in the convex hull calculations. Although the algorithm was specifically designed to handle cases, such as the one shown in Figure 4.17, it poses a limitation for certain cases.

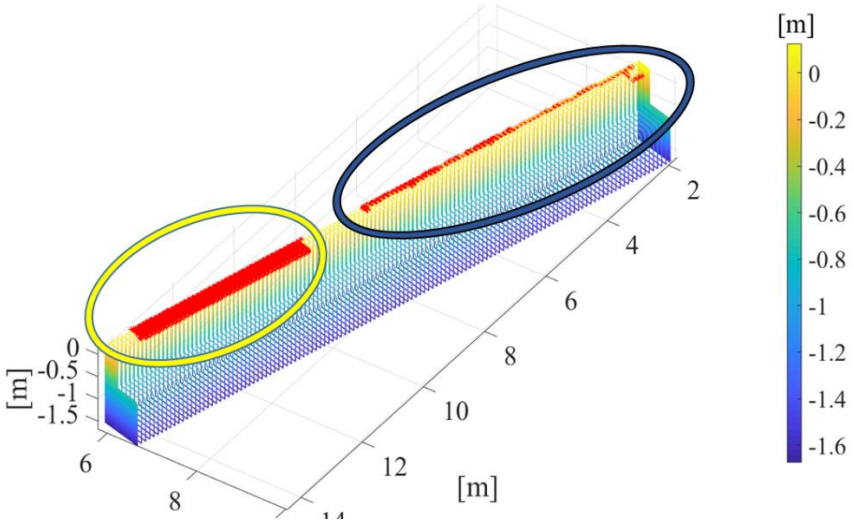

Figure 4.16 Virtual point cloud of southbound abutment with the point cloud representing the as-built status of the same element (red). The points encircled in yellow were included in convex hull calculations whereas the points encircled in blue are discarded.

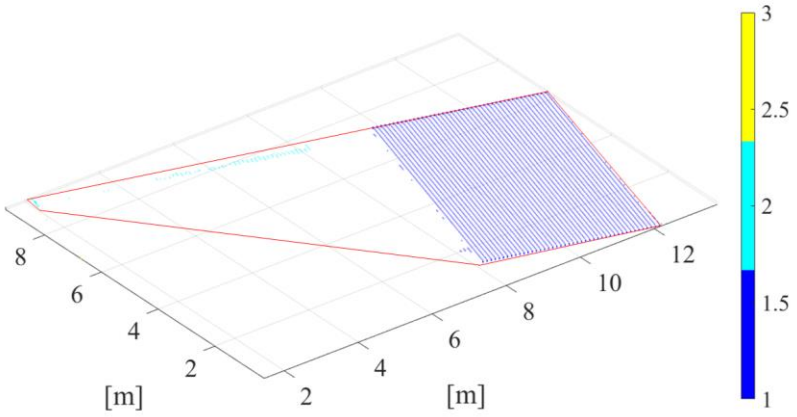

Figure 4.17 Outliers (in light blue) causing significant error in the convex hull calculations. The convex hull algorithm is designed to discard those points and keep the purple points.

Table 4.5 also shows erroneous values for the western parapet (Parapet_W) on scan dates August 22, 2018 and September 4, 2018. The corresponding values for this element in Table 4.3 shows that the western parapet is set to be 50% and 100% completed, respectively, on those dates. 50% was set for August 22, 2018 since most of the formwork and reinforcement bars had already been set up on that day. On scan date September 4, 2018, the parapet was complete. Figure 4.18 illustrates that the convex hull calculations did not account for the surface correctly. This is attributed to the fact that railings were not included in the 3D model and the top of the parapet was not modeled precisely to account for the placement of railings. Based on the provided schedule, it is assumed that the completion of the parapet signifies the completion of the railings placement. Similarly, this explanation applies to the error obtained (-10%) for the left northbound wingwall (Wingwall_NL) in the scan collected on July 13, 2018.

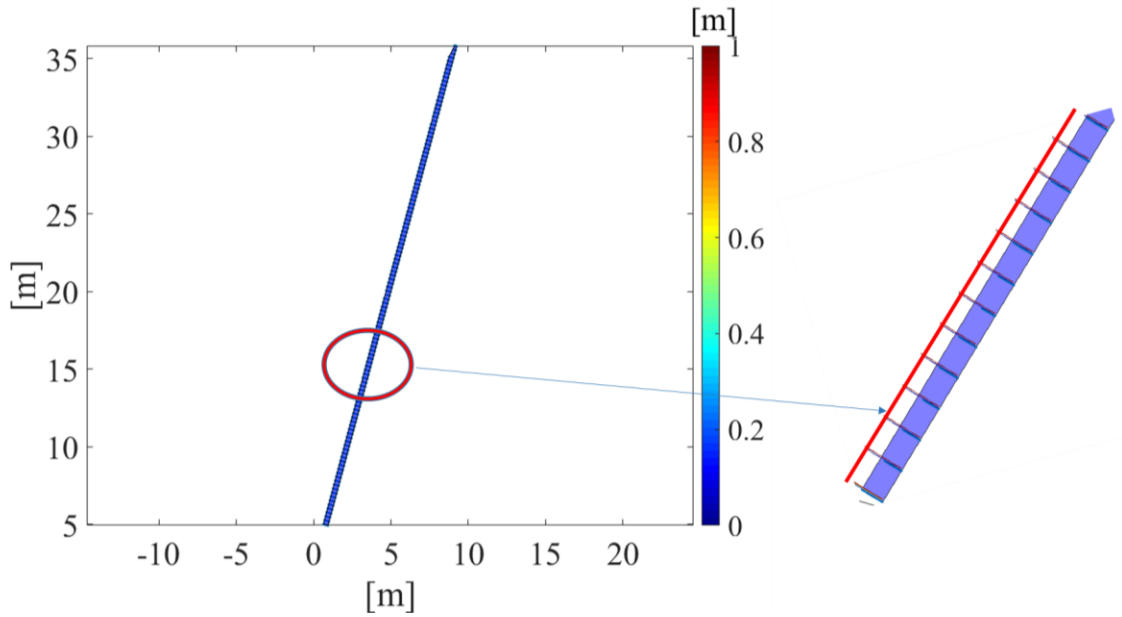

Figure 4.18 Western parapet convex hull (August 22, 2018). The right part represents an enlarged view of the convex hull. The red line on the enlarged section on the right side represents the extent of the area that should have been covered, and the blue region represents the area that was covered.

4.4 Discussion and Limitations

The performance of the progress tracking framework was tested using the data collected from Truax Creek Bridge construction project. The performance of the framework was reflected in the difference between as-built POC (framework-based) and as-built POC (manual-based) values, as shown in Table 4.6.The quality of the progress tracking results, i.e. the POC values, are sensitive to numerous factors. For instance, the number of passes during the data collection can affect the density of the point cloud data obtained, which could impact the POC values. At the same time, the number of passes made during each data collection cycle has a direct impact on data collection time. The future research should investigate the number of passes required to obtain optimum results. The limitations of the proposed framework are detailed below.

4.4.1 Amount of Manual Effort Required

Although the framework automatically computes the POC values, there are manual tasks which should be performed to support the automated processes described in the framework. The presence of false positives directly impacts the POC calculations. Thus, the initial process of manually removing false positives should be performed carefully. The removal process of false positives should ensure that points not belonging to the structure or part of the structure are completely removed. Figure 4.19 and Figure 4.20 illustrate this problem.

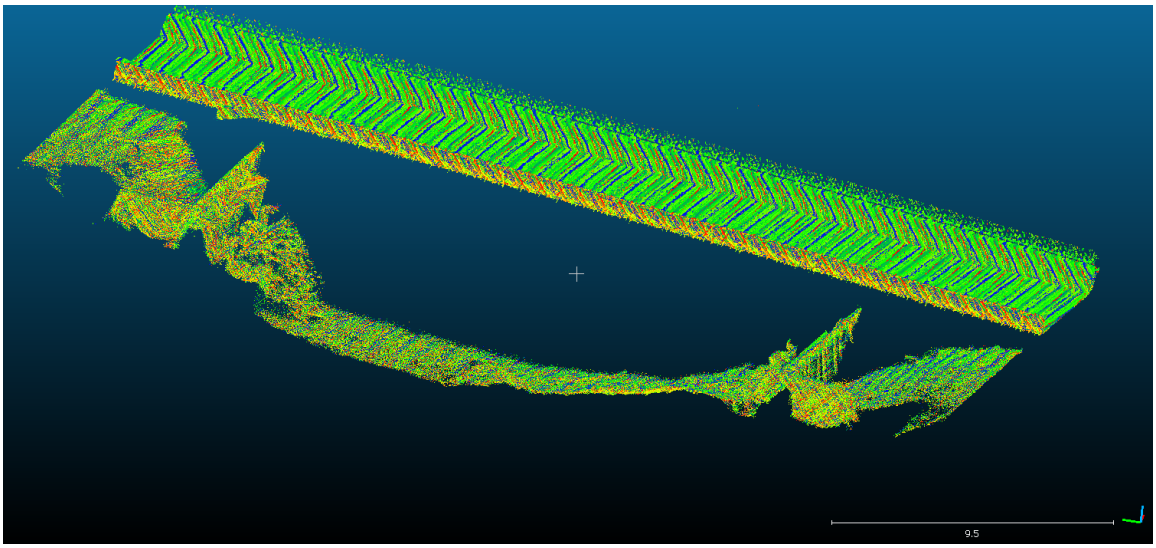

Figure 4.19 Scan data collected on July, 13, 2018

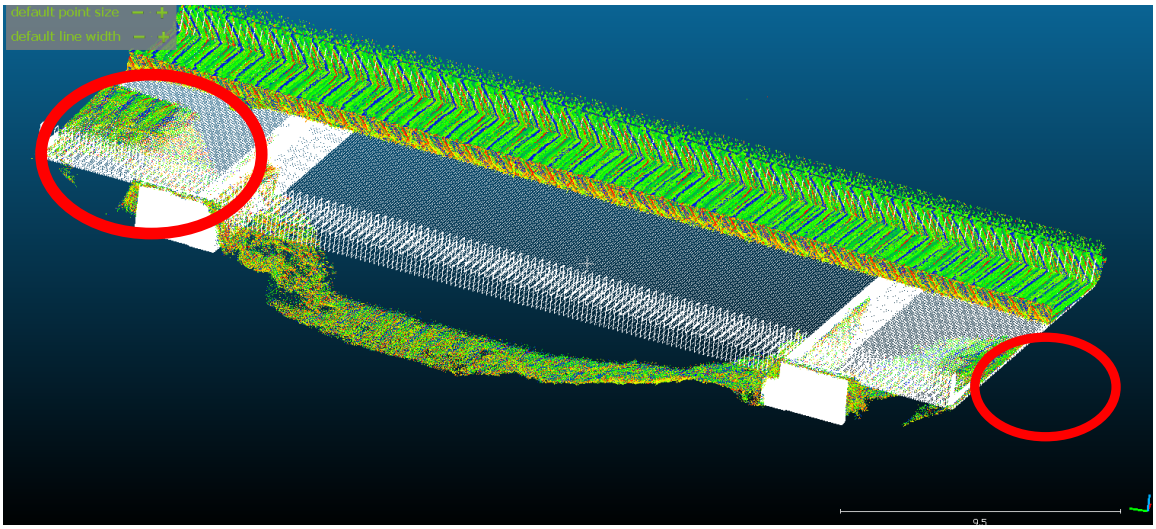

Figure 4.20 Scan data overlapped with the finely registered original virtual point cloud. Regions of unwanted overlap bounded by red circles (Scan date: July, 13, 2018.)

As shown in Figure 4.20, the part of the original virtual point cloud corresponding to the two bridge end panels have overlapped with the original as-built scans. During the object recognition phase, the progress of panels will be reported as "under construction", and will be assigned a percentage of completion, based on the percentage of overlap between the original virtual point cloud and the original as-built scans. Carefully cleaning the point cloud will result in better detection results. In addition, manual work was required for separating the road surface from the rest of bridge structure for the ACWS layer detection. Future work will focus on improving the framework to enable automatic segmentation of road surface from the as-built data.

4.4.2 Accuracy of the Mobile Mapping System

Figure 4.11 shows that approximately 3-4 cm noise was present in the as-built data. The presence of noise directly affected the selection of the threshold during the fine registration and segmentation steps. The limitation can be overcome by using a more accurate scanning system, such as the Pegasus mobile mapping system, or a terrestrial laser scanner. Consequently, the threshold could be lowered by approximately 3 – 4 cm, which should improve the accuracy of the POC calculations.

4.4.3 Manual processing time per epoch

Table 4.7 summarizes the approximate time taken for the manual and automated processes in the framework, including the software used for each step. Note that the orange color denotes processes that need to be performed only once. The blue color represents processes that have to be performed multiple times (refer to the comments column). Apart from manual processes that are required to be performed only once (highlighted in orange), the data processing time required for each epoch takes approximately 1 hour and 15 minutes. Please note that if a 3D project design at Level of Development (LOD) 300 is already available, it can be converted into STL format directly, which would lower the time required for processes to be performed manually at the beginning of the project (processes highlighted in orange) down to approximately 12 minutes. 3D models are becoming more and more commonly used for infrastructure projects; hence, this time window would not need to be considered as time to utilize this workflow for progress monitoring.

Table 4.7 Time taken for manual tasks for the proposed framework for the case study

Process	Software used	Time Taken	Comments
Data Collection			
Average time required for each data collection cycle	N/A	20 mins	Time includes 2-3 passes, depends on bridge length
Data Download and Upload to external hard drive (4 TB)	N/A	2 mins	For 15-20 GB file size, depends on data storage device used
Manual Processes			
Development of 3D model (equivalent to BIM Level of Development 300 (LOD 300))	Autodesk Revit	4-5 hours	Time includes studying 2D drawings
Creation of as-planned POC table	MS Excel	10 mins	
Generating STL files	Gmsh	2 mins	Per STL file
Manual Processes (per epoch)			
Point cloud pre-processing Geoclean	TOPCON Geoclean	20 - 30 mins	Per as-built point cloud
Point Cloud Cleaning (after preprocessing)	CloudCompare	15 mins	Per as-built point cloud
#Coarse Registration	CloudCompare	20 mins	Per set of as-built point cloud and virtual point cloud
Automated Processes			
Fine Registration Step (Approximate value, depends on size of point cloud)	MATLAB	15 mins	Per set of as-built point cloud and virtual point cloud, includes the time required for one-to-one matching
Segmentation, Object Recognition and POC calculations	MATLAB	5 secs	Per virtual point cloud of an object

Table Notes:

The Coarse Registration step can be avoided by using a consistent coordinate system for the models and the mobile lidar data.

5 Assessment of Compliance of Dimensional Tolerances in Concrete Slabs using TLS data and the 2D Continuous Wavelet Transform

5.1 Summary

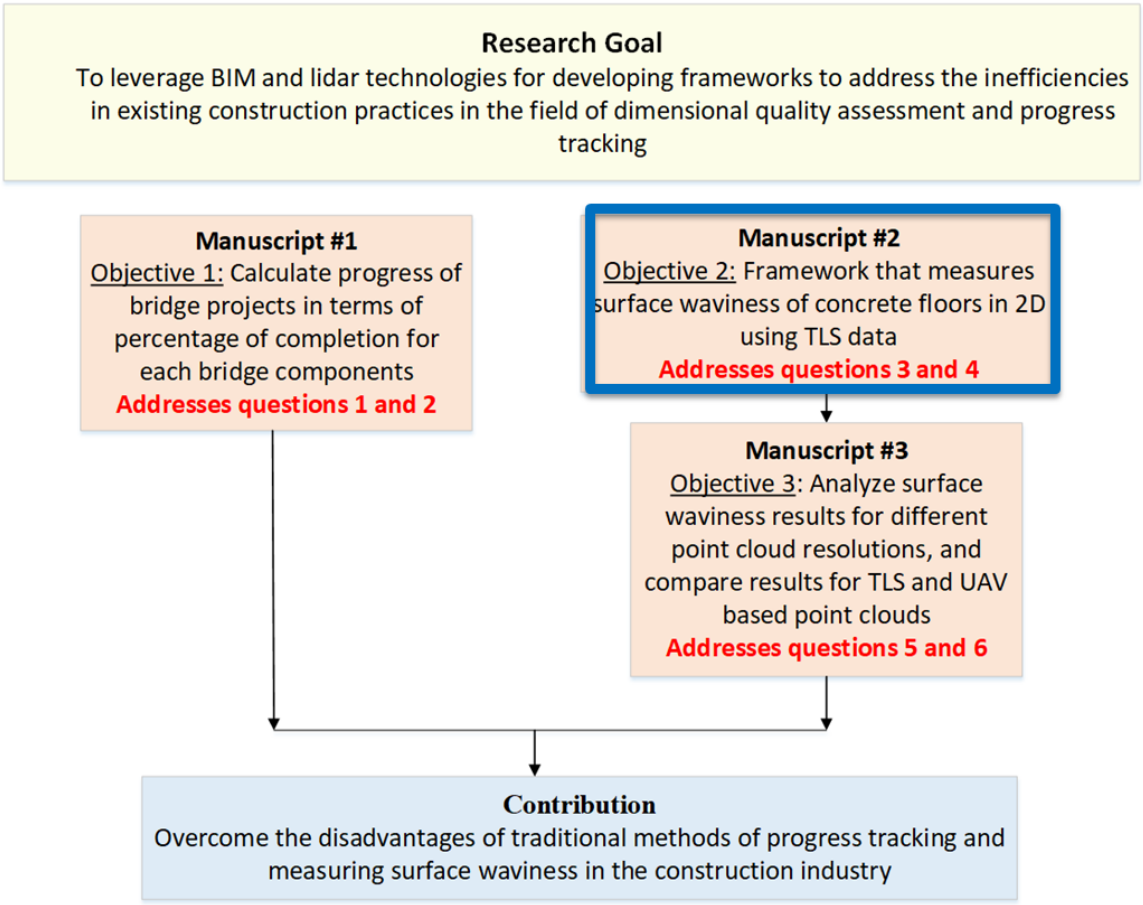

Figure 5.1 Overall research goal and contribution

Chapter 4 presented a framework that combines and processes mobile lidar data and 4D design models to track the progress of bridge construction projects, and addresses the problems related to cost and schedule overruns. The objective of Chapter 5, as shown in Figure 5.1, is to address the issues related to dimensional quality control in construction. Chapter 5 achieves this by proposing a framework that uses TLS to obtain accurate waviness information about newly constructed and existing concrete surfaces rapidly. This paper presents a methodology that applies the two-dimensional Continuous Wavelet Transform (2D CWT) to TLS point clouds to measure concrete slab surface waviness. The

approach builds on preliminary works published in [138] [150], but presents and analyses it in a more comprehensive manner. The proposed methodology is designed to help carry out tolerance compliance control tasks for slabs based on project specifications describing their waviness tolerances. Uniquely, the methodology is able to perform an accurate and comprehensive assessment of the surface geometry in both spatial and frequency domains.

5.2 Proposed Methodology

The proposed methodology is summarized in Figure 5.2. The raw 3D point cloud consists of data points from a concrete slab as well as its surrounding environment, including workers, equipment and surrounding buildings. The point cloud is typically the result of multiple laser scans co-registered using a standard (reliable) target-based approach. First, the raw point cloud is pre-processed to isolate the area of interest, the concrete slab in this case, from the raw point cloud. The next step is to develop a depth map, which is used as input to the 2D CWT. The areas with undulations corresponding to various characteristic periods are identified after applying the 2D CWT with the Mexican Hat wavelet.

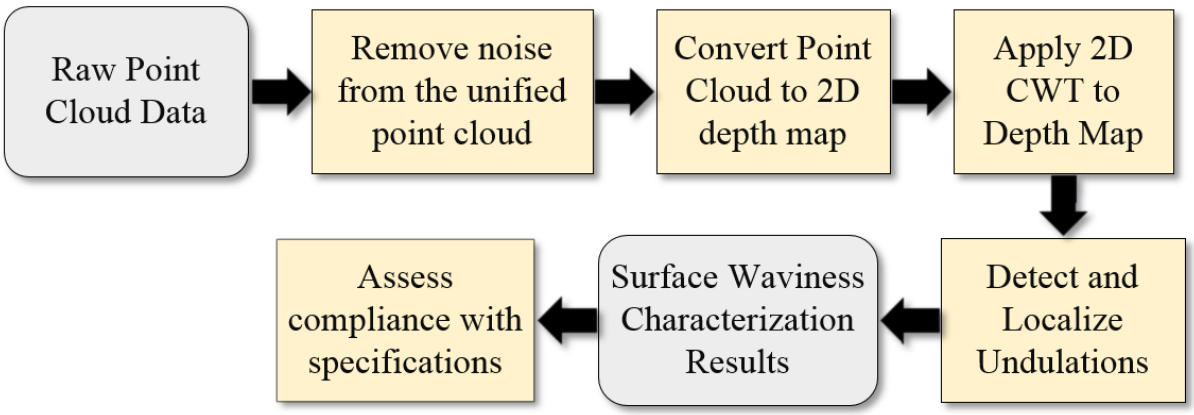

Figure 5.2 Overview of the research methodology

5.2.1 Data pre-processing

As stated in the overview of the research methodology, the raw point cloud data should be pre-processed before 2D CWT can be applied to it. The input is a raw point cloud that may be the result of the co-registration of multiple scans collected during the scanning process. The noise present in the registered point cloud data is removed using a corresponding functionality provided by a commercial point cloud processing software, leaving a clean point cloud of the area of interest (i.e. concrete slab). The pre-processed point cloud corresponding to the slab surface is aligned (parallel) to the x-y plane, which is likely to be the case already. Accordingly, z coordinates represent the elevation of each point, facilitating further analysis.

In order to analyze the frequencies of undulations present on the surface, the point cloud data should have equispaced rows and columns along the x and y axes [151]. Because raw point cloud data from slabs typically has a random arrangement, it is converted into a regular grid, with intervals along the x and y axes were both set to δ_p = 1 cm. This sampling interval ensures robust localization of defects across the 2D surface. Triangulation-based linear interpolation is used to obtain the values of z-coordinates at each grid point. Consequently, a 2D depth map is created, which represents the height of the surface for points at δ_p = 1 cm intervals along the x- and y-axes.

5.2.2 Detection of Undulations using 2D Continuous Wavelet Transform

The depth map resulting from the previous operation is used as the input "signal" to the 2D CWT. The scale a at which the CWT is applied relates to a few parameters, as in Equation 5.1 [115]:

$$a = \frac{f_c}{f \cdot \delta_p} = \frac{T \cdot f_c}{\delta_p} \qquad (1.1)$$

where f represents the frequency of the undulation, T the characteristic period of the signal, and f_c, the main frequency component of the Fourier Transform of the mother wavelet. For the Mexican Hat wavelet, $f_c = 0.252$ cm^{-1}.

The output of applying the 2D CWT is a series of scalograms that report the CWT response at each grid point on the depth map. These maps are meaningful to some extent, but should be further processed to accurately define the exact characteristic period at each location. Indeed, a wavy region will result in peak responses at several scales, i.e. frequencies, as can be seen in Figure 5.6 for example. However, not all those peaks correspond to defects whose size matches the period associated to that scale. First, peak values (i.e. local maxima) are detected in each 2D CWT response map. Next, different isolines are then calculated around each peak, which connect pixels with the same CWT response. These isolines may describe irregular shapes whose mathematical analysis, and further comparison with other defects, can be truly complex. Therefore, areas enclosed by isolines are described by means of ellipses, and the two main axes of each ellipse are determined to be used as reference values. If any of the axes matches the period associated to the scale of interest, a surface deviation is detected in that area for that particular period. The result of this process is a set of clear waviness defect detections at all the scales/periods considered, which can be combined in a single diagram.

5.2.3 Correspondence between WI and 2D CWT methods

The correspondence between the WI method and the 2D CWT method in terms of their response to similar surface wavelengths (or periods) is shown in Table 5.1. The k values of the WI method correspond to characteristic periods of different lengths. The corresponding CWT scales for each of these k values are calculated using Equation 5.1 with $\delta_p = 1$ cm. The characteristic periods (T) selected in this table represent the floor undulations, with periods of 0.61, 1.22, 1.83, 24.4 and 30.5 m (2, 4, 6, 8 and 10 ft) that are the focus of the WI method.

Table 5.1 Continuous Wavelet Transform scales and equivalent Waviness Index [22]

Characteristic period (T) [cm]	**CWT scale (a)**	**Waviness Index (k values)**
61	15	1
121.9	30	2
182.9	45	3
243.8	60	4
304.8	75	5

5.3 Experimental Results

5.3.1 Data Collection and Pre-Processing

An in-situ concrete slab from a warehouse project in Gresham, Oregon was scanned after 5-6 hours of placement. The surface of the concrete slab was sturdy enough for foot traffic and for setting up the tripod of the scanner. The concrete slab of the warehouse building was scanned using a Leica ScanStation P40 3D laser scanner. The scanner has 8" horizontal and 8" vertical angular accuracy. The 3D position accuracy is ±3mm at 50 m and ±6 mm at 100 m [152].

Figure 5.3 shows the plan view of the concrete slab as well as one of the 3D point clouds captured. The area of interest with a surface area of approximately 1500 m^2 is highlighted in both the plan view and the point cloud. It was determined that scans taken from four different locations would be sufficient to capture the surface with sufficient detail. Six targets were placed at different locations on site to facilitate the point cloud registration process.

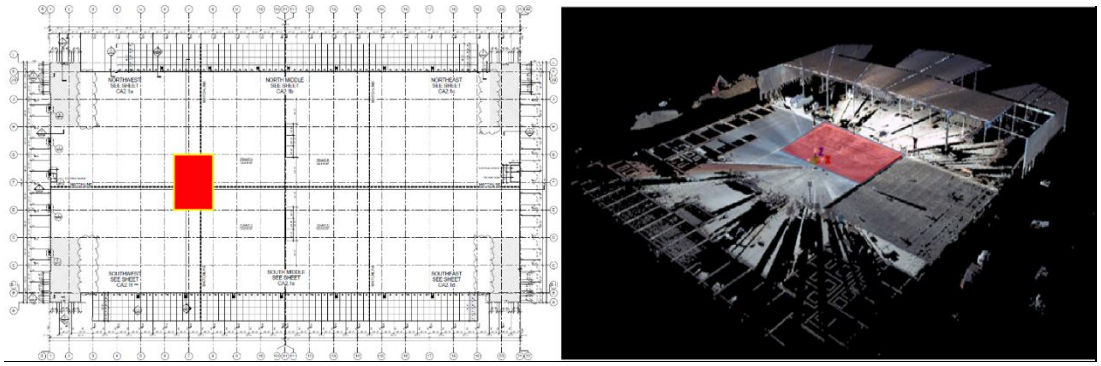

Figure 5.3 The floor plan (left) and the 3D point cloud (right) of the warehouse building. The area of interest is highlighted in red.

The overall scanning process, including setup, scanning, dismantling and re-locating, took approximately 45 minutes. The data pre-processing stage, comprising of registering the point clouds in the same coordinate system and removing the noise, took 50 minutes. The raw point clouds, i.e. laser scans including noise, were first imported into a commercial point cloud processing software. The four laser scans were registered under the same coordinate system using the targets placed at strategic locations on the construction site. After the registration was complete, the point cloud of the area of interest was manually isolated from the rest. The point cloud corresponding to the slab section of interest had approximately 100,000,000 points. Figure 5.4 shows an image of the scan after registration and noise removal.

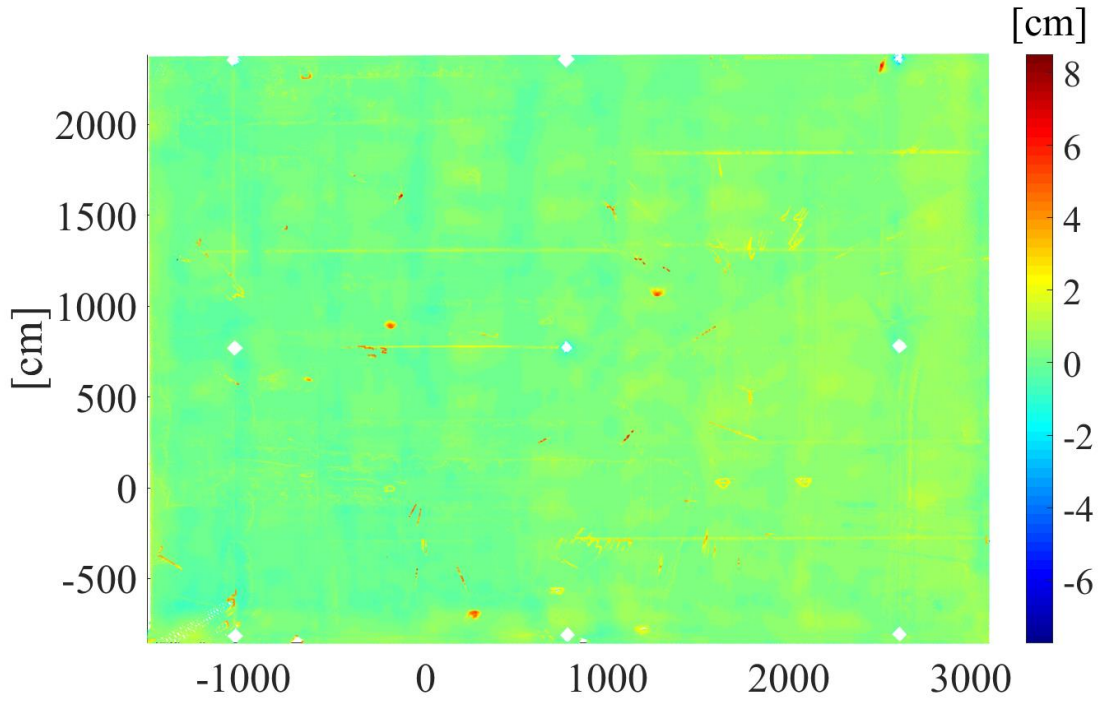

Figure 5.4 Top view of the point cloud of the area of interest obtained after the registration of the four scans and noise removal. The color scale represents elevation values in cm.

5.3.2 Data Processing

Following pre-processing, the point cloud is converted into a 3242 x 4629 depth map with 1 cm intervals in both horizontal and vertical directions, with the z-coordinates at each grid point calculated as described in Section 5.2.1. Figure 5.5 shows the resulting depth map. As seen in Figure 5.5, the height of the concrete slab with respect to the xy plane, varies most in the interval of -2 cm to 2 cm. Thus, the color map was adjusted accordingly to highlight the height differences between various areas across the floor.

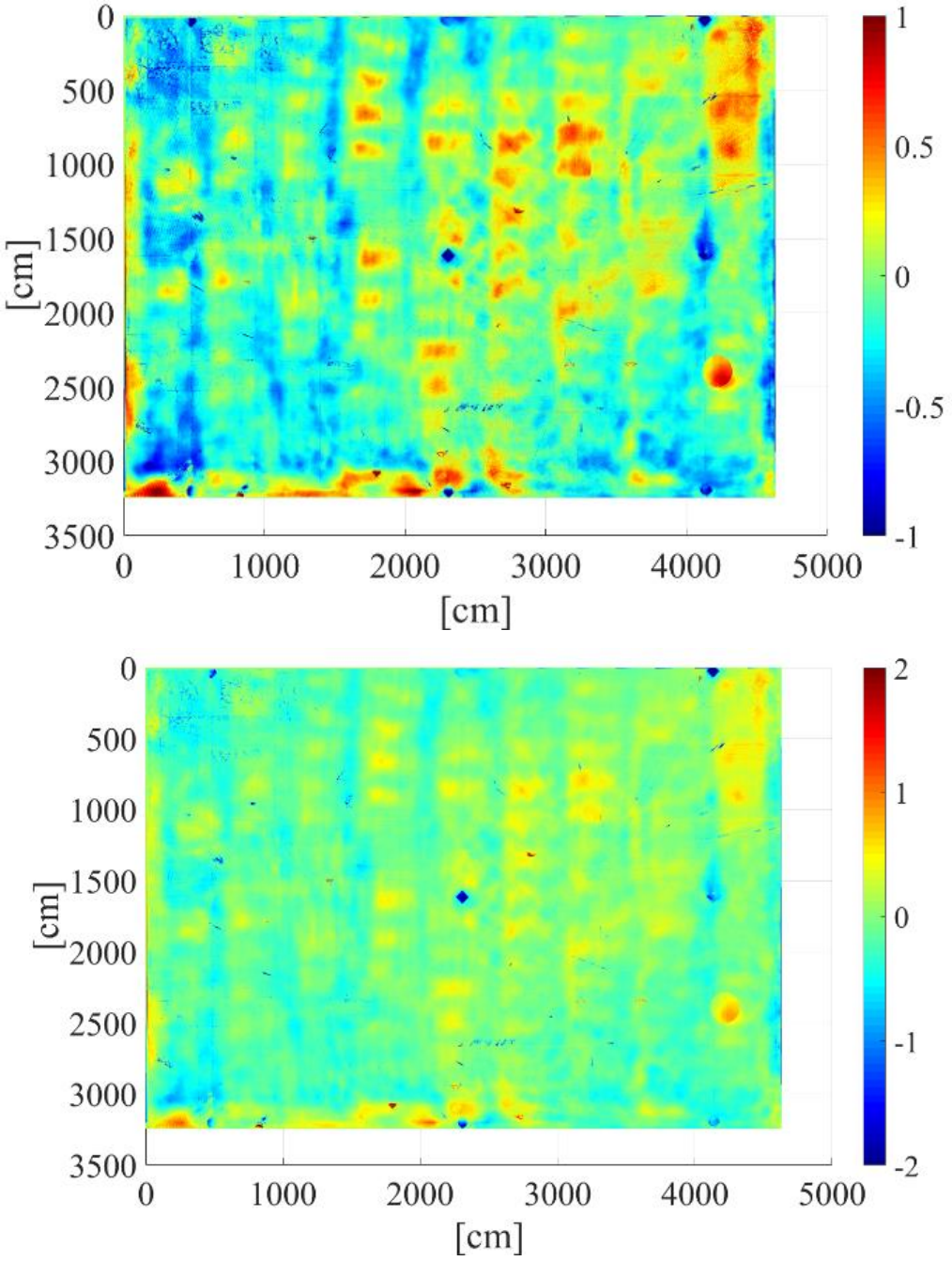

Figure 5.5 Depth map derived from the TLS data, with color map limits set to [-1, 1] cm (left) and [-2, 2] cm (right)

5.3.3 CWT Results

5.3.3.1 CWT Scalogram

Figure 5.6 presents the results obtained using the scales (a) 15, 30, 45, 60 and 75 of the mother wavelet. The regions where the input “signal” strongly correlates with the mother wavelet applied at the scales above are highlighted in yellow in Figure 5.6.

The point cloud in Figure 5.4 and the depth maps in Figure 5.5 show that the surface of the investigated slab is relatively flat with a few “peaks”. For the entire slab surface, the average value of the deviation in the z-axis was 0.0 cm with a standard deviation of 0.3 cm. Figure 5.6(a) represents the regions where the wavelength of the undulations present on the surface correlates with the mother wavelet of scale 15. The scalogram shows that the regions near (1900 cm, 3100 cm) has an undulation of this characteristic period present on the slab surface. Figure 5.6 (b) shows regions near (1900 cm, 3100 cm) and (2400 cm, 1700 cm) have undulations that correspond to the mother wavelet of scale 30. Similarly, the scalograms in Figure 5.6 (c), (d) and (e) show that the region near (2400 cm, 1700 cm), (300 cm, 3400 cm) and (4200 cm, 2400 cm) have undulations corresponding to scales 45, 60 and 75. The region near (2400 cm, 1700 cm) shows responses for all these three scales. Thus, the identification of the scale which has the top response at that location is necessary. Furthermore, such analysis is an added advantage of using the proposed 2D CWT method and cannot be done using the WI method.

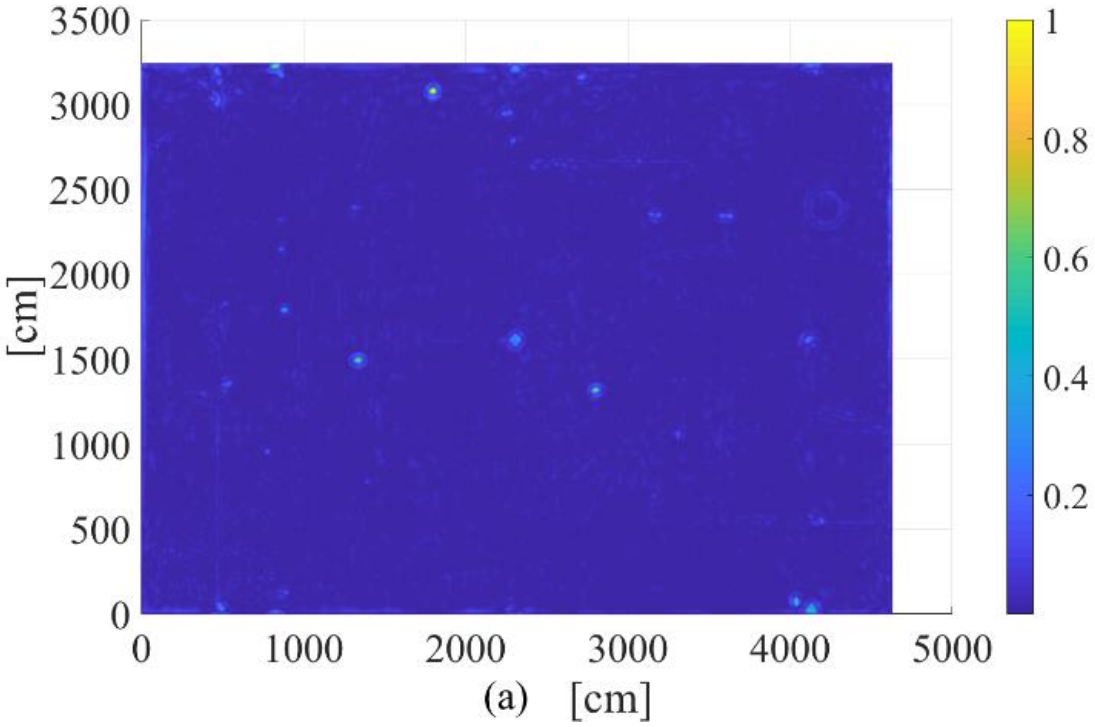
3500
3000
2500
2000
1500
1000
500
0
[cm]
0
1000
2000
3000
4000
5000
(a) [cm]
1
0.8
0.6
0.4
0.2

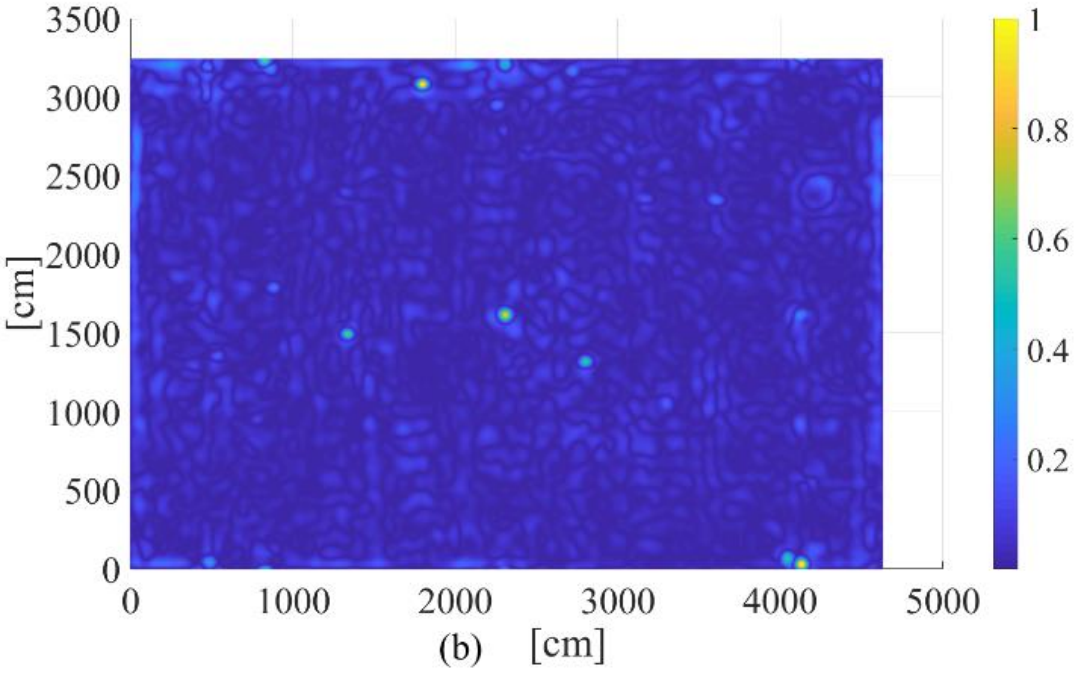
3500
3000
2500
2000
1500
1000
500
0
[cm]
0
1000
2000
3000
4000
5000
(b) [cm]
1
0.8
0.6
0.4
0.2

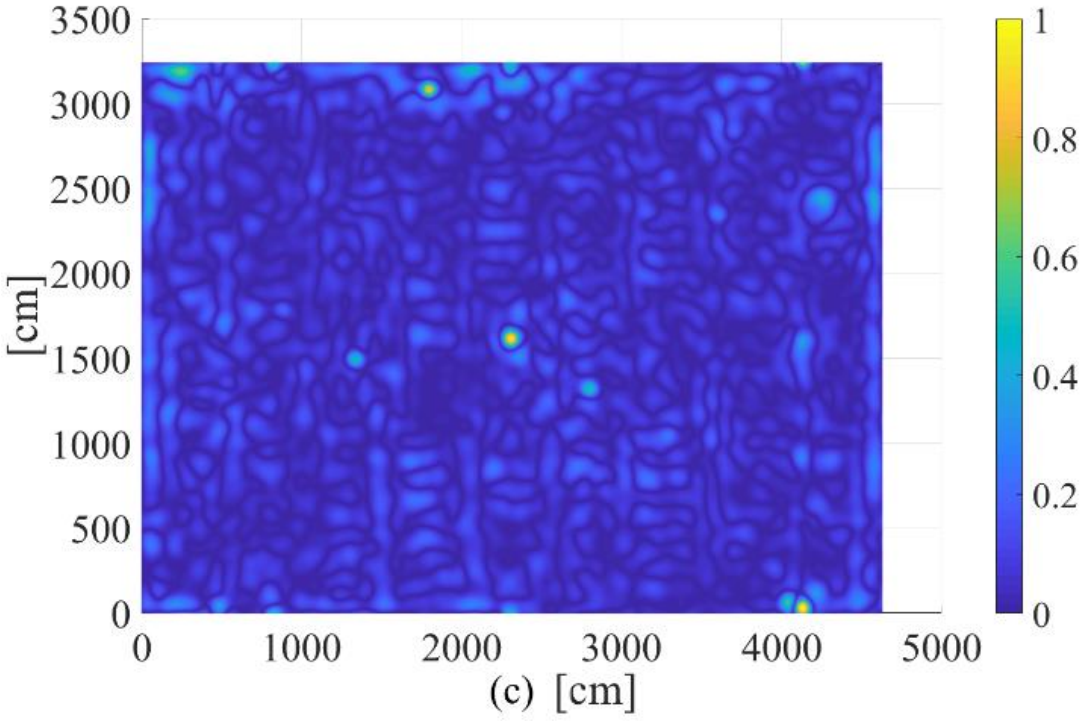
3500
3000
2500
2000
1500
1000
500
0
[cm]
0
1000
2000
3000
4000
5000
(c) [cm]
1
0.8
0.6
0.4
0.2
0

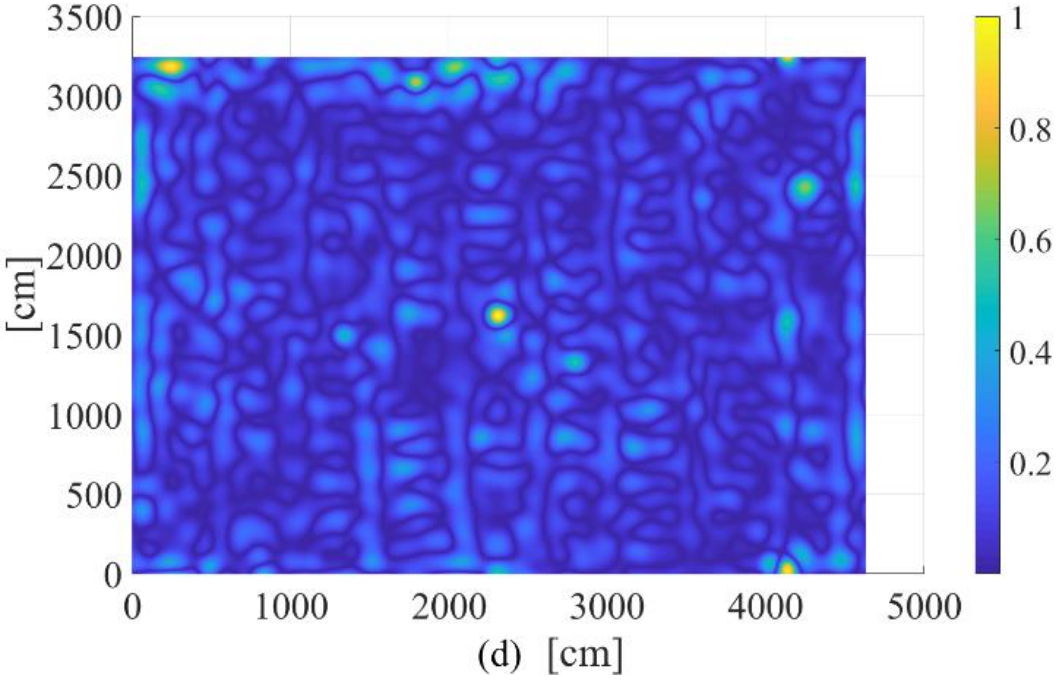
3500
3000
2500
2000
1500
1000
500
0
[cm]
0
1000
2000
3000
4000
5000
(d) [cm]
1
0.8
0.6
0.4
0.2

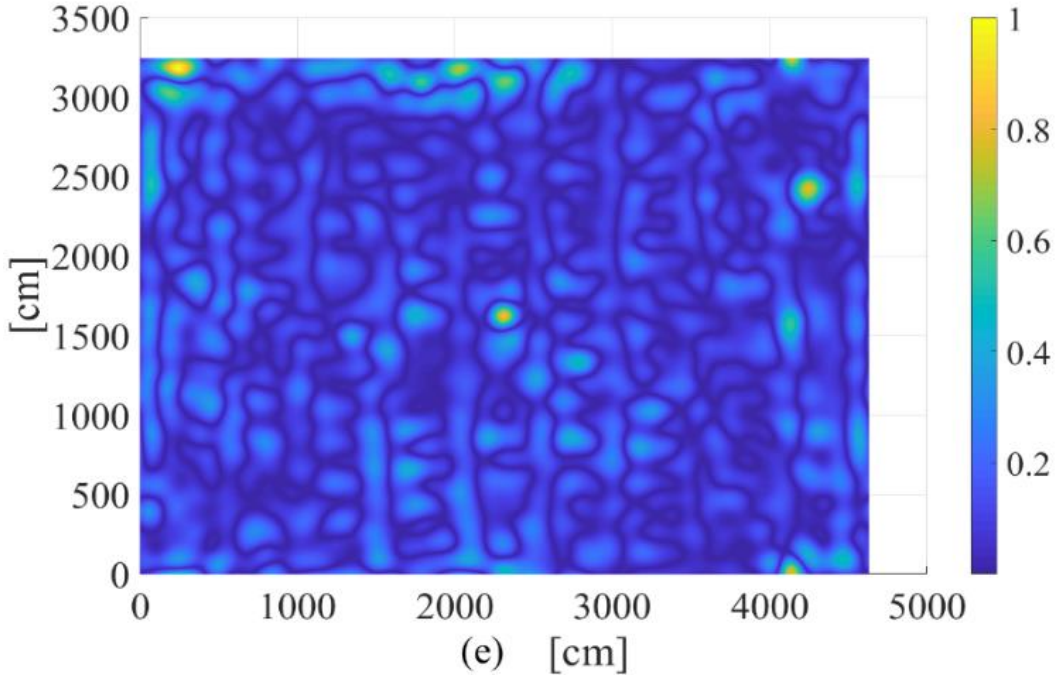

Figure 5.6 The coefficients obtained from the wavelet transformation corresponding to scales 15 (a), 30 (b), 45 (c), 60 (d) and 75 (e) are plotted on the map. The areas in the slabs where undulations corresponding to these scales are present are shown.

5.3.3.2 Surface analysis and automatic defect detection

Figure 5.7 illustrates regions, enclosed by ellipses, where potential defects have been identified for two of the five scales in Figure 5.6. Note that no defective regions were found for the other three scales.

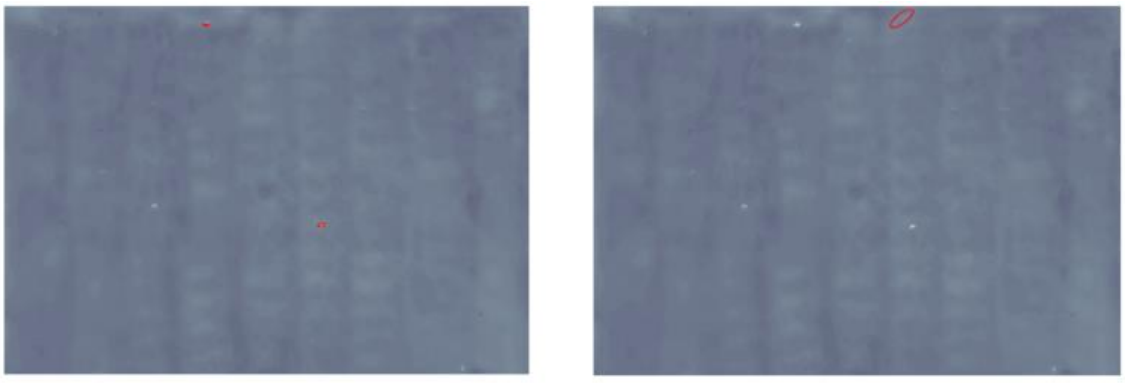

Figure 5.7 Potential defective areas for a) 61cm (±2cm) and b) 244cm (±2cm).

The advantage of our approach is that it combines dense 3D data from TLS with the 2D CWT that can support the analysis of waviness with essentially any characteristic period (i.e. wavelength). This enables our approach to study waviness not just for a few discrete wavelengths (like the 5 above), but for dense and large ranges of wavelengths. This is demonstrated in Figure 5.8 that summarizes the potential defects on the slab for any wavelength within the continuous range of 20 to 400 cm.

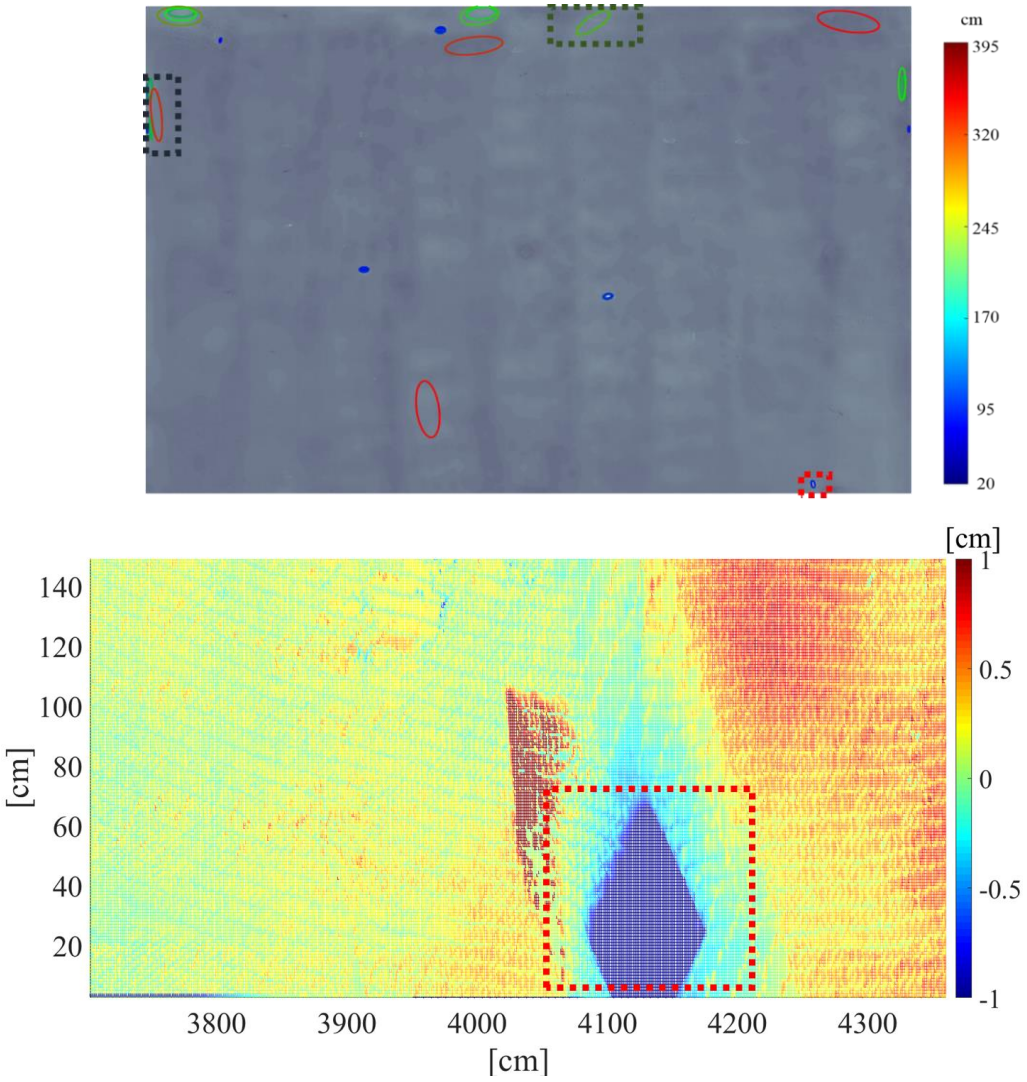

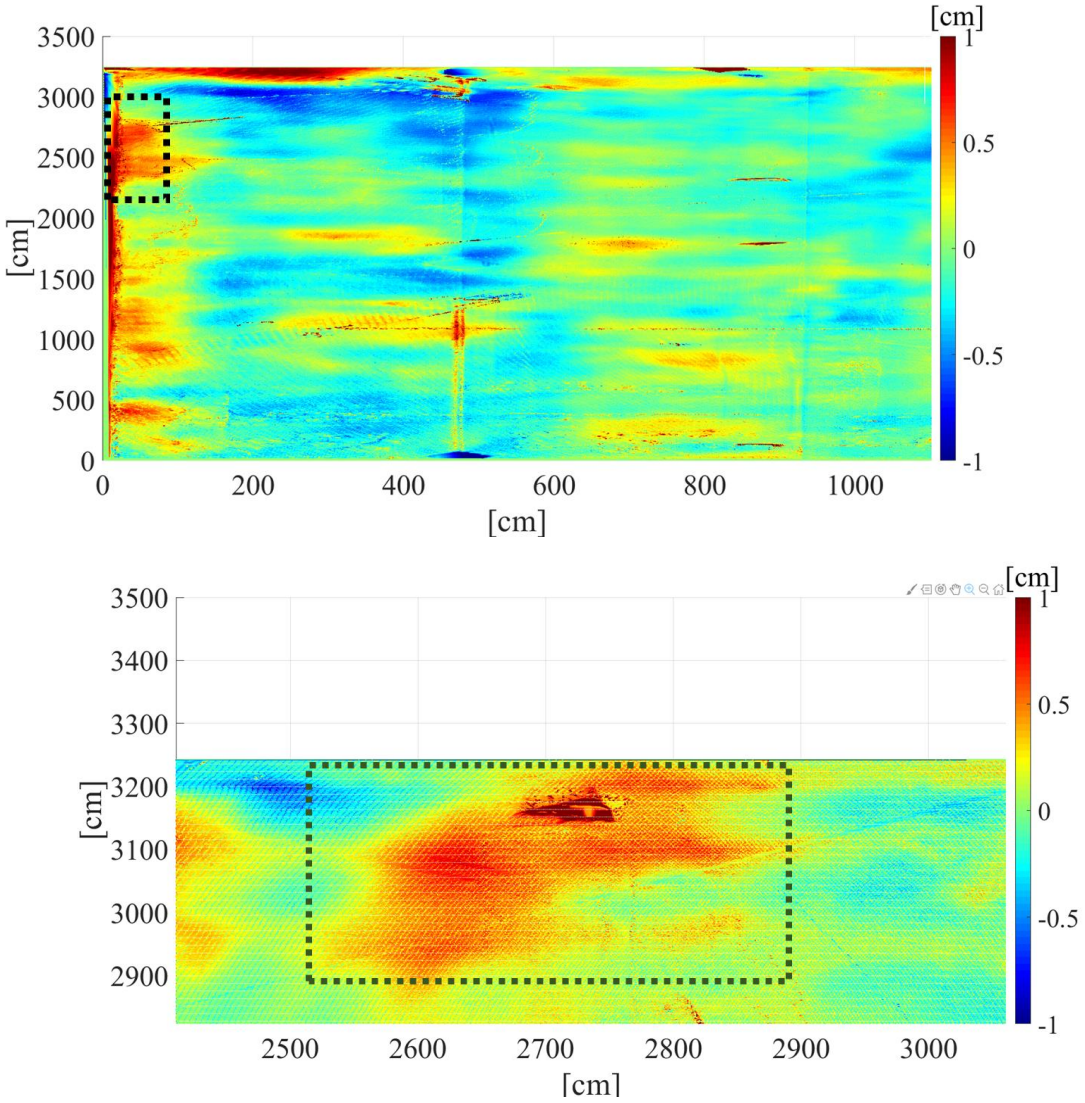

Figure 5.8 Detected defects for periods between 20 and 400 cm, with area within the dotted rectangles showing close-up views for the corresponding regions in the depth map

5.3.4 Comparison of Results with WI method

The ASTM E1486-14 standard describes the test method for measuring the waviness of concrete floors using the WI method. In a similar way to [22], we propose to apply the WI method as defined in this standard, but using the digitized slab surface as the surface of application (instead of the real slab). Referring to this standard, 103 survey lines along the x-axis and 148 lines along the y-axis were defined on the slab, as shown in Figure 5.9.

The lines are spaced at 1-ft intervals. This is much denser that what would normally be achieved in normal practice, but is useful to conduct the comparison with the proposed CWT approach.

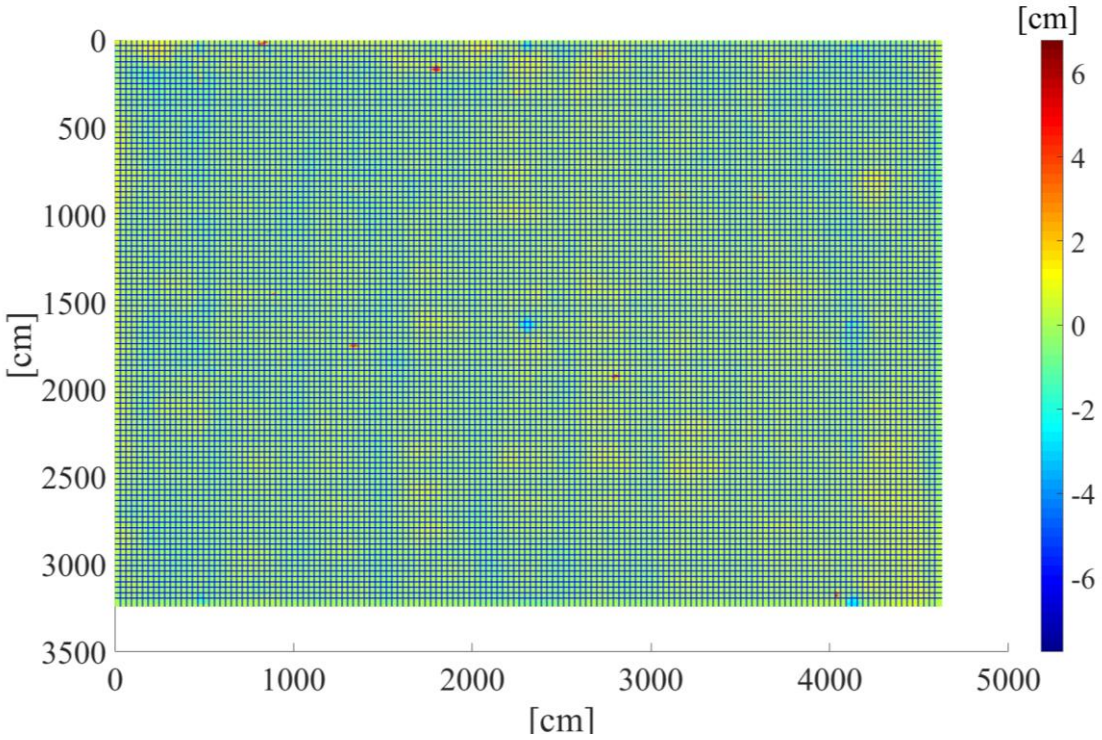

Figure 5.9 The 251 survey lines (103 along the x-axis and 148 along the y-axis) that are defined across the slab surface.

The length adjusted RMS deviation (LAD) responses are calculated for each line. The survey lines are parallel to each other and are spaced at a distance of 30.5 cm (1ft). Survey points with a spacing s=30.5 cm (1ft) are measured along those lines. The standard defines chord length as the length of the imaginary line joining two points on the surface of the concrete floor. The chord length is equal to 2ks, where k= {1, 2, 3, 4 and 5}. The vertical distance between the midpoint of the chord and the survey point on the surface, D_{kj}, is calculated using the following formula,

$$D_{kj} = h_{j+k} - 0.5(h_j + h_{j+2k}) \quad (5.2)$$

where, h_{j+k}, h_j and h_{j+2k} represent the heights of the survey point and the two end points of the chord, respectively.

After the deviation D_{kj} is calculated, the length adjusted RMS deviation (LAD_k) is calculated using Equation 5.3.

$$LAD_{l,k} = \sqrt{\frac{\frac{L_r}{2ks}[\sum_{i=1}^{jmax_{l,k}}(D_{l,k,j})^2]}{jmax_{l,k}}} \quad (5.3)$$

where L_r corresponds to the reference length of 1 ft. $jmax_k$ corresponds to the total number of deviation calculations with a chord length 2ks along a survey line and l denotes the survey line being tested.

Similarly, the 2D CWT responses at the j^{th} sampled location, $CWT_{l,a,j}$, for scales 15, 30, 45, 60 and 75 were obtained in section 5.3.3.1. These scales correspond to the WI k-values 1, 2, 3, 4 and 5 respectively. It is proposed that the CWT responses for each of the 210 lines for those 5 scales, $CWT_{l,a}$, be calculated using the similar formula:

$$CWT_{l,a} = \sqrt{\frac{\sum_{i=1}^{jmax_{l,a}} CWT^2_{l,a,j}}{jmax_{l,a}}} \quad (5.4)$$

where $jmax_k$ corresponds to number of locations at which the 2D CWT response have been calculated.

The correlation between the $LAD_{l,k}$ and $CWT_{l,a}$ responses is calculated to compare the surface waviness results obtained using the WI and 2D CWT methods. 15 survey lines along the x-axis and 15 survey lines along the y-axis, as shown in Figure 5.10, are randomly selected (out of the previously defined 251 lines), to illustrate the correlation results presented in Figure 5.11 and Figure 5.12. The correlation coefficients, denoted by r^2, are included in the top left-hand corner of each graph. The values indicate a strong correlation between the results obtained using the WI and 2D CWT methods. This strongly validates the value of the proposed approach, which has the additional advantage of being able to more precisely define defects' wavelengths and locations (including actual orientation). Table 5.2 provides the summary statistics for the correlation between $LAD_{l,k}$ and $CWT_{l,a}$ responses at five different characteristic undulation periods [61, 121.9, 182.9, 243.8, 304.8] cm for the 30 lines along the x and y axes.

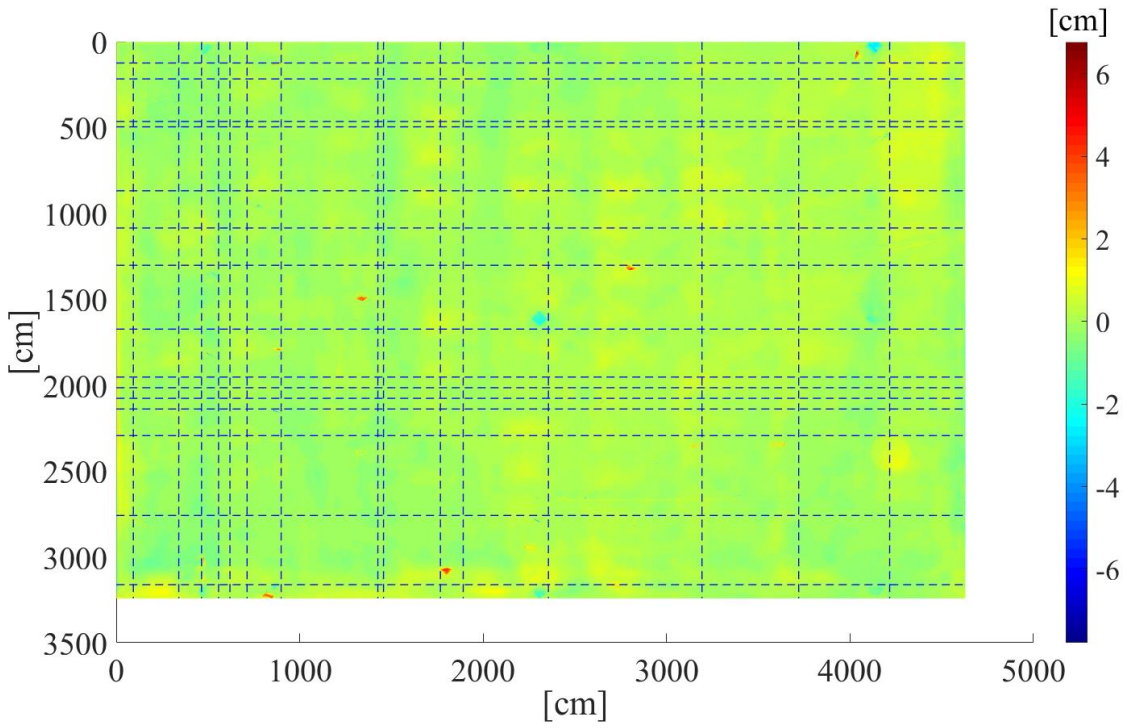

Figure 5.10 The 30 survey lines (15 along each axis) that were selected for the generation of correlation results.

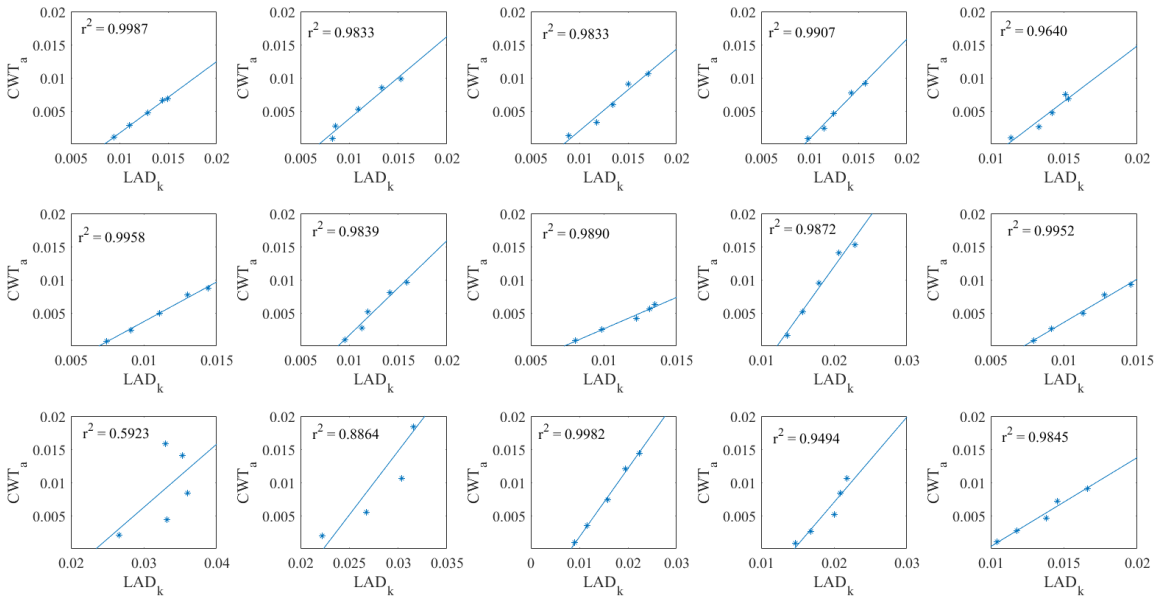

Figure 5.11 Correlation between $LAD_{l,k}$ and $CWT_{l,a}$ responses for the five characteristic undulation periods [61, 121.9, 182.9, 243.8, 304.8] cm, along 15 lines along the x-axis shown in Figure 5.10.

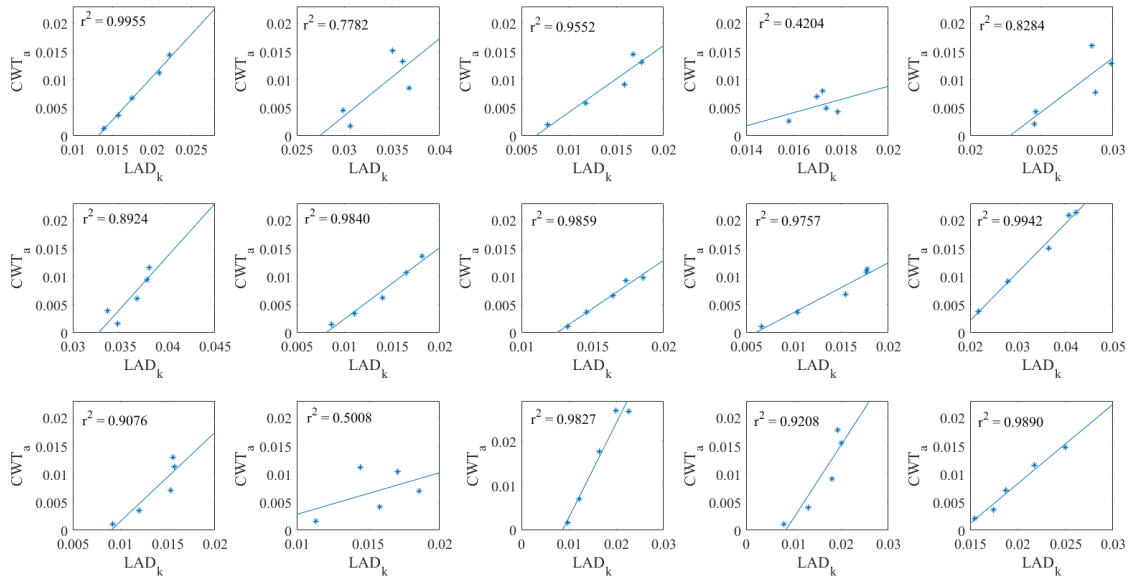

Figure 5.12 Correlation between $LAD_{l,k}$ and $CWT_{l,a}$ responses for the five characteristic undulation periods [61, 121.9, 182.9, 243.8, 304.8] cm, along 15 lines along the y-axis shown in Figure 5.10.

Table 5.2 Summary statistics for the correlation between $LAD_{l,k}$ and $CWT_{l,a}$ responses for the five characteristic undulation periods [61, 121.9, 182.9, 243.8, 304.8] cm, along 16 lines along the y-axis shown in Figure 5.11 and Figure 5.12.

Correlation Statistics	
Minimum	0.42
Maximum	1.00
Range	0.58
Count	30.00
Sum	27.39
Mean	0.91
Median	0.98
Mode	0.9833, 0.9890
Standard Deviation	0.15
Variance	0.02
Mid Range	0.71
Quartiles	
Q1	0.90
Q2	0.98
Q3	0.99
Interquartile Range (IQR)	0.09
Sum of Squares	0.65
Mean Absolute Deviation	0.10
Root Mean Square (RMS)	0.92
Std Error of Mean	0.03
Skewness	-2.23
Kurtosis	6.79
Coefficient of Variation	0.16
Relative Standard Deviation	16.42%

The proposed approach overcomes all of the drawbacks of traditional waviness assessment methods mentioned earlier. The 2D CWT method enables a comprehensive analysis of the waviness of 2D surfaces, both in the spatial and wavelength domains. In contrast to the F-number and WI methods, the output of the CWT-based approach enables easy visual representations of where waviness defects are located on the surface (as shown in Figure 5.6). This can help users with minimal knowledge about 3D TLS or 2D CWT to quickly determine where surface corrections should be applied, for example.

6 Analyzing the Impact of Point Cloud Resolution on Surface Flatness Measurements

6.1 Summary

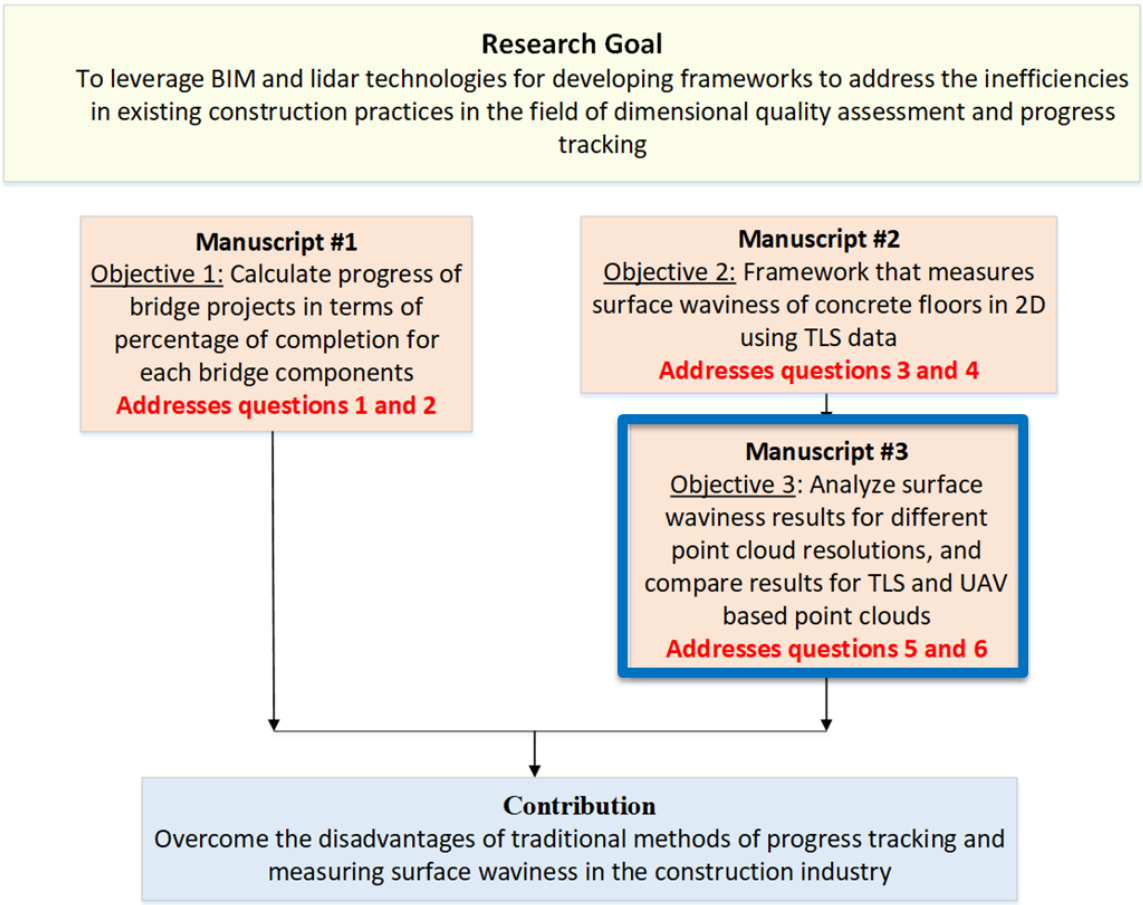

Figure 6.1 Overall research goal and contribution

The study in Chapter 5 presents the framework developed to process 2D as built information in the form of depth maps, as opposed to 1D survey lines derived from TLS-based point clouds to impart waviness information of newly constructed concrete slabs. This study, as shown in Figure 6.1, focusses on performing a comparative analysis of the floor waviness results obtained using point cloud data collected using TLS and lidar senor mounted UAV. The method of comparison presented in this study uses waviness detection results from TLS point clouds as ground truths. Furthermore, the impact of point cloud

resolution is analyzed to provide recommendations on the number of TLS scans required and the scanning resolution.

6.2 Comparison of TLS-based and UAV-based Point Clouds for Surface Waviness Measurement

6.2.1 Data Collection and Preprocessing

The data was collected from a newly constructed floor of a lecture hall under the Magruder Hall Expansion project in Corvallis, OR. Figure 6.2 shows the region of interest, and its surface area was approximately 140 m^2. The Leica P40 scanner was setup in two locations across the floor. After registering the two scans, the resolution of the output point cloud was approximately 5 mm within a range of 10 m.

The UAV mounted with the lidar sensor was operated at a constant height of approximately 60 m above the surface of the ground, making two passes over the area of interest. It is assumed that the beam divergence is constant throughout the flight. The preprocessing steps for the UAV data involved processing the flight trajectory and computing the point cloud data from the processed trajectory. The final resolution of the output point cloud collected from the UAV system was 5 cm within a range of 60 m.

Figure 6.2 The region of interest is marked in orange.

6.2.2 Data Processing

The framework developed in [137] was used to process the data obtained from TLS and UAV. The obtained point clouds from the TLS and UAV systems were imported into a commercial point cloud processing software to remove scans corresponding to workers working on the floor and various construction debris. A depth map is developed using triangulation-based linear interpolation on a grid with regular intervals of 1 cm. This process generated a map showing z-coordinates at the each query points, where each query point is represented by the intersection of lines on the x-y plane of the grid. CWT, using the Mexican Hat wavelet as the mother wavelet, was applied to the depth map at different scales. For simplifying the analysis, only five scales were chosen for the CWT: 15, 30, 45, 60 and 75. The five scales correspond to the five undulation periods that are focused upon in the WI method: 2, 4, 6, 8 and 10 ft respectively. The correspondence between the WI index values and the CWT scales are shown in Table 1.

Table 6.1 Waviness Index values and corresponding continuous wavelet transform scales [3][4]

Characteristic period (T) [cm]	CWT scale (a)	Waviness Index (k values)
61	15	1
121.9	30	2
182.9	45	3

6.2.3 CWT Results

The surface waviness results obtained for the TLS- and UAV-based point clouds are shown in Figure 2.As shown in the scalogram, peak responses are shown for the CWT coefficient values lie 10% below the maximum value. The location of these peak responses for each of the five scales are used for our analysis. Figure 6.3 shows the peaks detected for the CWT responses at the five scales.

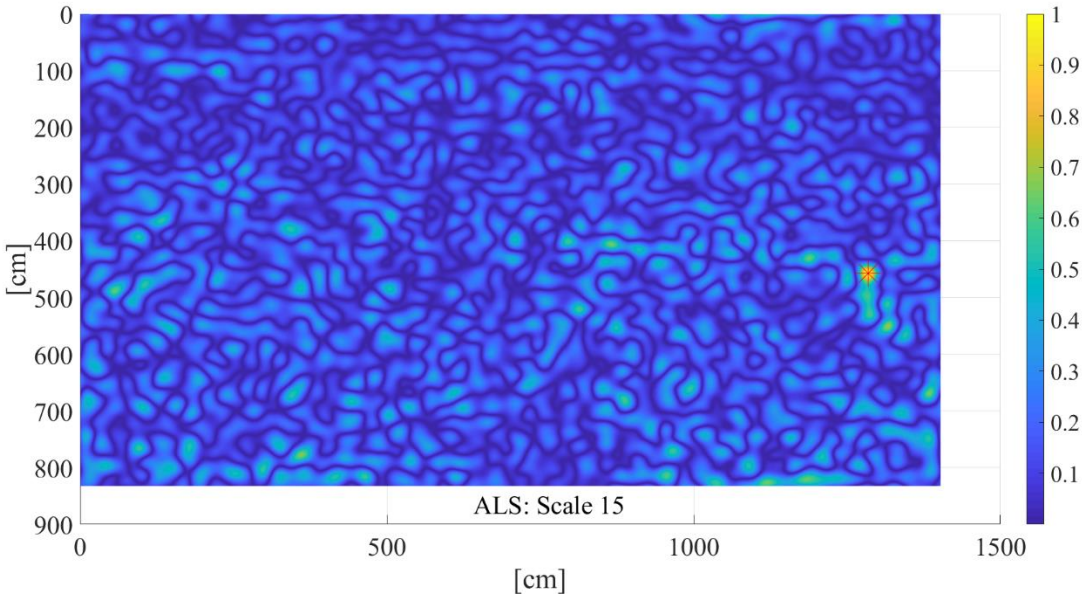

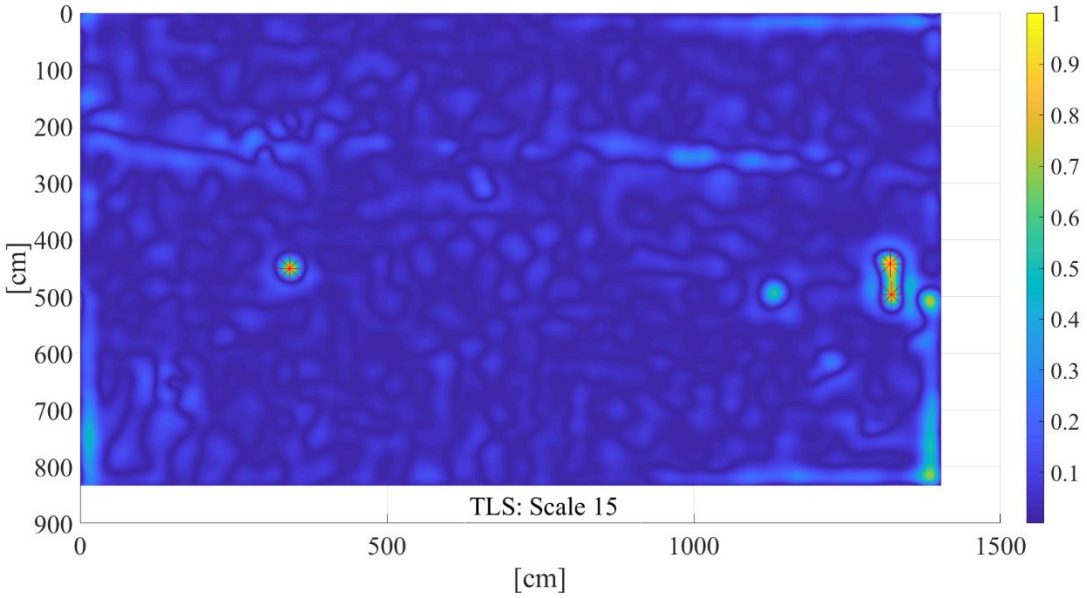
0
100
200
300
400
500
600
700
800
900
[cm]
TLS: Scale 15
0
500
1000
1500
[cm]
1
0.9
0.8
0.7
0.6
0.5
0.4
0.3
0.2
0.1

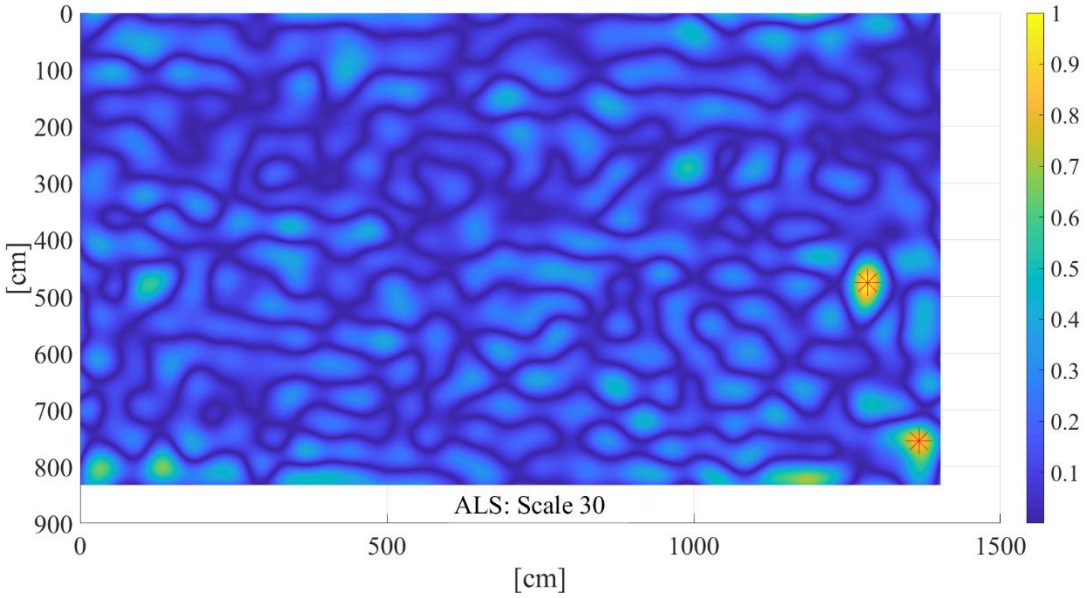
0
100
200
300
400
500
600
700
800
900
[cm]
ALS: Scale 30
0
500
1000
1500
[cm]
1
0.9
0.8
0.7
0.6
0.5
0.4
0.3
0.2
0.1

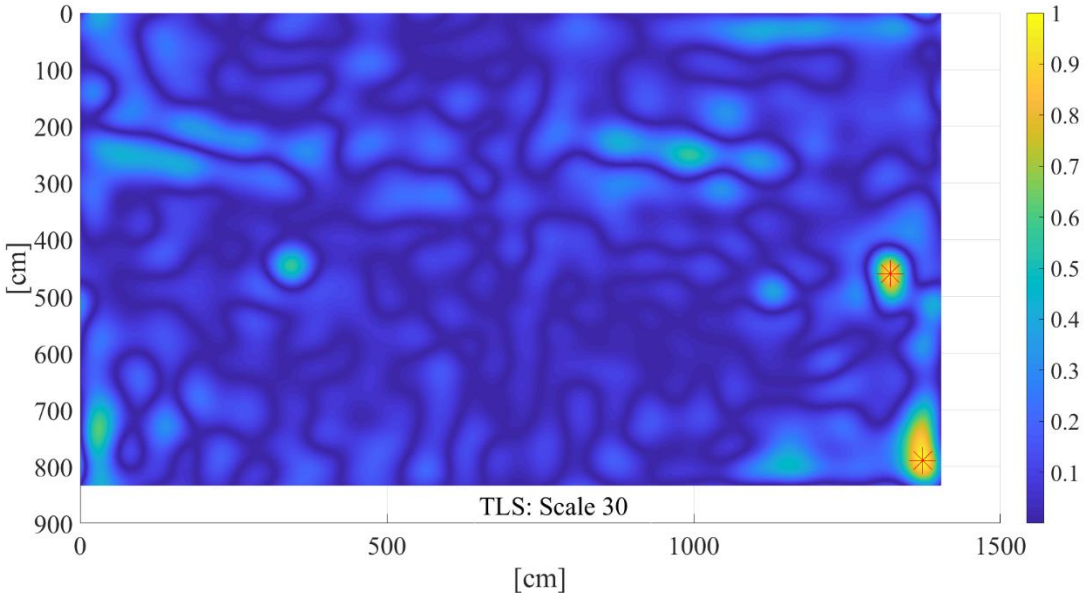
0
100
200
300
400
500
600
700
800
900
[cm]
TLS: Scale 30
0
500
1000
1500
[cm]
1
0.9
0.8
0.7
0.6
0.5
0.4
0.3
0.2
0.1

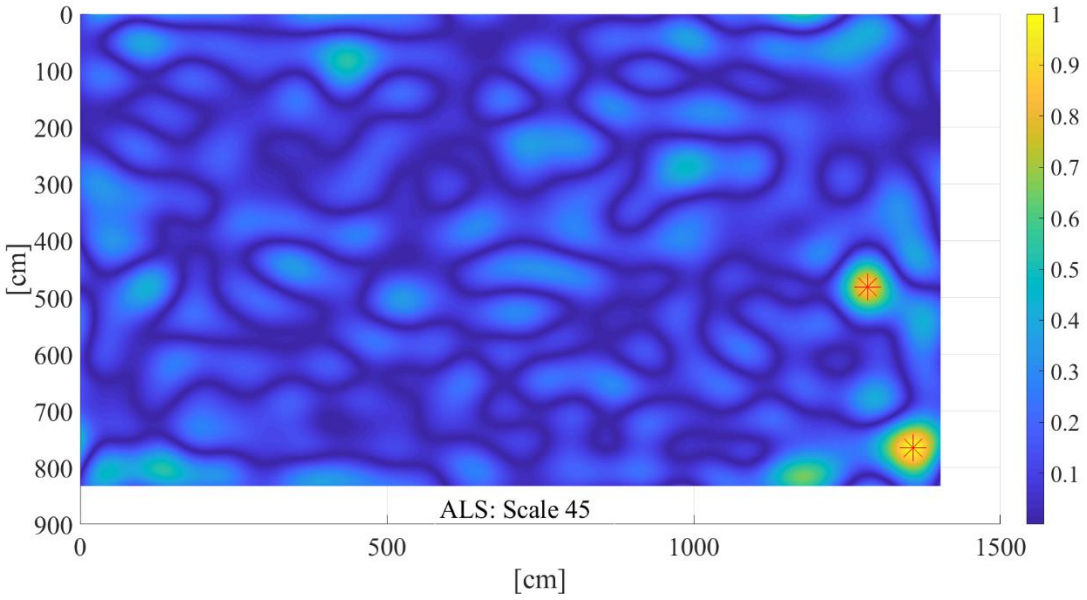
0
100
200
300
400
500
600
700
800
900
[cm]
ALS: Scale 45
0
500
1000
1500
[cm]
1
0.9
0.8
0.7
0.6
0.5
0.4
0.3
0.2
0.1

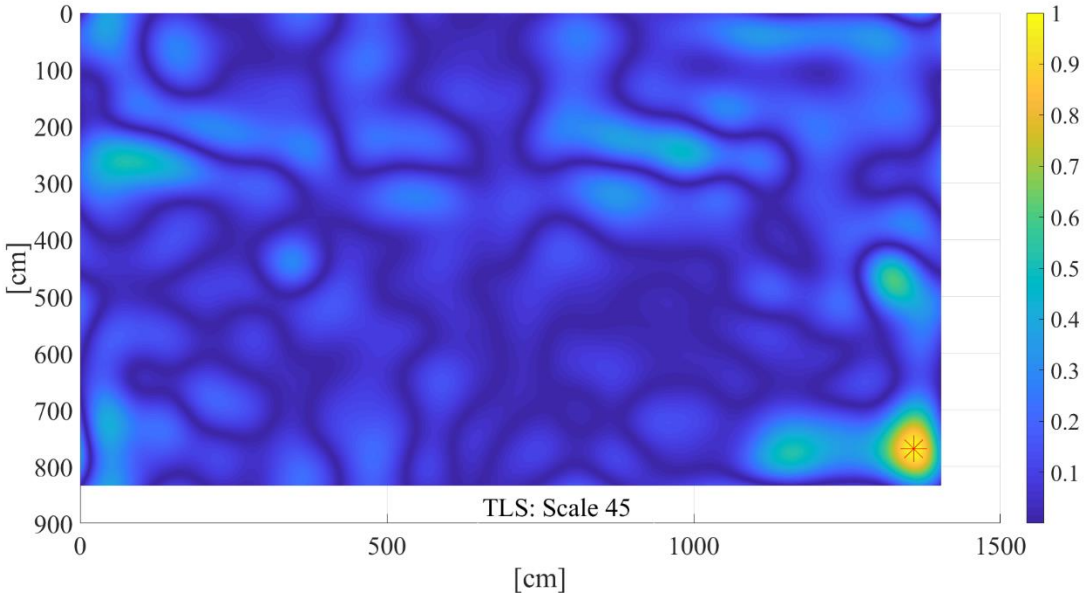
0
100
200
300
400
500
600
700
800
900
[cm]
TLS: Scale 45
0
500
1000
1500
[cm]
1
0.9
0.8
0.7
0.6
0.5
0.4
0.3
0.2
0.1

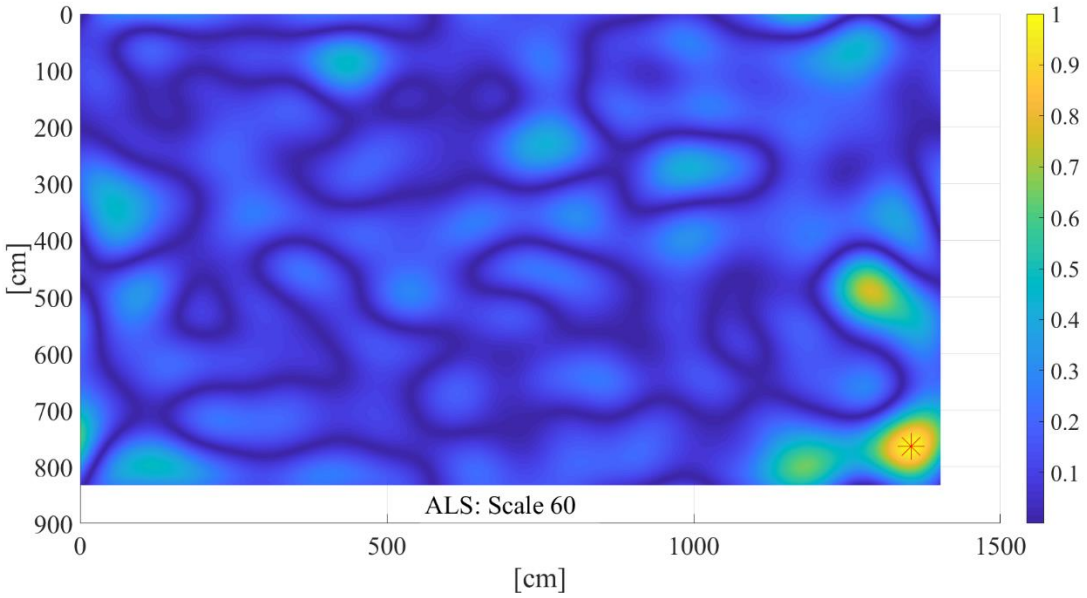
0
100
200
300
400
500
600
700
800
900
[cm]
ALS: Scale 60
0
500
1000
1500
[cm]
1
0.9
0.8
0.7
0.6
0.5
0.4
0.3
0.2
0.1

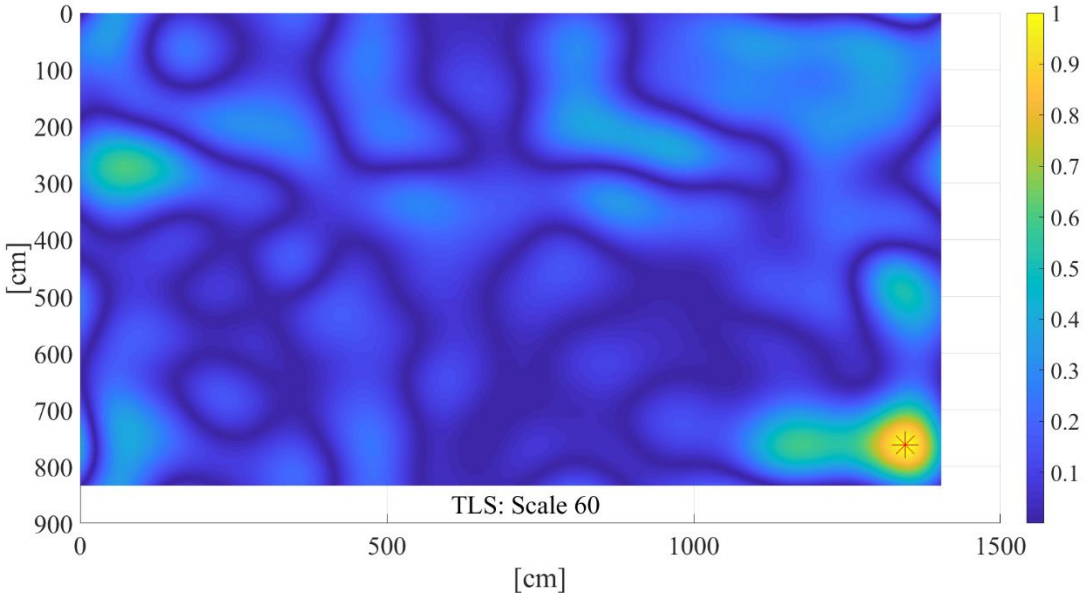
0
100
200
300
400
500
600
700
800
900
[cm]
TLS: Scale 60
0
500
1000
1500
[cm]
1
0.9
0.8
0.7
0.6
0.5
0.4
0.3
0.2
0.1

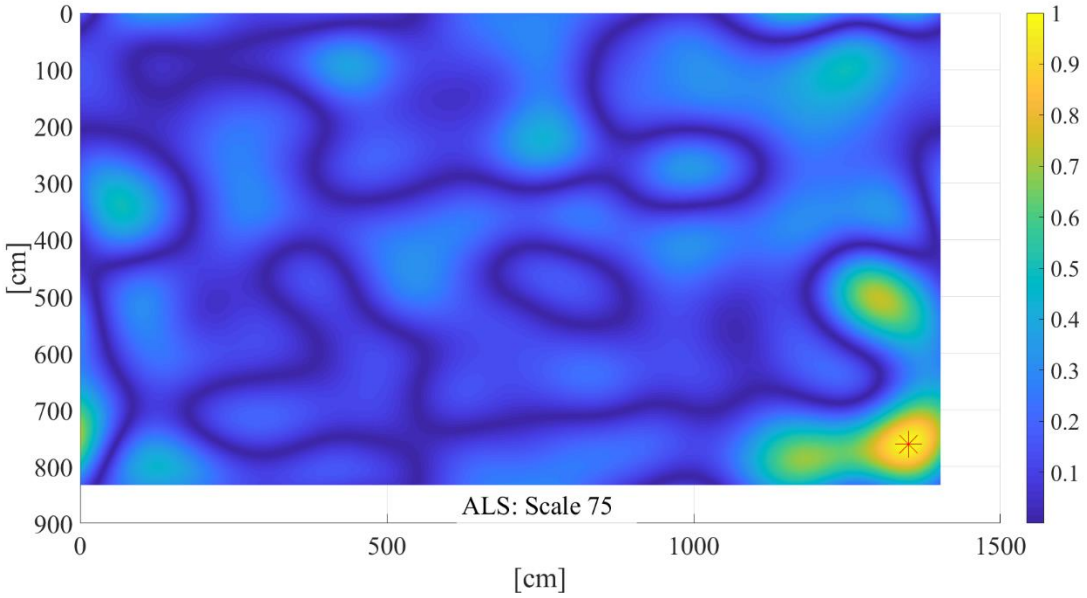
0
100
200
300
400
500
600
700
800
900
[cm]
ALS: Scale 75
0
500
1000
1500
[cm]
1
0.9
0.8
0.7
0.6
0.5
0.4
0.3
0.2
0.1

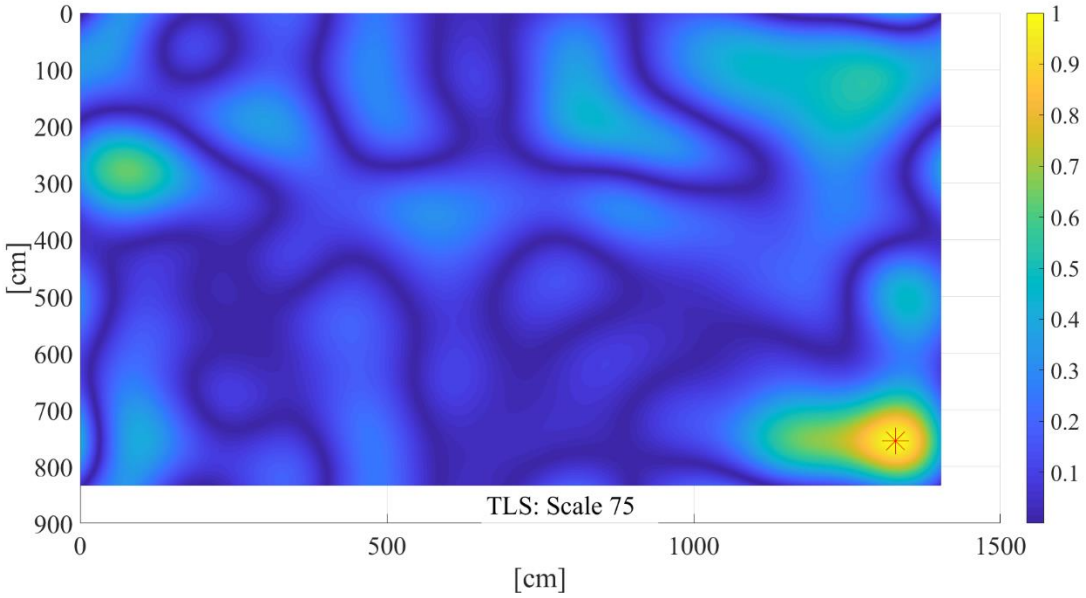

Figure 6.3 The results of the CWT analysis with peak detection

The waviness results obtained from the TLS-based point clouds are used as ground truth for measuring the performance of the UAV-based point clouds for generating the waviness results. Figure 6.3 shows the peak detection results for the UAV-based and TLS-based point clouds.

In the TLS based results, for scale 15, the ground truth shows that there are 3 peaks that correspond to undulations having a characteristic period of 61 cm. Only one of those peaks are detected in the waviness results derived from the UAV point cloud. For scale 30, two peaks that correspond to the characteristic period of 121.9 cm were detected in both the TLS and UAV based results. At scale 45, one peak corresponding to 182.9 cm was obtained in the TLS and two peaks in the TLS based results. Similarly, for scales 60 and 75, 1 peak corresponding to the characteristic period of 304.8 cm was detected in both the TLS and UAV based results.

Table 6.2 Peak detection results for the TLS-based and UAV-based point cloud data

Scales	Number of peaks correctly identified	Number of peaks incorrectly identified or failed to identify	Actual number of peaks (based on 0.01° scanning resolution)
15	**1**	**2**	**3**
30	**2**	**0**	**2**
45	**1**	**1**	**1**
60	**1**	**0**	**1**
75	**1**	**0**	**1**

The surface waviness results for scales 60 and 75 using the TLS and UAV based point clouds are comparable. For scale 45, a false positive was detected near [1283 cm,481 cm]. The same region near the TLS was inspected and no peak was found. The CWT response at that region for the UAV based results was 0.8816, and 0.1674 for the TLS. This discrepancy might be attributed to the difference in the z-values shown in the depth maps of the TLS and UAV point clouds. The TLS based depth map shows the elevation at [1283 cm,481 cm] to be approximately 2.8 cm and the UAV based depth map shows 1.75 cm. Although the TLS and UAV scans were collected almost simultaneously, there were workers actively working on the work surface. This may be due to dynamic changes resulting from moved objects or debris on the surface of the floors. Due to a lower resolution of the UAV point cloud, the points in that region may have been visually classified as part of the floor and not removed. For scale 15, the results are not comparable to each other. A possible reason could be that using TLS-based a high-resolution point cloud accurately detected undulations of a lower characteristic period (61 cm). The lower resolution UAV-based point cloud may have failed to capture the undulations. While generating the depth map, the z-coordinates are smoothed out to a higher degree if less neighboring points are present around the query points. For the true positives obtained in the peak detection results, mean average error is calculated to determine the magnitude with which the position of the detected peaks deviate from the ground truth values.

6.3 TLS Point Cloud Resolution Analysis

The framework developed in [137] was used to process the data obtained using the TLS system. The data used analysis in this section was collected from the Magruder Hall Expansion project in Corvallis, OR and the Vista Logistics Park project in Gresham, OR. The slab from the Magruder Hall expansion project represents the floor of a new classroom and is approximately 140 m^2. The in-situ concrete slab from the Vista Logistics project represents the floor of an industrial space which is approximately 500 m^2.

6.3.1 Magruder Hall Expansion Project

6.3.1.1 Data Collection

A total of two scans were collected from the Magruder Hall Expansion project. Figure 6.4 shows the 9.4 m x 15.1 m slab with the two scan positions. As shown in the picture, several gaps exist in the point cloud, which resulted from cleaning the point cloud. During the creation of depth map, these regions will acquire z-values as a result of the interpolation of z-values of the neighboring points. Table 6.3 provides details about the collected scans.

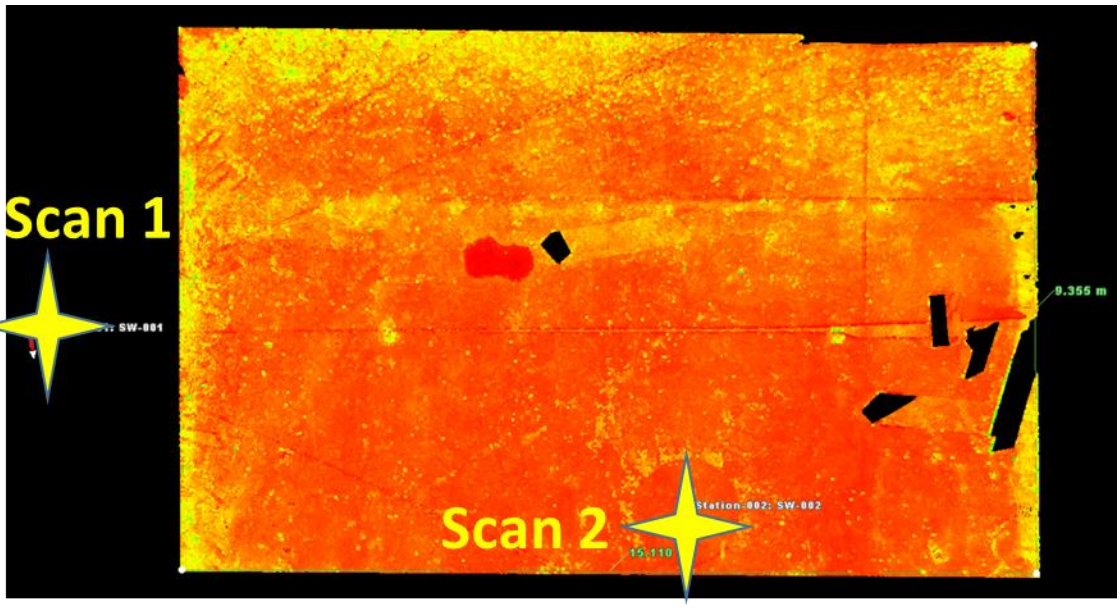

Figure 6.4 Point cloud data for the floor of the Magruder Hall expansion project showing the two scan positions.

The scans were collected using the Leica P40 scanning system with the resolution setting of 2mm @10 m. Using simple trigonometry, this resolution setting can be converted into degrees as follows:

$$d = 2^{*} \tan^{-1}\left(\frac{0.5 * d}{D * 1000}\right) * \left(\frac{180^{\circ}}{\pi}\right) \qquad (6.1)$$

where, D is the distance between the scanner and an object, and d is the point spacing. Using this relation, it was found that 2mm @10 m corresponds to 0.01°. Note that Equation 6.1 is assuming that laser pulses come in contact with the surface at perfect incidence. In practice, this angle of incidence varies across the floor surface, contrary to the assumption made in Equation 6.1.

Table 6.3 Information on the two scans for the Magruder Hall expansion project

	Number of Points	**Original Scanning Resolution**	**Distance from Scan Position to Center of Slab [m]**	**Nearest point from Scan Position to Edge of Slab [m]**	**Furthest point from Scan Position to Edge of Slab [m]**
Point Cloud 1 (SW1)	12,648,589	0.01°	10.38	3.01	18.5
Point Cloud 2 (SW2)	73,312,914	0.01°	3.86	1.75	12.46

6.3.1.2 Data Processing

The point cloud is converted into a depth map with 1 cm intervals in both horizontal and vertical directions and the z-coordinates at each grid point is calculated based on the procedure described in section 5.2.1. The two point clouds, each having 0.01° scanning resolution are used. The resulting depth map is shown in Figure 6.5. The color ma limits were set to [-1,1] cm because the height of the slab varies mostly from -1 cm to 1 cm. These limits enable the variations in elevation along the slab surface to be distinguished easily.

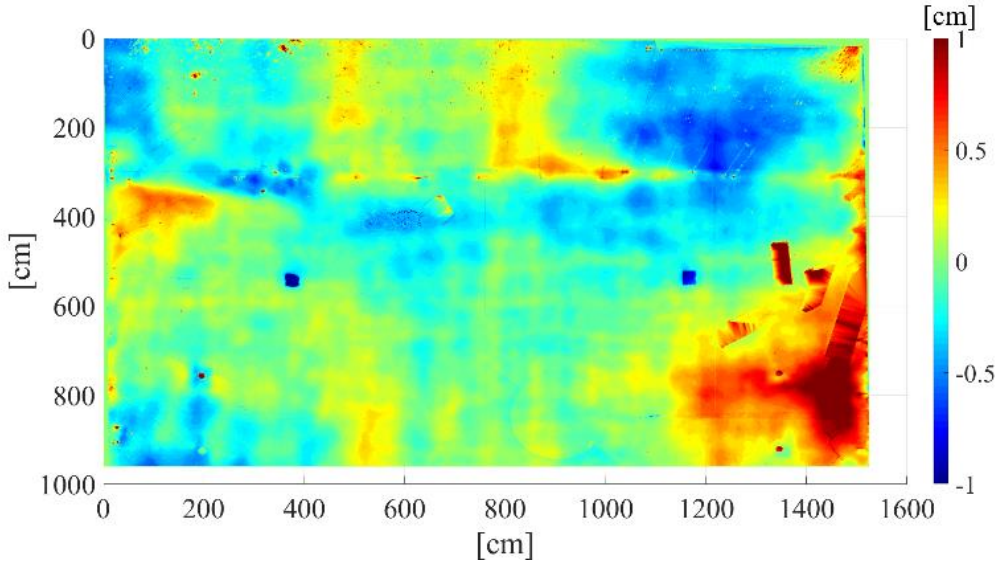

Figure 6.5 Depth map derived from the Magruder Hall TLS data, with color map limits set to [−1, 1] cm; scanning resolution of 0.01°.

6.3.1.3 CWT Results

Figure 6.6 shows the results obtained for the scales 15, 30, 45, 60 and 75 of the mother wavelet for the Magruder Hall TLS data having two scans, each at a resolution of 0.01°. The point cloud consisting of the two scans each at scanning resolution of 0.01° is considered as the ground truth for comparing and analyzing CWT results. This is justified because the correspondence between the WI method and the 2D CWT method in [137] was established based on a point cloud having a consisting of four scans at scanning resolution of 0.01°. The regions where the input “signal”, the slab surface, strongly correlates with the mother wavelet applied at the scales above are highlighted in yellow in Figure 6.6.

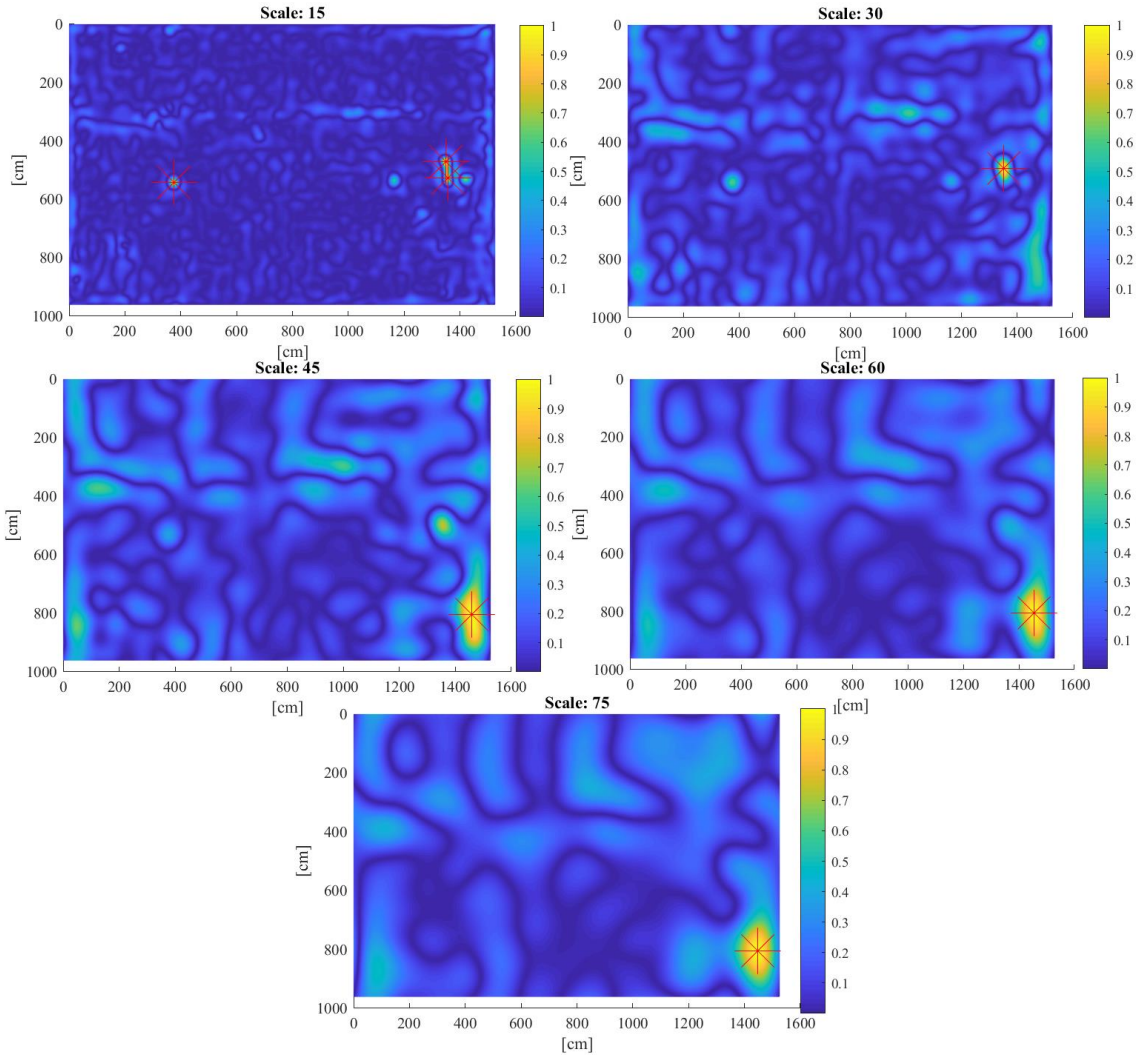

Figure 6.6 The coefficients obtained from the wavelet transformation corresponding to scales 15 (a), 30 (b), 45 (c), 60 (d) and 75 (e) are plotted on the map for the Magruder Hall slab. The areas in the slabs where undulations corresponding to these scales are present are shown. The peaks are marked in red. The two scans are at scanning resolution 0.01° each.

Each of the collected scans for the Magruder Hall extension project are analyzed for five different scan resolutions of 0.02°, 0.04°, 0.06°, 0.08° and 0.1°. The estimated scanning times for the scan resolutions of 0.01°, 0.02°, 0.04°, 0.06°, 0.08° and 0.1° are 13 min, 4 min, 2 min, 1 min and 0.5 min and 0.3 min respectively (not including the times for collecting the images) assuming normal speed mode. They represent times for collecting scans only (without images). When scans are collected from multiple scanning positions,

it can be assumed that the time for dismantling and setting up the TLS for each scan position requires 5-8 minutes. Three different cases have been analyzed for the Magruder Hall slab. The first case analyses, a discussed in section 6.3.1.3.1, the CWT result at the five angular resolutions for Scan 1. The second and third cases defined in sections 6.3.1.3.2 and 6.3.1.3.3 represent similar analyses for Scan 2, and Scan 1 and Scan 2 combined, respectively. Scan 1 and Scan 2 were analyzed separately in order to study the effect of the distance between scanner location and the geometric center of the slab, on the CWT results. As shown in Table 6.3, the scanner position for Scan 1 is 10.3 m away from the geometric center of the slab, whereas for Scan 2, this value is 3.68 m. This discrepancy between the two point clouds fundamentally affects the density of the point cloud in the region of interest. Thus, further analyses is presented in section 6.3.1.3.1.

6.3.1.3.1 Case 1: Number of Scans =1 (Scan 1)

The coefficients obtained from the wavelet transformation corresponding to scales 15 (a), 30 (b), 45 (c), 60 (d) and 75 (e) are plotted on the map for the Magruder Hall slab. The areas in the slabs where undulations corresponding to these scales are present are shown in Appendix CWT results from Chapter 6 . The peaks are marked in red. Scan 1 is at scanning resolution of 0.02°.

The surface waviness results for scales 60 and 75 using the 0.01° and 0.02° scanning resolution point clouds are comparable, as shown in Figure 6.6 The coefficients obtained from the wavelet transformation corresponding to scales 15 (a), 30 (b), 45 (c), 60 (d) and 75 (e) are plotted on the map for the Magruder Hall slab. The areas in the slabs where undulations corresponding to these scales are present are shown. The peaks are marked in red. The two scans are at scanning resolution 0.01° each. For scale 15, a false positive was detected near [600 cm, 390 cm]. The same region in the point cloud having scanning resolution of 0.01° was inspected and no peak was found. This discrepancy might be attributed to the difference in the z-values shown in the depth maps of the two point clouds. The depth map of point cloud having scanning resolution of 0.01° shows the elevation at

[600 cm, 390 cm] to be approximately 0.7 cm and the depth map of point cloud having scanning resolution of 0.01° shows more than 1 cm. This discrepancy is due to a gap in the point cloud resulting from filtering out noise. However, the same argument does not justify the presence of two false negatives that were detected for scale 15, as shown in Figure 6.6 The coefficients obtained from the wavelet transformation corresponding to scales 15 (a), 30 (b), 45 (c), 60 (d) and 75 (e) are plotted on the map for the Magruder Hall slab. The areas in the slabs where undulations corresponding to these scales are present are shown. The peaks are marked in red. The two scans are at scanning resolution 0.01° each. Similarly, the results for scan resolutions 0.04°, 0.06°, 0.08° and 0.1° fail to accurately and precisely detect the location of defects for various scales, as shown in Appendix A.2: Magruder Hall Expansion Project:. The results for all scales are summarized in Appendix A.2: Magruder Hall Expansion Project: for the five angular resolutions.

6.3.1.3.2 Case 2: Number of Scans =1 (Scan 2)

For Scan 2, results of the scanning resolution angles of 0.02°, 0.04°, 0.06° and 0.08°. showed that they match with our ground truth results. For scanning resolution of 0.1°, a discrepancy is observed for scale 30, where one peak is misclassified. The resolution of the point cloud has affected the CWT result at the scanning resolution of 0.1°. Appendix A.2: Magruder Hall Expansion Project: summarizes the results of the CWT analysis for the five scanning resolutions.

6.3.1.3.3 Case 3: Number of Scans =2 (Scan 1 + Scan 2)

For this case, scan 1 and scan 2, each having the same scanning resolution, are combined and analyzed. For Scan 1 and 2, results of the scanning resolution angles of 0.02°, 0.04°, 0.06°, 0.08° and 0.1° showed that they match with our ground truth results Appendix A.2: Magruder Hall Expansion Project: summarizes the results of the CWT analysis for the five scanning resolutions.

6.3.1.3.4 Discussion

The results from section 6.3.1.3.1, 6.3.1.3.2 and 6.3.1.3.3 show that the CWT analysis five resolutions for the combined scans (Scan 1 and Scan 2) give results that match the ground truth in the Magruder Project. There are significant discrepancies between the results obtained using only Scan 1 and only Scan 2 for the five scanning resolutions. This can be attributed to the fact that Scan 2 has 6 times as many points as Scan 1. This is due to the different scanning positions chosen for the two scans. The results are summarized in Table 6.4.

Table 6.4 Summary of results for the Magruder Hall expansion project. The cells that are in red color denote that the test case results did not match the ground truth results, whereas the cells that are in yellow color denote that the test case results did match the ground truth results.

	0.02°	**0.04°**	**0.06°**	**0.08°**	**0.10°**
Scan 1	×	×	×	×	×
Scan 2	✓	✓	✓	✓	×
Scan 1 + Scan 2	✓	✓	✓	✓	✓

Using only one scan (in our case Scan 2) ensured that the CWT results matched the ground truth results for scanning resolutions ranging from 0.02° through 0.08°. Thus, it can be concluded that collecting one scan can give accurate surface waviness results for scanning position as far as a 12.46 m from the furthest point in slab (Table 6.3). Note that the scanner is setup within the boundaries of the slab surface.

If scans are collected from two scanning locations, scanning resolutions ranging from 0.02° through 0.1° can be used. Each of the scanning locations for the two scans may be as

far as 12.46 m from the furthest point in the slab. Table 6.3 shows that this distance could have been 18.5 m but a conservative distance was chosen to generate accurate results. Note that the scanner is setup within the boundaries of the slab surface.

6.3.2 Vista Logistics Park Project

6.3.2.1 Data Collection

Four different scanning positions were chosen for collecting data from the Vista Logistics Park Project. The concrete slab from this project is shown in Figure 6.7 and has dimensions of 25.5 m x 19.5 m. Details on the collected scans are shown in Table 6.5.

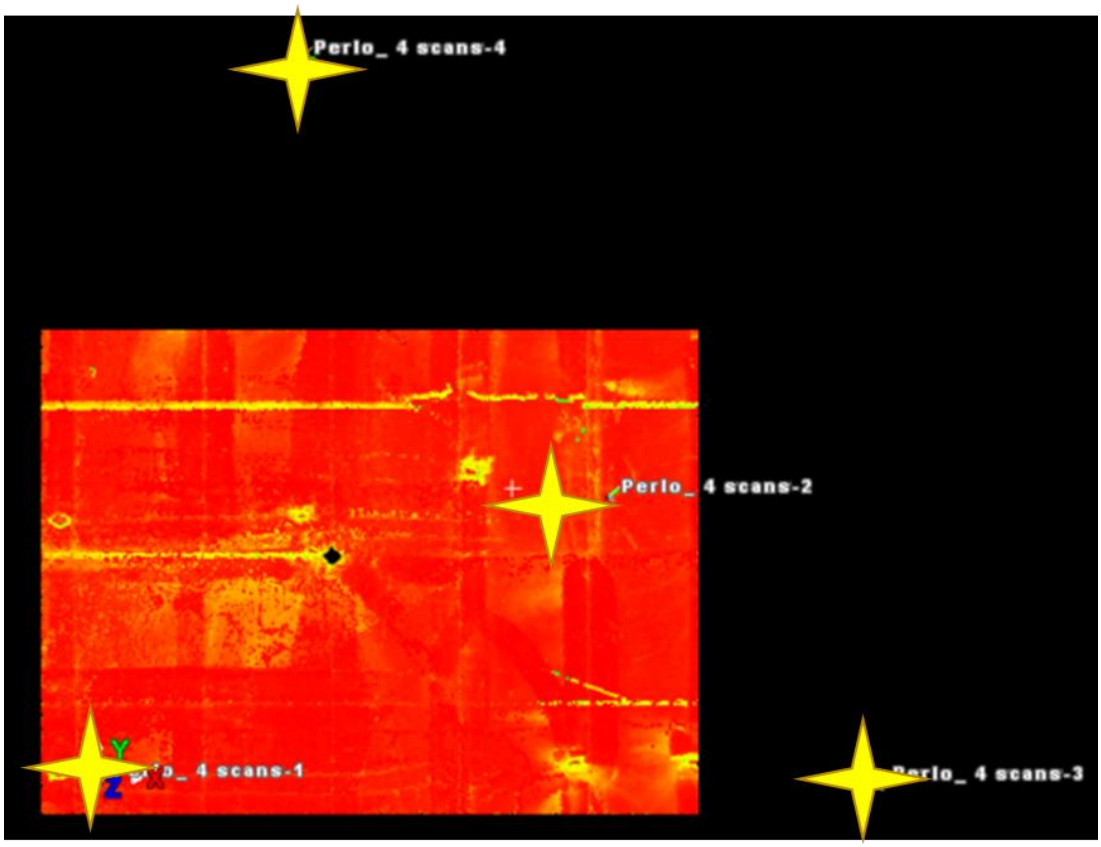

Figure 6.7 Point cloud data for the concrete slab of the Vista Logistics Park project showing four scan positions.

Table 6.5 Details on the four scans collected from the concrete slab of the Vista Logistics Park project showing four scan positions

	Number of Points	**Original Scanning Resolution**	**Distance from Scan Position to Center of Slab [m]**	**Nearest point from Scan Position to Edge of Slab [m]**	**Furthest point from Scan Position to Edge of Slab [m]**
Point Cloud 1 (SW1)	68,710,907	0.01°	11.89	2.21	25.85
Point Cloud 2 (SW2)	68,579,657	0.01°	8.40	3.4	22.69
Point Cloud 3 (SW3)	27,566,521	0.01°	19.26	6.46	33.28
Point Cloud 4 (SW4)	22,260,828	0.01°	17.53	2.32	36.73

6.3.2.2 Data Processing

A depth map with 1 cm intervals in both horizontal and vertical directions is created using the four point clouds, each having a scanning resolution of 0.01°. The z-coordinates at each grid point is calculated based on the procedure described in section 5.2.1. The depth map is shown in Figure 6.8. The color limits were set to [-1,1] cm because the height of the slab varies predominantly between -1 cm to 1 cm, and variations in elevation along the slab surface can be distinguished easily.

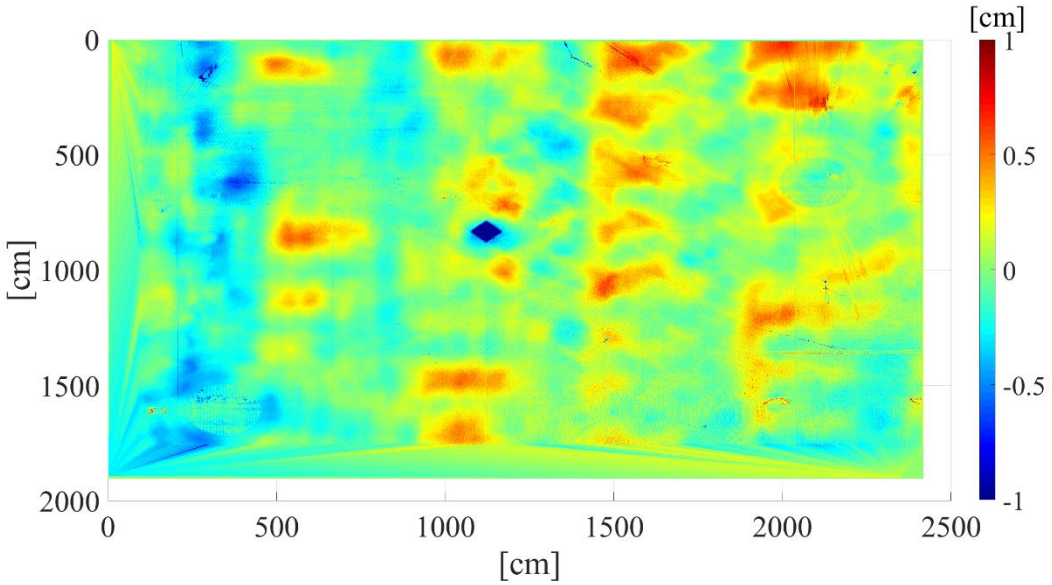

Figure 6.8 Depth map derived from the Vista Logistics Park project TLS data, with color map limits set to [−1, 1] cm; scanning resolution of 0.01°.

6.3.2.3 CWT Results

Figure 6.9 shows the results obtained for the scales 15, 30, 45, 60 and 75 of the mother wavelet for the Magruder Hall TLS data having two scans, each at a resolution of 0.01°. The point cloud consisting of the two scans each of scanning resolution of 0.01° is considered as the ground truth for comparing and analyzing CWT results. The regions where the input “signal”, the slab surface, strongly correlates with the mother wavelet applied at the scales above are highlighted in yellow in Figure 6.9.

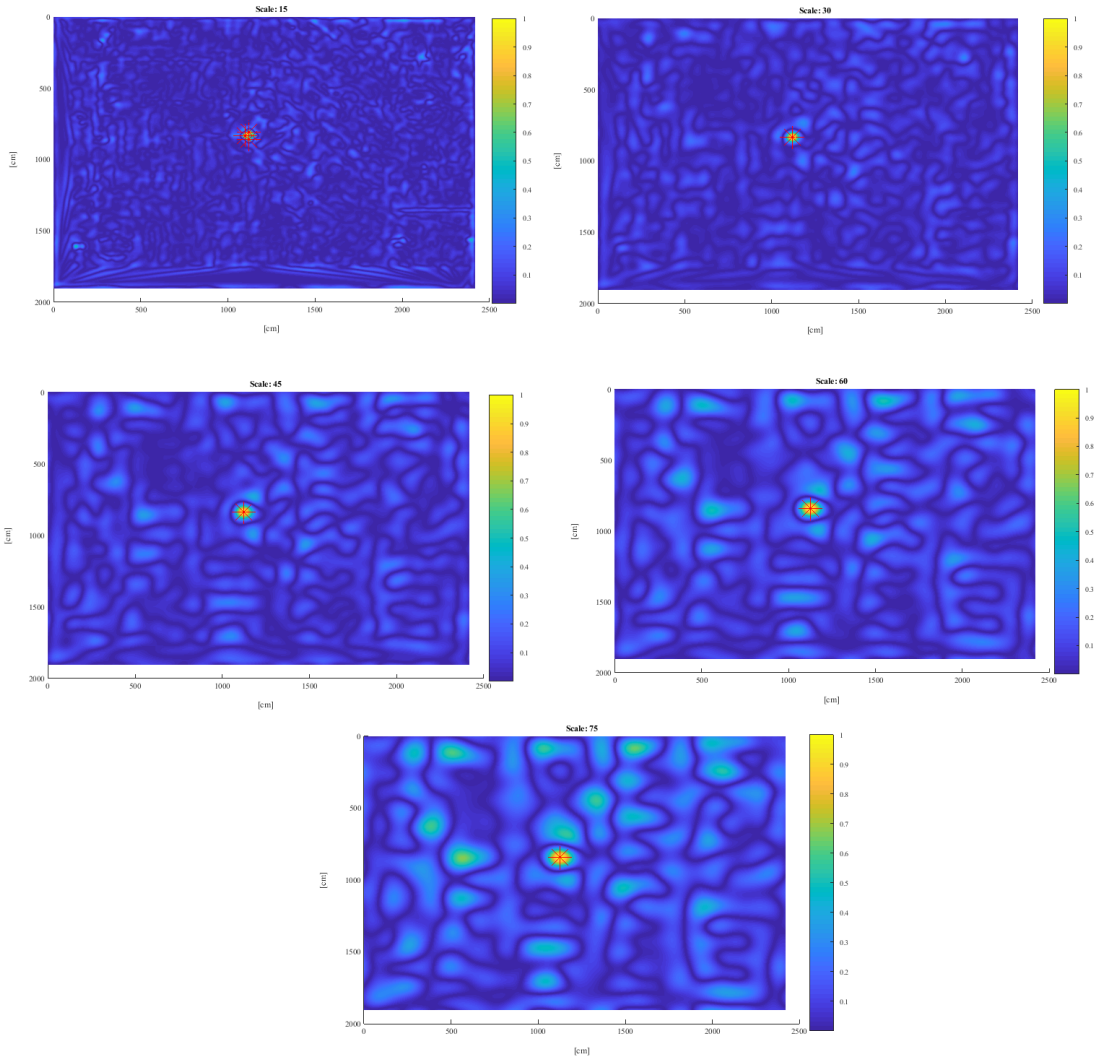

Figure 6.9 The coefficients obtained from the wavelet transformation corresponding to scales 15 (a), 30 (b), 45 (c), 60 (d) and 75 (e) are plotted on the map for the Vista Logistics Park project slab. The areas in the slabs where undulations corresponding to these scales are present are shown. The peaks are marked in red. The four scans are at scanning resolution 0.01° each.

The four scans collected for the Vista Logistics Park project extension project are analyzed for five different scan resolutions of 0.02°, 0.04°, 0.06°, 0.08° and 0.1°. Four different cases have been analyzed for the Vista Logistics Park project slab. The first case analyses the CWT result at the five angular resolutions for Scan 2. Scan 2 was chosen because the scan

position was relatively closer to the geometric center of the slab. The second case represents similar analyses for Scan 1 and Scan 2 combined. The third and fourth cases analyze Scans 1, 2 and 4 combined, and Scans 1, 2, 3 and 4 combined, respectively.

6.3.2.3.1 Case 1: Number of Scans =1 (Scan 2)

The coefficients obtained from the wavelet transformation corresponding to scales 15 (a), 30 (b), 45 (c), 60 (d) and 75 (e) are plotted on the map for Scan 2 of the Vista Logistics Park project slab. The areas in the slabs where undulations corresponding to these scales are present are shown. The peaks are marked in red. Scan 2 is at scanning resolution of 0.02°. The CWT analyses of all five scanning resolutions showed that the surface waviness results for scale 15 were significantly different from the ground truth results. The surface waviness results for scales 30, 45, 60 and 75 using the ground truth and 0.02° scanning resolution point cloud (Scan 2) are comparable, as shown in Figure 6.6 and Figure 6.10. The results are summarized in Table 6.6.

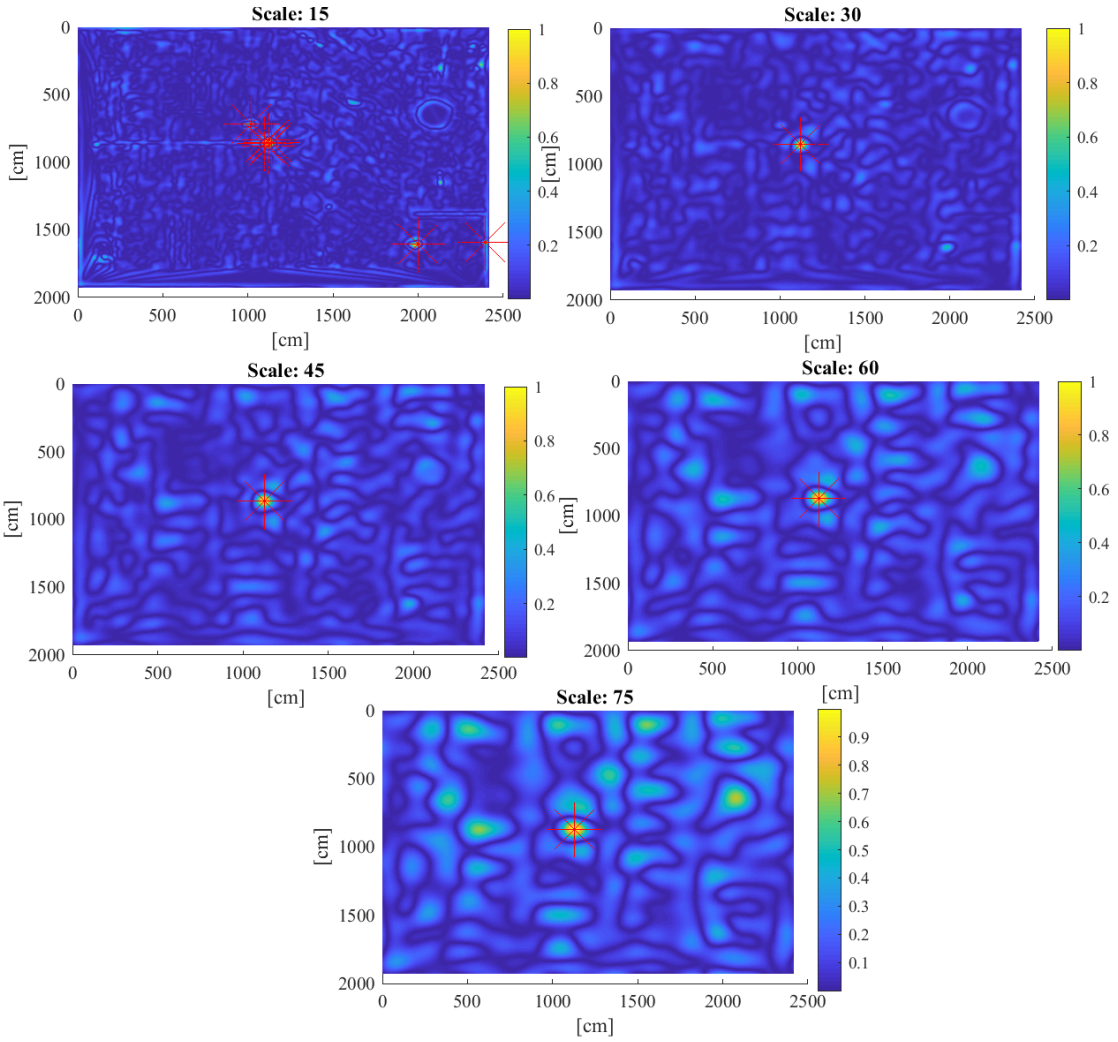

Figure 6.10 The coefficients obtained from the wavelet transformation corresponding to scales 15 (a), 30 (b), 45 (c), 60 (d) and 75 (e) are plotted on the map for Scan 2 of the Vista Logistics Park project slab. The areas in the slabs where undulations corresponding to these scales are present are shown. The peaks are marked in red. The scan is at scanning resolution 0.02°.

Table 6.6 Peak detection results for Scan 2 at scanning resolution 0.02°

Scales	**Number of peaks correctly identified**	**Number of peaks incorrectly identified or failed to identify**	**Actual number of peaks (based on 0.01° scanning resolution)**
15	**3**	**3**	**3**
30	**1**	**0**	**1**
45	**1**	**0**	**1**
60	**1**	**0**	**1**
75	**1**	**0**	**1**

For scale 15, one false positive was detected near [1050 cm, 750 cm]. This discrepancy might be attributed to the difference in the z-values shown in the depth maps of the two point clouds. The depth map of point cloud having scanning resolution of 0.01° shows the elevation at [1050 cm, 750 cm] to be approximately 0.75 cm and the depth map of point cloud (Scan 2) having scanning resolution of 0.02° shows 0.1 cm. Two other false positives were detected near [2000 m, 1600 m] and [2400 m, 1600m]. The same region in the point cloud having scanning resolution of 0.01° was inspected and no peak was found. This discrepancy is due to a gap in the point cloud resulting from filtering out noise. Similarly, the results for scan resolutions 0.04°, 0.06°, 0.08° and 0.1° fail to accurately and precisely detect the location of defects for scale 15, as shown in Appendix A.3: Vista Logistics park project:. The results for all other scales are summarized in Appendix A.3: Vista Logistics park project: for the five angular resolutions.

6.3.2.3.2 Case 2: Number of Scans =2 (Scan 1 + Scan 2)

Scan 1 and Scan 2 are both at scanning resolution of 0.02°. For Scan 1 and Scan 2 combined, results of the scanning resolution angles of 0.02°, 0.04°, 0.06° and 0.08° showed that they match with our ground truth results for scales 30 45, 60 and 75. For scanning resolution of 0.1°, a discrepancy is observed for scales 15, 30 and 75. The resolution of the point cloud has affected the CWT result at the scanning resolution of 0.1°. Appendix A.3: Vista Logistics park project: summarizes the results of the CWT analysis for the five scanning resolutions.

6.3.2.3.3 Case 3: Number of Scans =2 (Scan 1 + Scan 2+ Scan 4)

Scan 1, Scan 2 and Scan 4 are all at scanning resolution of 0.02°. For Scan 1, Scan 2 and Scan 4 combined, results of the scanning resolution angles of 0.02°, 0.04°, 0.06° and 0.08° showed that they match with our ground truth results for scales 30 45, 60 and 75. For scanning resolution of 0.1°, a discrepancy is observed for scales 15 and 75. The resolution of the point cloud has affected the CWT result at the scanning resolution of 0.1°. Appendix A.3: Vista Logistics park project: summarizes the results of the CWT analysis for the five scanning resolutions.

6.3.2.3.4 Case 4: Number of Scans =2 (Scan 1 + Scan 2 + Scan 3 + Scan 4)

Scan 1, Scan 2, Scan 3 and Scan 4, in their original form, are at scanning resolution of 0.01°. For Scan 1, Scan 2, Scan 3 and Scan 4 combined, results of the scanning resolution angles of 0.02° show that the results match the ground truth results for all five scales. The results from 0.04°, 0.06° and 0.08° showed that they match with our ground truth results for scales 30, 45 and 60. For scanning resolution of 0.1°, a discrepancy is observed for scales 15, 30 and 75. The resolution of the point cloud has affected the CWT result at the scanning resolution of 0.1°. Appendix A.3: Vista Logistics park project: summarizes the results of the CWT analysis for the five scanning resolutions.

6.3.2.3.5 Discussion

The results from section 6.3.2.3.1, 6.3.2.3.2, 6.3.2.3.3, 6.3.2.3.4 and 6.3.1.3.3 show that Scan 1, Scan 2, Scan 3 and Scan 4, combined, at 0.02° scanning resolution each, give results that match the ground truth in the Vista Logistics Park project. There are significant discrepancies between the results obtained using only Scan 1 and Scan 1 and Scan 2, combined, for the five scanning resolutions. Similarly, for other scanning resolutions (0.04°, 0.06° and 0.08°) in Case 4, the results were identical to the ground truth results for

scales 30, 45, 60 and 75. However, the results were different for scale 15 and thus, these scanning resolutions cannot be recommended. The results are summarized in Table 6.7.

Table 6.7 Summary of results for Vista Logistics Park Project. The cells that are in red color denote that the test case results did not match the ground truth results, whereas the cells that are in yellow color denote that the test case results did match the ground truth results.

	0.02°	**0.04°**	**0.06°**	**0.08°**	**0.10°**
Scan 1	×	×	×	×	×
Scan 1 + Scan 2	×	×	×	×	×
Scan 1 + Scan 2 + Scan 4	×	×	×	×	×
Scan 1 + Scan 2 + Scan 3 + Scan 4	✓	✓	✓	✓	×

Using four scans (in our case Scan 1, Scan 2, Scan 3 and Scan 4) ensured that the CWT results matched the ground truth results for scanning resolutions ranging from 0.02° through 0.08°. Thus, it can be concluded that collecting four scans can give accurate surface waviness results. Scanning resolutions ranging from 0.02° through 0.08° can be used. Each of the scanning locations for the four scans may be as far as 22 m from the furthest point in the slab. Note that the scanner is setup within the boundaries of the slab surface. Table 6.3 shows that this distance could have been 25 m, 33 m and 36 m but a conservative distance was chosen to generate accurate results.

7 Limitations and Conclusions

This chapter discusses and summarizes the findings in the Chapters 4, 5 and 6. In addition, it analyses whether the research objectives defined in Chapter 3 have been achieved. The conclusions and limitations of the work presented in this dissertation are also discussed.

7.1 Limitations and Future Work

A progress tracking framework for transportation projects, bridge construction projects in particular, was developed and demonstrated in this dissertation. The framework combines information from 3D design models and construction schedule and lidar data to report project progress information. Using mobile lidar for as-built data collection provides significant benefits over manual methods for progress tracking by facilitating faster as-built data collection and accurately capturing 3D geometric information from construction sites. The developed framework was evaluated using data collected from the Truax Creek bridge project, a small bridge construction project located in Albany, OR. The results of the case study demonstrated that the developed framework enables tracking the completion of individual bridge elements accurately and efficiently. The process of obtaining progress results using the framework is mostly automated. The steps that require manual work include removing irrelevant sections in the preprocessed point clouds that overlap with bridge elements. The object detection relies upon the geometric alignment between the as-built point cloud and virtual point cloud. Hence, overlap between as-built data and irrelevant regions, such as earthwork material may lead to misclassification. Furthermore, the manual processing time for each epoch is approximately 1 hour and 15 minutes for the case study. This time could be further reduced by continued development and refinement of algorithms to complete these manual processing tasks, which were beyond the scope of this study.

Future work should focus on implementing this framework on multiple larger bridge construction projects that contain elements with complex geometrical shapes. Although the

bridge used in this study was of a small scale, the framework is scalable for application to larger bridges. Furthermore, only the x, y, and z coordinates of the collected scan are utilized by the proposed framework. Integration of RGB (Red-Green-Blue) and intensity values into the framework may enable material classification. Integration of RGB values can contribute toward accurate segmentation and object recognition results by correctly classifying points. Furthermore, using a high accuracy scanning system could enable road design layer classification. In this study, only two surfaces, paved and unpaved, were analyzed using PSD to help track progress tracking in horizontal construction projects. Higher accuracy data can be gathered from different road layers (surfaces) during construction. The surface characteristics or roughness of different road design layers can then be effectively analyzed to generate a metric which enables distinguishing one layer from another.

TLS technology has a promising future in the construction industry owing to its ability to rapidly and accurately capture and record as-built conditions. Research efforts are being concentrated to identify specific areas, which could particularly benefit from the application of TLS. Dimensional QC is one such area. The analysis performed using the 2D CWT for QC provides great flexibility for examining the surface undulations with a wide range of characteristic periods. The localization property of 2D CWT highlights regions on the surface and helps in compliance assessment and corrective work planning. The proposed approach in this paper demonstrates how TLS data of a concrete surface can be used to characterize waviness by implementing 2D CWT, using Mexican Hat Wavelet as the mother wavelet. The comparative analysis of the various methods of measuring waviness in concrete slabs reveals that the 2D CWT method provides results that strongly correlate with those of the WI method (the current state of the art), but has numerous advantages over it and other existing methods.

Future research efforts can be directed toward improving the practicality of implementing laser scanning for measuring floor surface waviness. The method proposed in this paper can be used in conjunction with augmented reality devices to enable the visualization of

undulations corresponding to various characteristic periods on site. The proposed method can be further improved by developing algorithms for automatically removing noise and generating scan plans to estimate optimal scanning positions. For this study, manual effort was required for preparing scan plans, setting up the scanner and collecting the point cloud data. Automated registration of laser scans can be further explored. In addition, the analysis presented in Chapter 6 can be extended to larger slab surface areas. Furthermore, the impact of various scanning positions can be explored in detail. The findings can be summarized to develop a TLS scan planning tool that provides guidelines on optimal locations for scanner setups and the optimal scanning resolutions.

7.2 Conclusions: Addressing Research Questions and Objectives

The overall research questions developed for this dissertation were:

1. What are the existing inefficient practices for as-built data collection in the fields of dimensional quality assessment, quality inspection and progress tracking in the construction?
2. How can technology-supplemented as-built data collection improve dimensional quality assessment, quality inspection and progress tracking processes?

The comprehensive literature review performed prior to the beginning of each chapter provided an understanding about the existing practices for as-built documentation in the fields of dimensional quality control quality inspection and progress tracking. The disadvantages of the traditional methods that are prevalent in the industry today were identified. In order to overcome drawbacks related to manual error-prone measurements, challenges related to repeatability of results, labor-intensive inspection procedures and the traditional pen-and-paper method of recording as-built information from on-going construction sites, technology supplemented frameworks are developed and tested. To further narrow the scope of the research, this dissertation focused on the existing problems related to measuring surface waviness in concrete slabs and the progress tracking of bridge construction projects. Section 7.2 provides details about the developed frameworks and describe how technology supplemented frameworks can be used to improve existing

practices in the fields of progress tracking and quality assessment. Although the developed frameworks are not fully automated and still require some degree of human interference, the proposed frameworks can be used in conjunction with existing practices to make these practices more efficient.

The first study in this dissertation, Chapter 4, discusses a technology-supplemented progress monitoring approach. The main research question for the study was 'How can we report the progress of horizontal construction projects in terms of percentage of completion?'

To answer this question, a framework was designed and tested on a real-life bridge construction project. The framework analyses as-built data that is obtained using mobile lidar technology from a jobsite rapidly while ensuring the safety of the data collector. The proposed framework utilizes point cloud data and 4D design models to identify deviations of the performed work from the planned work. In order to achieve this, the framework was tested using as-built data acquired from an on-going bridge construction project. The as-built mobile laser scanning data was first registered with the 4D model. The progress information for each bridge component was calculated by segmenting a region of the point cloud that corresponds to each bridge component. Using the object recognition algorithm developed in the study, the percentage of bridge component that was completed on a given scan date was computed. Percentage of Completion (POC) for the as-built bridge elements are calculated and compared with the as-planned POC. The differences between these two POC values for each element, on a particular scan date, are used for assessing the performance of the proposed framework. The obtained difference between as-built and as-planned POC values ranged from -7% to 6% for most elements, which shows that the developed framework enables tracking the completion of individual bridge elements in an accurate and efficient manner. The framework overcomes the disadvantages associated with manual methods of progress tracking because field inspectors no longer have to rely on subjective data. Additionally, the progress tracking information is less prone to error because the results can be verified using the collected 3D point clouds. In addition, it saves the need to perform multiple site visits incase as-built data is not recorded properly.

The second study in this dissertation is described in Chapter 5. The main research question this study attempts to answer is ‘How can the traditional methods of measuring surface waviness along 1D lines be extended to measuring surface flatness along the 2D surface and provide a more comprehensive assessment of surface geometry?’

Chapter 5 proposes using TLS data for measuring floor flatness as opposed to the traditional methods. Using TLS data will enable assessing the surface flatness in a comprehensive manner because 2D/3D data is used to capture the overall geometry of the surface as opposed to 1D lines. In order to process TLS data for obtaining surface waviness information, a compliance-checking algorithm is presented for detecting elements where their dimensions exceed specified construction tolerances. First, the TLS data is cleaned to remove points associated with debris and workers on the surface. The TLS data is then converted into a depth map having 1 cm in both the x and y directions. The CWT is used to analyze the depth map to provide surface waviness information.

Thus, the framework enables assessment of a concrete surface in two-dimensional (2D) domain using the synergy of Terrestrial Laser Scanning (TLS) technology and Continuous Wavelet Transform (CWT) analysis. 2D CWT analysis provides information not only about the periods of the surface undulations, but also the location of such undulations. The traditional methods of measuring surface waviness are not efficient while measuring surface waviness over areas as large 45,000 sq. ft., which is the typical surface area of a warehouse floor.

The validity of the methodology is established by running a test on point clouds obtained from a warehouse project near Gresham, Oregon. A rigorous comparison between one of the existing floor waviness measurement methods, the waviness index method, and the proposed method is made. The results showed that the proposed methodology delivers accurate results that enable the localization of surface undulations of various characteristic

periods. This methodology will help quality control inspectors perform waviness assessment over large surface areas with minimal time and high accuracy.

Chapter 6 presented a comparative analysis of floor waviness measurement results obtained using UAV-based (mounted with a 3D laser scanning sensor) and TLS-based technologies. One of the major drawbacks in using point cloud data for as-built documentation is related to storing and processing large volumes of point cloud data. The main research question for this study is 'How does the resolution of point clouds affect the localization of surface defects?'

The TLS data from two projects are used to investigate how the quality of surface waviness results are affected by the scanning resolution. The point cloud data were analyzed at scanning resolutions of 0.02°, 0.04°, 0.06°, 0.08° and 0.1°, which are typical resolution settings for most commercially available TLS systems. The finding showed that for the Magruder Hall Expansion Project, using only one scan (in our case Scan 2) ensured that the CWT results matched the ground truth results for scanning resolutions ranging from 0.02° through 0.08°. If scans are collected from two scanning locations, scanning resolutions ranging from 0.02° through 0.1° can be used. Each of the scanning locations for the two scans may be as far as 12.46 m from the furthest point in the slab. Table 6.3 shows that this distance could have been 18.5 m but a conservative distance was chosen to generate accurate results. Note that the scanner is setup within the boundaries of the slab surface. The results from the Vista Logistic Park Project show using four scans (in our case Scan 1, Scan 2, Scan 3 and Scan 4) ensured that the CWT results matched the ground truth results for scanning resolutions ranging from 0.02° through 0.08°. Each of the scanning locations for the four scans may be as far as 22.69 m from the furthest point in the slab. Note that the scanner is setup within the boundaries of the slab surface. Furthermore, the results obtained from analyzing UAV-based point cloud data and TLS point cloud data for measuring floor flatness shows that comparable results are obtained for the scales of 30, 60 and 75. However, acceptable results for scales of 15 and 30 were not obtained. Thus, it

was concluded that UAV-based point cloud data on its own does not ensure localization of all kinds of surface undulations and TLS should be the preferred choice.

REFERENCES

[1] Construction Industry Institute (CII), “Guide to Activity Analysis,” 2010.

[2] National Research Council, “Advancing the Competitiveness and Efficiency of the U.S. Construction Industry,” 2009.

[3] McKinsey Global institute, “Reinventing Construction: A Route to Higher Productivity,” 2017.

[4] U. S. Census Bureau., “Value of construction put in place at a glance,” 2013.

[5] J. L. Burati and J. J. Farrington, "Costs of quality deviations in design and construction," Bureau of Engineering Research, University of Texas at Austin, 1987.

[6] L. Patterson and W. B. Ledbetter, “The cost of quality: A management tool,” in *Excellence in the Constructed Project*, 1989, pp. 100–105.

[7] P.-E. Josephson and Y. Hammarlund, “The causes and costs of defects in construction: A study of seven building projects,” *Automation in construction*, vol. 8, no. 6, pp. 681–687, 1999.

[8] P. Tang, B. Akinci, and D. Huber, “Characterization of three algorithms for detecting surface flatness defects from dense point clouds,” *IS&T/SPIE Electronic Imaging*, vol. 7239, p. 72390N–72390N, 2009.

[9] J.D. Owolabi, L.M. Amusan, C.O. Oloke, O. Olusanya, P.F. Tunji-Olayeni, O. Dele, N.J. Peter, I.O. Omuh, “Causes and effect of delay on project construction delivery time,” *International Journal of Education and Research*, vol. 2, no. 4, pp. 197–208, 2014.

[10] Y. Turkan, F. Bosche, C. T. Haas, and R. Haas, “Automated progress tracking using 4D schedule and 3D sensing technologies,” *Automation in Construction*, vol. 22, pp. 414–421, 2012.

[11] Y. Turkan, F. Bosche, C. T. Haas, and R. Haas, “Tracking Secondary and Temporary Concrete Construction Objects Using 3D Imaging Technologies,” *Computing in Civil Engineering*, pp. 749–756, 2013.

[12] S. El-omari and O. Moselhi, “Automation in Construction Integrating 3D laser scanning and photogrammetry for progress measurement of construction work,” vol. 18, pp. 1–9, 2008.

[13] M. Golparvar-Fard, F. Peña Mora, and S. Silvio, “D4AR-A 4-dimensional augmented reality model for automating construction progress monitoring data collection, processing and communication,” *Electronic Journal of Information*

Technology in Construction, vol. 14, no. June, pp. 129–153, 2009.

[14] A. Braun, A. Borrmann, S. Tuttas, and U. Stilla, "Towards automated construction progress monitoring using BIM-based point cloud processing," *eWork and eBusiness in Architecture, Engineering and Construction - Proceedings of the 10th European Conference on Product and Process Modelling, ECPPM 2014*, pp. 101–107, 2015.

[15] A. Braun, S. Tuttas, A. Borrmann, and U. Stilla, "Automated progress monitoring based on photogrammetric point clouds and precedence relationship graphs," *Proceedings of the 32nd International Symposium on Automation and Robotics in Construction and Mining*, pp. 274–280, 2015.

[16] H. Son, C. Kim, and Y. Kwon Cho, "Automated Schedule Updates Using As-Built Data and a 4D Building Information Model," *Journal of Management in Engineering*, vol. 33, no. 4, p. 4017012, 2017.

[17] C. Kim, H. Son, and C. Kim, "Automated construction progress measurement using a 4D building information model and 3D data," *Automation in Construction*, vol. 31, pp. 75–82, 2013.

[18] Z. Pučko, N. Šuman, and D. Rebolj, "Automated continuous construction progress monitoring using multiple workplace real time 3D scans," *Advanced Engineering Informatics*, vol. 38, pp. 27–40, 2018.

[19] C. Zhang and D. Arditi, "Automation in Construction Automated progress control using laser scanning technology," *Automation in Construction*, vol. 36, pp. 108–116, 2013.

[20] H. P. Gillette, C. S. Hill, C. T. Murray, H. B. Kirkland, and S. C. Hadden, *Engineering and Contracting*, no. v. 39. Gillette Publishing Company, 1913.

[21] F. Bosché and E. Guenet, "Automating surface flatness control using terrestrial laser scanning and building information models," *Automation in Construction*, vol. 44, pp. 212–226, 2014.

[22] F. Bosché and B. Biotteau, "Terrestrial laser scanning and continuous wavelet transform for controlling surface flatness in construction – A first investigation," *Advanced Engineering Informatics*, vol. 29, pp. 591–601, 2015.

[23] American Road & Transportation Builders Association, "U.S. Transportation Construction Market Forecast 2017," 2017.

[24] American Society Of Civil Engineers (ASCE), "Report Card for America's Infrastructure," 2017. [Online]. Available: https://www.infrastructurereportcard.org/.

[25] American Society Of Civil Engineers (ASCE), “Failure To Act : Closing the Infrastructure Investment Gap for America’s Economic Future,” 2016.

[26] P. A. Nee, *ISO 9000 in Construction*. John Wiley & Sons, 1996.

[27] A. Bhargava, P. C. Anastasopoulos, S. Labi, K. C. Sinha, and F. L. Mannering, “Three-stage least-squares analysis of time and cost overruns in construction contracts,” *Journal of Construction Engineering and Management*, vol. 136, no. 11, pp. 1207–1218, 2010.

[28] C. C. Cantarelli, B. Flyvbjerg, E. J. E. Molin, and B. van Wee, “Cost overruns in large-scale transportation infrastructure projects: Explanations and their theoretical embeddedness,” *European Journal of Transport and Infrastructure Research*, vol. 10, no. 1, pp. 5–18, 2010.

[29] B. Flyvbjerg, M. K. Skamris Holm, and S. L. Buhl, “How common and how large are cost overruns in transport infrastructure projects?,” *Transport reviews*, vol. 23, no. 1, pp. 71–88, 2003.

[30] S. M. Vick and I. Brilakis, “A Review of Linear Transportation Construction Progress Monitoring Techniques,” *Proceedings of the 16th International Conference on Computing in Civil and Building Engineering*, no. July, pp. 1106–1113, 2016.

[31] D. K. Ballast, *Handbook of Construction Tolerances*, Second. John Wiley & Sons, 2007.

[32] *Manual for Quality Control for Structural Precast Concrete Products*, 4th Editio. Precast Concrete Institute, 1999.

[33] F. R. Neal, *Concrete Industrial Ground Floors*. Thomas Telford, 2002.

[34] B. M. Phares, G. a. Washer, D. D. Rolander, B. a. Graybeal, and M. Moore, “Routine Highway Bridge Inspection Condition Documentation Accuracy and Reliability,” *Journal of Bridge Engineering*, vol. 9, no. 4, pp. 403–413, 2004.

[35] American Society for Testing and Materials (ASTM), “Standard Test Method for Determining F F Floor Flatness and F L Floor Levelness Numbers (Metric) 1,” ASTM, vol. 96, no. Reapproved 2008, pp. 7–14, 2015.

[36] American Society for Testing and Materials (ASTM), “Standard Test Method for Determining Floor Tolerances Using Waviness , Wheel Path,” ASTM vol. 04, no. November 1998, pp. 1–12, 2004.

[37] C. N. Ytterberg, “Using the Waviness Index To Improve Floor Flatness,” 1996.

[38] R. E. Loov, “Is the F-number system valid for your floor?,” *Concrete International*,

vol. 12, no. 1, pp. 68–76, 1990.

[39] D. Bryde, M. Broquetas, and J. M. Volm, “The project benefits of building information modelling (BIM),” *International Journal of Project Management*, vol. 31, no. 7, pp. 971–980, 2013.

[40] C. Eastman, P. Teicholz, R. Sacks, and K. Liston, *BIM Handbook: A Guide to Building Information Modeling for Owners, Managers, Designers, Engineers and Contractors*. Wiley Publishing, 2008.

[41] P. Teicholz, *BIM for Facility Managers*. Hoboken, NJ: Wiley, 2013.

[42] F. Levy, *BIM in Small-Scale Sustainable Design*. Wiley, 2011.

[43] M. J. Olsen, F. Kuester, B. J. Chang, and T. C. Hutchinson, “Terrestrial Laser Scanning-Based Structural Damage Assessment,” *Journal of Computing in Civil Engineering*, vol. 24, no. 3, pp. 264–272, 2010.

[44] M. Nuikka *et al.*, “Comparison of three accurate 3D measurement methods for evaluating as-built floor flatness,” *ISPRS Archives*, vol. XXXVII, no. part B5, pp. 129–134, 2008.

[45] M. Golparvar-Fard, J. Bohn, J. Teizer, S. Savarese, and F. Peña-Mora, “Evaluation of image-based modeling and laser scanning accuracy for emerging automated performance monitoring techniques,” *Automation in Construction*, vol. 20, no. 8, pp. 1143–1155, 2011.

[46] V. Gikas, “Three-dimensional laser scanning for geometry documentation and construction management of highway tunnels during excavation.,” *Sensors (Basel, Switzerland)*, vol. 12, no. 8, pp. 11249–70, 2012.

[47] “Tolerances in concrete construction ,” Editorial staff of concrete construction.

[48] M.-K. Kim, J. C. P. Cheng, H. Sohn, and C.-C. Chang, “A framework for dimensional and surface quality assessment of precast concrete elements using BIM and 3D laser scanning,” *Automation in Construction*, vol. 49, pp. 225–238, 2015.

[49] F. Bosché, “Automated recognition of 3D CAD model objects in laser scans and calculation of as-built dimensions for dimensional compliance control in construction,” *Advanced Engineering Informatics*, vol. 24, no. 1, pp. 107–118, 2010.

[50] M.-K. Kim, H. Sohn, and C.-C. Chang, “Automated dimensional quality assessment of precast concrete panels using terrestrial laser scanning,” *Automation in Construction*, vol. 45, no. September, pp. 163–177, 2014.

[51] Y. Turkan, F. Bosche, C. T. Haas, and R. Haas, “Automated progress tracking using 4D schedule and 3D sensing technologies,” *Automation in Construction*, vol. 22, pp.

414–421, 2012.

[52] D. Cotts, "The Facility Management Handbook Second Edition AMACM, 1998." ISBN: 0-8144-030-8.

[53] F. Al-shalabi and Y. Turkan, “A novel framework for BIM enabled facility energy management – A concept paper,” pp. 1–8, 2015.

[54] B. Becerik-Gerber, F. Jazizadeh, and N. Li, “Application areas and data requirements for BIM-enabled facilities management,” *and Management*, vol. 138, no. March, pp. 431–442, 2011.

[55] L. Y. Liu, A. L. Stumpf, S. S. Kim, and F. M. Zbinden, “Capturing as-built project information for facility management,” in *Computing in Civil Engineering*, 1994, pp. 614–621.

[56] T. Minato, “Representing causal mechanism of defective designs: a system approach considering human errors,” *Construction Management and Economics*, vol. 21, no. 3, pp. 297–305, 2003.

[57] S. Talebi, L. Koskela, M. Shelbourn, and P. Tzortzopoulos, “Critical Review of Tolerance Management in Construction,” 2016.

[58] M. Alshawi and J. Underwood, “Improving the constructability of design solutions through an integrated system,” *Engineering, Construction and Architectural Management*, vol. 3, no. 1/2, pp. 47–67, 1996.

[59] P. Teicholz, P. M. Goodrum, and C. T. Haas, “US construction labor productivity trends, 1970--1998,” *Journal of Construction Engineering and Management*, vol. 127, no. 5, pp. 427–429, 2001.

[60] H. D. Jeong, "Framework for Advanced Daily Work Report System" No. WBS: 25-1121-003-238. 2015.

[61] S. Gezici *et al.*, “Localization via ultra-wideband radios: a look at positioning aspects for future sensor networks,” *IEEE signal processing magazine*, vol. 22, no. 4, pp. 70–84, 2005.

[62] J. Teizer, D. Lao, and M. Sofer, “Rapid automated monitoring of construction site activities using ultra-wideband,” in *Proceedings of the 24th International Symposium on Automation and Robotics in Construction, Kochi, Kerala, India*, 2007, pp. 19–21.

[63] T. Cheng, M. Venugopal, J. Teizer, and P. A. Vela, “Performance evaluation of ultra wideband technology for construction resource location tracking in harsh environments,” *Automation in Construction*, vol. 20, no. 8, pp. 1173–1184, 2011.

[64] S. Kiziltas, B. Akinci, E. Ergen, P. Tang, and C. Gordon, "Technological assessment and process implications of field data capture technologies for construction and facility/infrastructure management," *Electronic Journal of Information Technology in Construction*, vol. 13, pp. 134–154, 2008.

[65] K. M. Furlani and L. E. Pfeffer, "Automated tracking of structural steel members at the construction site," *Proceedings of 17th ISARC*, pp. 1201–1206, 2000.

[66] S. Chin, S. Yoon, C. Choi, and C. Cho, "RFID+ 4 D CAD for progress management of structural steel works in high-rise buildings," *Journal of Computing in Civil Engineering*, vol. 22, no. 2, pp. 74–89, 2008.

[67] J. J. Lin, K. K. Han, and M. Golparvar-Fard, "A framework for model-driven acquisition and analytics of visual data using UAVs for automated construction progress monitoring," in *Computing in Civil Engineering 2015*, 2015, pp. 156–164.

[68] J. Lin, K. Han, Y. Fukuchi, M. Eda, and M. Golparvar-Fard, "Model based Monitoring of work in progress via Images Taken by Camera equipped UAV and BIM," in *Proc., 2015 International Conference on Civil and Building Engineering Informatics*, 2015.

[69] A. Braun, S. Tuttas, A. Borrmann, and U. Stilla, "A concept for automated construction progress monitoring using BIM-based geometric constraints and photogrammetric point clouds," *Journal of Information Technology in Construction (ITcon)*, vol. 20, no. 5, pp. 68–79, 2015.

[70] K. Han, J. Lin, and M. Golparvar-Fard, "A formalism for utilization of autonomous vision-based systems and integrated project models for construction progress monitoring," in *Proc., 2015 Conference on Autonomous and Robotic Construction of Infrastructure*, 2015.

[71] K. Karsch, M. Golparvar-Fard, and D. Forsyth, "ConstructAide: analyzing and visualizing construction sites through photographs and building models," *ACM Transactions on Graphics (TOG)*, vol. 33, no. 6, p. 176, 2014.

[72] J. S. Bohn and J. Teizer, "Benefits and barriers of construction project monitoring using high-resolution automated cameras," *Journal of construction engineering and management*, vol. 136, no. 6, pp. 632–640, 2009.

[73] C. Zhang and D. Arditi, "Automated progress control using laser scanning technology," *Automation in Construction*, vol. 36, pp. 108–116, 2013.

[74] A. Braun, S. Tuttas, U. Stilla, and A. Borrmann, "Incorporating knowledge on construction methods into automated progress monitoring techniques," *23rd International Workshop of the European Group for Intelligent Computing in Engineering, At Kraków, Poland*, vol. 23, pp. 1–11, 2016.

[75] J. Hernández and B. Marcotegui, “Filtering of artifacts and pavement segmentation from mobile lidar data,” in *ISPRS Workshop Laserscanning 2009*, 2009.

[76] B. Riveiro, H. González-Jorge, J. Martinez-Sánchez, L. Diaz-Vilariño, and P. Arias, “Automatic detection of zebra crossings from mobile LiDAR data,” *Optics & Laser Technology*, vol. 70, pp. 63–70, 2015.

[77] J. Jung, E. Che, M. J. Olsen, and C. Parrish, “Efficient and robust lane marking extraction from mobile lidar point clouds,” *ISPRS Journal of Photogrammetry and Remote Sensing*, vol. 147, pp. 1–18, 2019.

[78] P. Kumar, C. P. McElhinney, P. Lewis, and T. McCarthy, “An automated algorithm for extracting road edges from terrestrial mobile LiDAR data,” *ISPRS journal of photogrammetry and remote sensing*, vol. 85, pp. 44–55, 2013.

[79] E. Che and M. J. Olsen, “An Efficient Framework for Mobile Lidar Trajectory Reconstruction and Mo-norvana Segmentation,” *Remote Sensing*, vol. 11, no. 7, 2019.

[80] A. Mitchell, E. Gensib, S. Sadasivam, T. Day, J. Gustafson, J. Bartlett, and T. Bonzelet, “3D Highway Design Model Cost Benefit Analysis,” 2019.

[81] B. Sankaran, G. Nevett, W. J. O’Brien, P. M. Goodrum, and J. Johnson, “Civil Integrated Management: Empirical study of digital practices in highway project delivery and asset management,” *Automation in Construction*, vol. 87, pp. 84–95, 2018.

[82] R. Navon and Y. Shpatnitsky, “A model for automated monitoring of road construction,” *Construction Management and Economics*, vol. 23, no. 9, pp. 941–951, 2005.

[83] N. Pradhananga and J. Teizer, “Automatic spatio-temporal analysis of construction site equipment operations using GPS data,” *Automation in Construction*, vol. 29, pp. 107–122, 2013.

[84] S. Siebert and J. Teizer, “Mobile 3D mapping for surveying earthwork projects using an Unmanned Aerial Vehicle (UAV) system,” *Automation in Construction*, vol. 41, pp. 1–14, 2014.

[85] A. Vasenev, N. Pradhananga,F. R. Bijleveld, D. Ionita, T. Hartmann, J. Teizer, and A. G. Doree, “An information fusion approach for filtering GNSS data sets collected during construction operations,” *Advanced engineering informatics*, vol. 28, no. 4, pp. 297–310, 2014.

[86] E. J. Jaselskis, Z. Gao, A. Welch, and D. O’Brien, “Pilot study on laser scanning technology for transportation projects,” in *Mid-Continent Transportation Research Symposium*, 2003.

[87] S. Vick and I. Brilakis, “Road Design Layer Detection in Point Cloud Data for Construction Progress Monitoring,” *Journal of Computing in Civil Engineering*, vol. 32, no. 5, p. 4018029, 2018.

[88] German Institute of Standardization, DIN 18202, “Tolerances in building construction – Buildings,” 2005.

[89] National Research Council of Canada - Institute for Research in Construction , “Inaccuracies in Construction,” *Canadian Building Digests*, Ottawa, p. 171, 1975.

[90] G. S. Cheok, W. C. Stone, R. R. Lipman, C. Witzgall, and J. Uisod, “Ladars for construction assessment and update,” vol. 9, no. 5, pp. 463–477, 2000.

[91] H. Son and C. Kim, “Advanced Engineering Informatics Semantic as-built 3D modeling of structural elements of buildings based on local concavity and convexity,” *Advanced Engineering Informatics*, vol. 34, no. August, pp. 114–124, 2017.

[92] S. Tuttas, A. Braun, A. Borrmann, and U. Stilla, “Comparision of photogrammetric point clouds with BIM building elements for construction progress monitoring,” *The International Archives of Photogrammetry, Remote Sensing and Spatial Information Sciences*, vol. 40, no. 3, p. 341, 2014.

[93] M.-C. Amann, T. Bosch, M. Lescure, R. Myllyla, and M. Rioux, “Laser ranging: a critical review of usual techniques for distance measurement,” *Optical Engineering*, vol. 40, no. 1, pp. 10–19, 2001.

[94] P. A. Fuchs, G. A. Washer, S. B. Chase, and M. Moore, “Applications of Laser-Based Instrumentation for Highway Bridges,” *Journal of Bridge Engineering*, vol. 9, no. 6, pp. 541–549, 2004.

[95] T. Schafer and T. Weber, “Deformation measurement using terrestrial laser scanning at the hydropower station of Gabcikovo,” in *INGEO 2004 and FIG Regional Central and Eastern European Conference on Engineering Surveying, FIG, Copenhagen, Denmark.*, 2004.

[96] M. C. Israel and R. G. Pileggi, “Use of 3D laser scanning for flatness and volumetric analysis of mortar in facades,” vol. 9, no. 1, pp. 91–106, 2016.

[97] Q. Wang, M. Kim, J. C. P. Cheng, and H. Sohn, “Automated quality assessment of precast concrete elements with geometry irregularities using terrestrial laser scanning,” *Automation in Construction*, 2016.

[98] N.-J. Shih and P.-H. Wang, “Using point cloud to inspect the construction quality of wall finish,” *Proceedings of the 22nd eCAADe Conference*, no. October, pp. 573–578, 2004.

[99] P. Goupillaud, A. Grossmann, and J. Morlet, “Cycle-octave and related transforms in seismic signal analysis,” *Geoexploration*, vol. 23, no. 1, pp. 85–102, 1984.

[100] R. Kronland-Martinet, J. Morlet, and A. Grossman, “Analysis of sound patterns through wavelet transforms ,” *International Journal of Pattern Recognition and Artificial Intelligence*, vol. 01, no. 02, pp. 273–302, 1987.

[101] T. Paul, “Functions analytic on the half-plane as quantum mechanical states,” *Journal of Mathematical Physics*, vol. 25, no. 11, pp. 3252–3263, 1984.

[102] J. Raja, B. Muralikrishnan, and S. Fu, “Recent advances in separation of roughness, waviness and form,” *Precision Engineering*, vol. 26, no. 2, pp. 222–235, 2002.

[103] Y. Ge, H. Tang, M. A. M. E. Eldin, P. Chen, L. Wang, and J. Wang, “A Description for Rock Joint Roughness Based on Terrestrial Laser Scanner and Image Analysis,” *Nature Publishing Group*, pp. 1–10, 2015.

[104] M. Bitenc, D. S. Kieffer, and K. Khoshelham, “Evaluation of Wavelet Denoising Methods for Small-Scale Joint Roughness Estimation Using Terrestrial Laser Scanning,” *ISPRS Annals of Photogrammetry, Remote Sensing and Spatial Information Sciences*, vol. II-3/W5, pp. 81–88, 2015.

[105] K. Khoshelham and D. Altundag, “Wavelet De-Noising of Terrestrial Laser Scanner Data for the Characterization of Rock Surface Roughness,” vol. 38, pp. 373–378, 1998.

[106] S. Chen, X., Raja, J., Simanapalli, “Multi-Scale Analysis of Engineering Surfaces,” vol. 35, no. 2, pp. 231–238, 1995.

[107] B. Josso, D. R. Burton, and M. J. Lalor, “Frequency normalised wavelet transform for surface roughness analysis and characterisation,” vol. 252, pp. 491–500, 2002.

[108] K. Stępień and W. Makieła, “An analysis of deviations of cylindrical surfaces with the use of wavelet transform,” vol. XX, no. 1, pp. 139–150, 2013.

[109] X. Q. Jiang, L. Blunt, and K. J. Stout, “Lifting wavelet for three-dimensional surface analysis,” vol. 41, pp. 2163–2169, 2001.

[110] R. R. Coifman and M. Maggioni, “Diffusion Wavelets,” no. April, 2006.

[111] S. Hussein, J. Paul, H. S. Abdul-rahman, X. J. Jiang, and P. J. Scott, “Freeform Surface Filtering Using the Lifting Wavelet Transform,” 2012.

[112] D. Mendlovic and N. Konforti, “Optical realization of the wavelet transform for two-dimensional objects,” *Appl. Opt.*, vol. 32, no. 32, pp. 6542–6546, Nov. 1993.

[113] V. V. Valenzuela, R. D. Lins, and H. M. De Oliveira, “Application of enhanced-2D-

CWT in topographic images for mapping landslide risk areas," *Lecture Notes in Computer Science (including subseries Lecture Notes in Artificial Intelligence and Lecture Notes in Bioinformatics)*, vol. 7950 LNCS, pp. 380–388, 2013.

[114] R. Polikar, "The Wavelet Tutorial," 1994.

[115] P. S. Addison, *The Illustrated Wavelet Transform Handbook: Introductory Theory and Applications in Science, Engineering, Medicine and Finance*, 1st Ed. CRC Press, 2002.

[116] I. Daubechies, *Ten Lectures on Wavelets*. Philadelphia, PA: Society for Industrial and Applied Mathemetics, 1992.

[117] N. Wang and C. Lu, "Two-dimensional continuous wavelet analysis and its application to meteorological data," *Journal of Atmospheric and Oceanic Technology*, vol. 27, no. 4, pp. 652–666, 2010.

[118] J.-P. Antione, R. Murenzi, P. Vandergheynst, and S. T. Ali, *Two-Dimensional Wavelets and Their Relatives*. Cambridge University Press, 2008.

[119] R. Leach, *Characterisation of Areal Surface Texture*. Springer Berlin Heidelberg, 2013.

[120] R. X. Gao and R. Yan, *Wavelets: Theory and applications for manufacturing*. Springer Science & Business Media, 2010.

[121] E. H. D. Marr, "Theory of Edge Detection," *Proceedings of the Royal Society of London. Series B, Biological Sciences*, vol. 207, no. 1167, pp. 187–217, 1980.

[122] J. P. Antoine and R. Murenzi, "Two-dimensional directional wavelets and the scale-angle representation," *Signal Processing*, vol. 52, no. 3, pp. 259–281, 1996.

[123] M. J. Olsen, J. C. Allan, and G. R. Priest, "Movement and Erosion Quantification of the Johnson Creek, Oregon, Landslide through 3D Laser Scanning," in *GeoCongress 2012: State of the Art and Practice in Geotechnical Engineering*, 2012, pp. 3050–3059.

[124] B. A. Leshchinsky, M. J. Olsen, and K. Hall, "Enhancing Landslide Inventorying, Lidar Hazard Assessment and Asset Management ," No. FHWA-OR-RD-18-18. Oregon. Dept. of Transportation. Research Section, 2018.

[125] X. Xu, H. Yang, and I. Neumann, "Concrete crack measurement and analysis based on terrestrial laser scanning technology," *Sensors and Transducers Journal*, vol. 186, no. 3, pp. 168–172, 2015.

[126] Y. Turkan, S. Laflamme, and L. Tan, "Terrestrial Laser Scanning-Based Bridge Structural Condition Assessment," 2016.

[127] Y. Turkan, J. Hong, S. Laflamme, and N. Puri, “Adaptive wavelet neural network for terrestrial laser scanner-based crack detection,” *Automation in Construction*, vol. 94, no. July, pp. 191–202, 2018.

[128] A. Alhasan, D. J. White, and K. De Brabanter, “Wavelet Filter Design for Pavement Roughness Analysis,” *Computer-Aided Civil and Infrastructure Engineering*, vol. 31, no. 12, pp. 907–920, 2016.

[129] A. Alhasan, D. J. White, and K. De Brabanterb, “Automation in Construction Continuous wavelet analysis of pavement profiles,” vol. 63, pp. 134–143, 2016.

[130] A. Alhasan, D. J. White, and K. De Brabanter, “Spatial pavement roughness from stationary laser scanning,” *International Journal of Pavement Engineering*, vol. 18, no. 1, pp. 83–96, 2017.

[131] P. Kumar, P. Lewis, C. P. Mcelhinney, and A. A. Rahman, “An algorithm for automated estimation of road roughness from mobile laser scanning data,” *Photogrammetric Record*, vol. 30, no. 149, pp. 30–45, 2015.

[132] A. Chin, M. J. Olsen, D. Ph, and A. M. Asce, “Evaluation of Technologies for Road Profile Capture, Analysis, and Evaluation,” *Journal of Surveying Engineering*, vol. 141, no. 1, pp. 1–13, 2015.

[133] E. Valero, F. Bosché, and A. Forster, “Automatic segmentation of 3D point clouds of rubble masonry walls, and its application to building surveying, repair and maintenance,” *Automation in Construction*, vol. 96, no. May, pp. 29–39, 2018.

[134] E. Valero, F. Bosché, A. Forster, L. Wilson, and A. Leslie, “Evaluation of historic masonry--Towards greater objectivity and efficiency,” *Heritage Building Information Modelling. Taylor & Francis*, 2017.

[135] S. Fai, K. Graham, T. Duckworth, N. Wood, and R. Attar, “Building Information Modelling and Heritage Documentation,” *XXIII CIPA International Symposium, Prague, Czech Republic*, 2011.

[136] M.-K. Kim, Q. Wang, J.-W. Park, J. C. P. Cheng, H. Sohn, and C.-C. Chang, “Automated dimensional quality assurance of full-scale precast concrete elements using laser scanning and BIM,” *Automation in Construction*, vol. 72, pp. 102–114, 2016.

[137] N. Puri, E. Valero, Y. Turkan, and F. Bosché, “Assessment of compliance of dimensional tolerances in concrete slabs using TLS data and the 2D continuous wavelet transform,” *Automation in Construction*, vol. 94, no. May, pp. 62–72, 2018.

[138] E. Valero and F. Bosché, “Automatic Surface Flatness Control using Terrestrial Laser Scanning Data and the 2D Continuous Wavelet Transform,” no. Isarc, p. 2016, 2016.

[139] M. J. Olsen, J. Raugust, and G.V. Roe, *Use of Advanced Geospatial Data, Tools, Technologies, and Information in Department of Transportation Projects*. Vol. 446. Transportation Research Board, 2013.

[140] R. A. Vincent, M. Ecker, and others, "Light detection and ranging (LiDAR) technology evaluation.," 2010.

[141] M. J. Olsen, G. V. Roe, C. Glennie, F. Persi, M. Reedy, D. Hurwitz, K. Williams, H. Tuss, A. Squellati, and M. Knodler, *Guidelines for the use of mobile LIDAR in transportation applications*, vol. 748. Transportation Research Board, 2013.

[142] P. J. Besl and N. D. McKay, "Method for registration of 3-D shapes," in *Sensor Fusion IV: Control Paradigms and Data Structures*, 1992, vol. 1611, pp. 586–607.

[143] M. M. Kanafi and A. J. Tuononen, "Top topography surface roughness power spectrum for pavement friction evaluation," *Tribology International*, vol. 107, pp. 240–249, 2017.

[144] S. Krishnamachari and R. Chellappa, "Multiresolution Gauss-Markov random field models for texture segmentation," *IEEE Transactions on image processing*, vol. 6, no. 2, pp. 251–267, 1997.

[145] R. Azencott, J.-P. Wang, and L. Younes, "Texture classification using windowed Fourier filters," *IEEE Transactions on Pattern Analysis & Machine Intelligence*, no. 2, pp. 148–153, 1997.

[146] F. S. Cohen and Z. Fan, "Rotation and scale invariant texture classification," in *Proceedings. 1988 IEEE International Conference on Robotics and Automation*, 1988, pp. 1394–1399.

[147] J. S. Weszka, C. R. Dyer, and A. Rosenfeld, "A comparative study of texture measures for terrain classification," *IEEE transactions on Systems, Man, and Cybernetics*, no. 4, pp. 269–285, 1976.

[148] R. N. Bracewell and R. N. Bracewell, *The Fourier transform and its applications*, vol. 31999. McGraw-Hill New York, 1986.

[149] H.-J. Kim and M. Fuentes, "Spectral analysis with spatial periodogram and data tapers," in *Proceedings Joint Statistical Meeting*, 2000.

[150] N. Puri and Y. Turkan, "Dimensional Quality Control of Concrete Slabs using 3D laser Scan Point Clouds," in *Proc. of the 16th International Conference on Construction Applications of Virtual Reality (CONVR)*, 2016.

[151] S. Kunis, "Nonequispaced FFT: Generalisation and Inversion," *Phd Thesis*, pp. 1–105, 2007.

[152] Leica Geosystems, “Leica ScanStation P30/P40 product specifications,” *Heerbrugg, Switzerland,* 2016.

APPENDICES

A.1: CWT results from Chapter 6

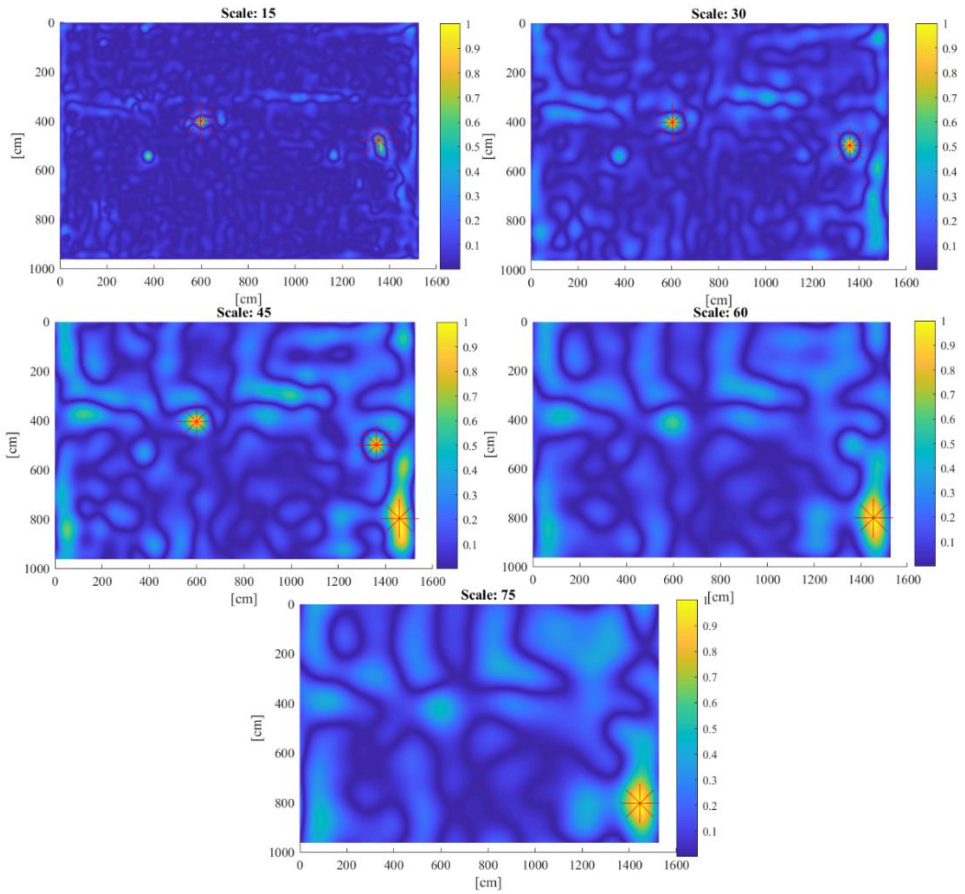

Figure A.1- 1 The coefficients obtained from the wavelet transformation corresponding to scales 15 (a), 30 (b), 45 (c), 60 (d) and 75 (e) are plotted on the map for Scan 1 of the Magruder Hall slab. The areas in the slabs where undulations corresponding to these scales are present are shown. The peaks are marked in red. The scan is at scanning resolution 0.02°.

Table A.1- 1 Peak detection results for Scan 1 (Magruder Hall Expansion Project) at scanning resolution 0.02°

Scales	Number of peaks correctly identified	Number of peaks incorrectly identified or failed to identify	Actual number of peaks (based on 0.01° scanning resolution)
15	**2**	**1**	**3**
30	**1**	**1**	**1**
45	**1**	**2**	**1**
60	**1**	**0**	**1**
75	**1**	**0**	**1**

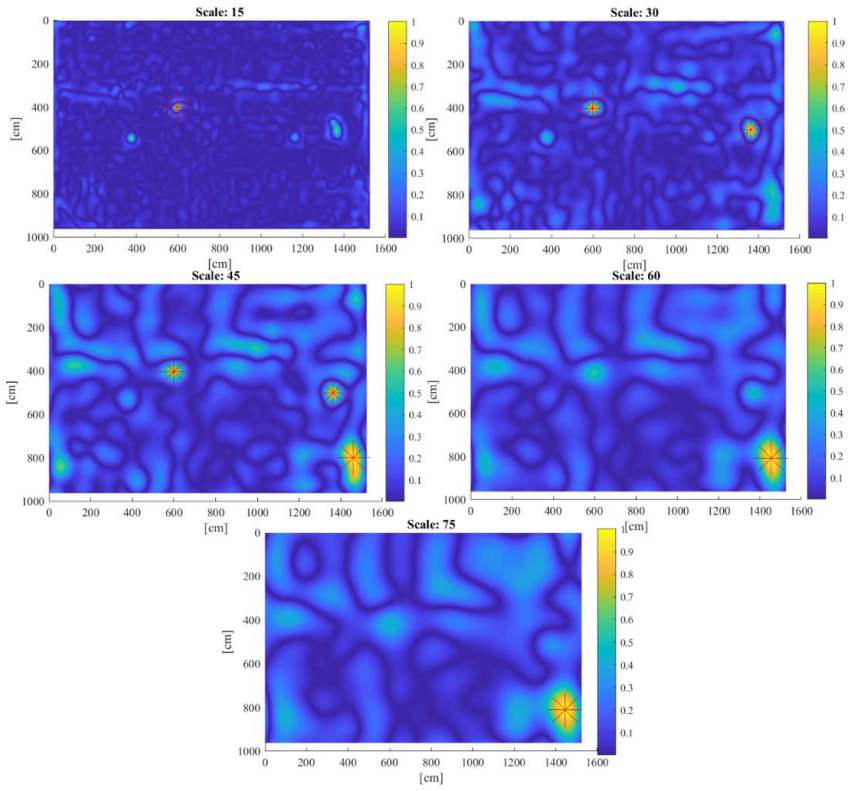

Figure A.1- 2 The coefficients obtained from the wavelet transformation corresponding to scales 15 (a), 30 (b), 45 (c), 60 (d) and 75 (e) are plotted on the map for Scan 1 of the Magruder Hall slab. The areas in the slabs where undulations corresponding to these scales are present are shown. The peaks are marked in red. The scan is at scanning resolution 0.04°.

Table A.1- 2 Peak detection results for Scan 1 (Magruder Hall Expansion Project) at scanning resolution 0.04°

Scales	Number of peaks correctly identified	Number of peaks incorrectly identified or failed to identify	Actual number of peaks (based on 0.01° scanning resolution)
15	**0**	**3**	**3**
30	**1**	**1**	**1**
45	**1**	**2**	**1**
60	**1**	**0**	**1**
75	**1**	**0**	**1**

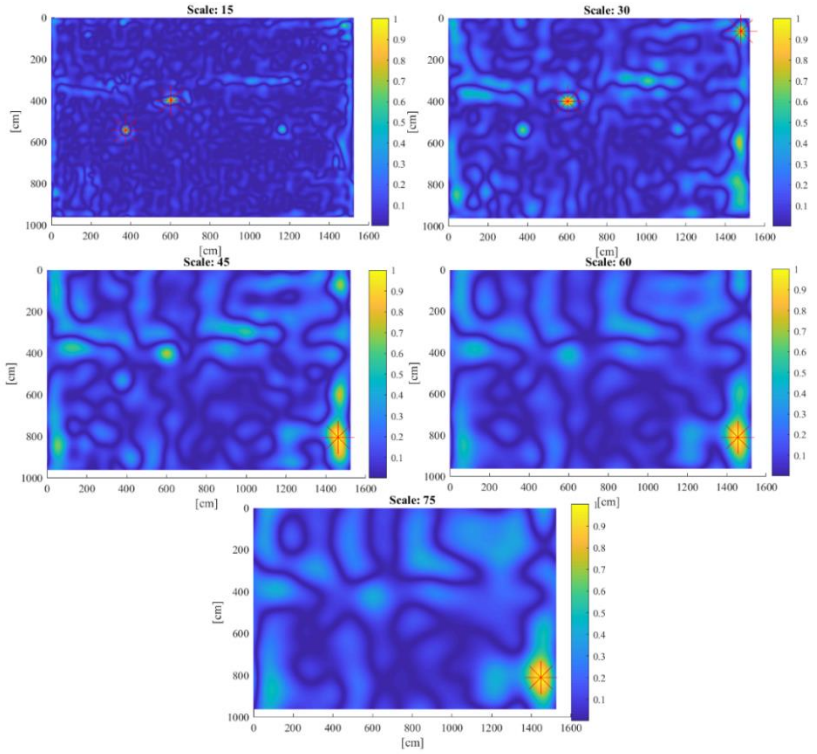

Figure A.1- 3 The coefficients obtained from the wavelet transformation corresponding to scales 15 (a), 30 (b), 45 (c), 60 (d) and 75 (e) are plotted on the map for Scan 1 the Magruder Hall slab. The areas in the slabs where undulations corresponding to these scales are present are shown. The peaks are marked in red. The scan is at scanning resolution 0.06°.

Table A.1- 3 Peak detection results for Scan 1 (Magruder Hall Expansion Project) at scanning resolution 0.06°

Scales	Number of peaks correctly identified	Number of peaks incorrectly identified or failed to identify	Actual number of peaks (based on 0.01° scanning resolution)
15	**1**	**3**	**3**
30	**1**	**1**	**1**
45	**1**	**0**	**1**
60	**1**	**0**	**1**
75	**1**	**0**	**1**

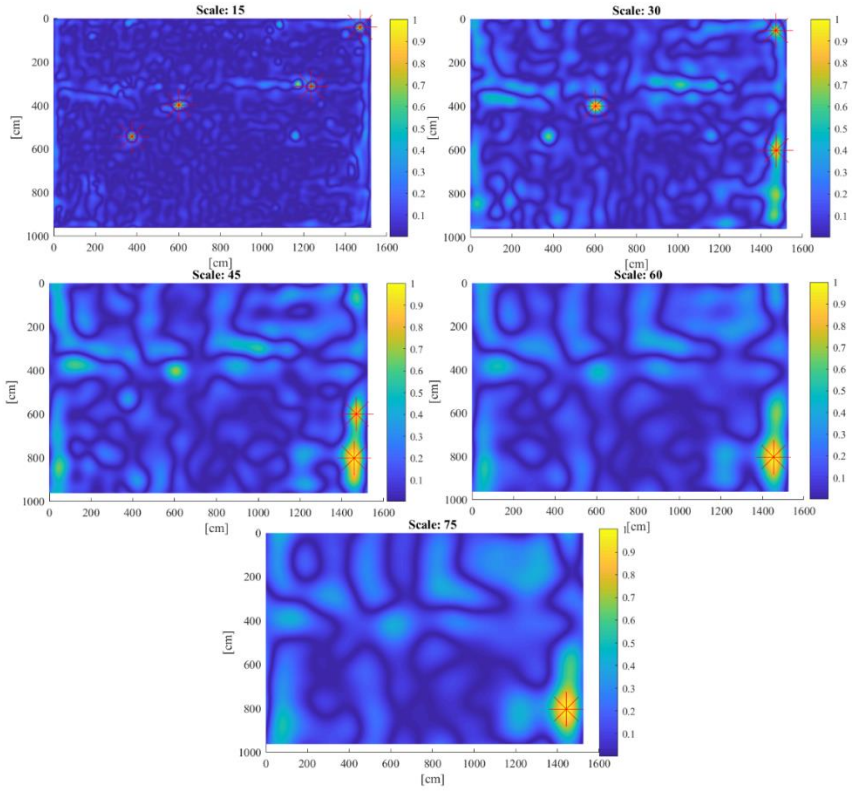

Figure A.1- 4 The coefficients obtained from the wavelet transformation corresponding to scales 15 (a), 30 (b), 45 (c), 60 (d) and 75 (e) are plotted on the map for Scan 1 of the Magruder Hall slab. The areas in the slabs where undulations corresponding to these scales are present are shown. The peaks are marked in red. The scan is at scanning resolution 0.08°.

Table A.1- 4 Peak detection results for Scan 1 (Magruder Hall Expansion Project) at scanning resolution 0.08°

Scales	Number of peaks correctly identified	Number of peaks incorrectly identified or failed to identify	Actual number of peaks (based on 0.01° scanning resolution)
15	**1**	**3**	**3**
30	**1**	**1**	**1**
45	**1**	**1**	**1**
60	**1**	**0**	**1**
75	**1**	**0**	**1**

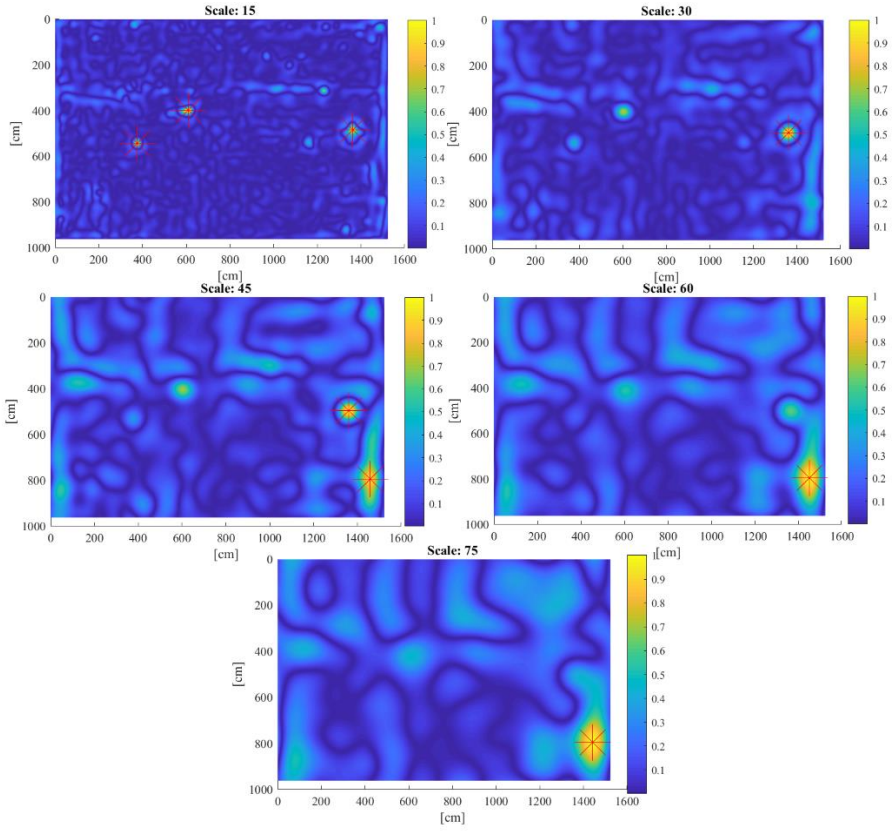

Figure A.1- 5 The coefficients obtained from the wavelet transformation corresponding to scales 15 (a), 30 (b), 45 (c), 60 (d) and 75 (e) are plotted on the map for the Magruder Hall slab. The areas in the slabs where undulations corresponding to these scales are present are shown. The peaks are marked in red. The scan is at scanning resolution 0.1°.

Table A.1- 5 Peak detection results for Scan 1 (Magruder Hall Expansion Project) at scanning resolution 0.10°

Scales	Number of peaks correctly identified	Number of peaks incorrectly identified or failed to identify	Actual number of peaks (based on 0.01° scanning resolution)
15	**2**	**1**	**3**
30	**1**	**0**	**1**
45	**1**	**1**	**1**
60	**1**	**0**	**1**
75	**1**	**0**	**1**

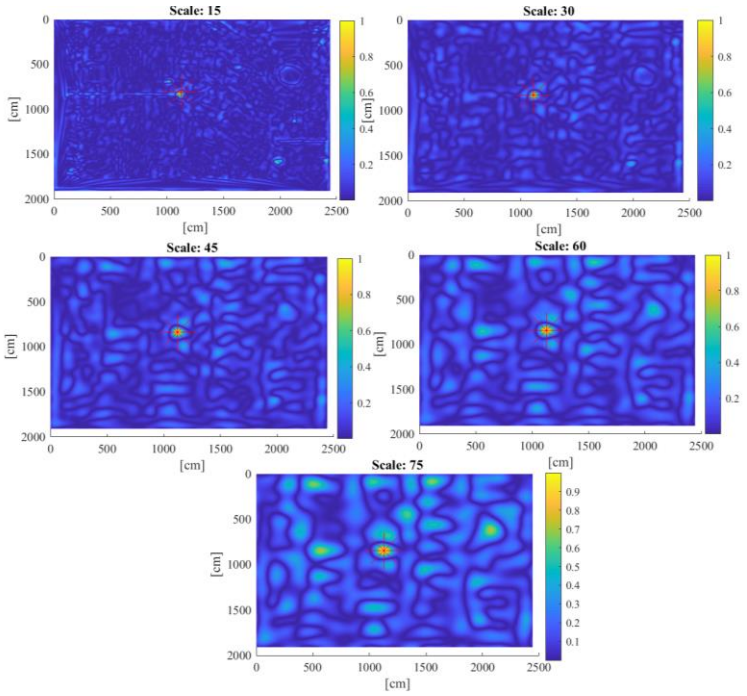

Figure A.1- 6 The coefficients obtained from the wavelet transformation corresponding to scales 15 (a), 30 (b), 45 (c), 60 (d) and 75 (e) are plotted on the map for the Magruder Hall slab. The areas in the slabs where undulations corresponding to these scales are present are shown. The peaks are marked in red. The scan is at scanning resolution 0.1°.

A.2: Magruder Hall Expansion Project:

Table A.2- 1 Peak detection results for Scan 2 (Magruder Hall Expansion Project) at scanning resolution 0.02°

Scales	Number of peaks correctly identified	Number of peaks incorrectly identified or failed to identify	Actual number of peaks (based on 0.01° scanning resolution)
15	**3**	**0**	**3**
30	**1**	**0**	**1**
45	**1**	**0**	**1**
60	**1**	**0**	**1**
75	**1**	**0**	**1**

Table A.2- 2 Peak detection results for Scan 2 (Magruder Hall Expansion Project) at scanning resolution 0.04°

Scales	Number of peaks correctly identified	Number of peaks incorrectly identified or failed to identify	Actual number of peaks (based on 0.01° scanning resolution)
15	**3**	**0**	**3**
30	**1**	**0**	**1**
45	**1**	**0**	**1**
60	**1**	**0**	**1**
75	**1**	**0**	**1**

Table A.2- 3 Peak detection results for Scan 2 (Magruder Hall Expansion Project) at scanning resolution 0.06°

Scales	Number of peaks correctly identified	Number of peaks incorrectly identified or failed to identify	Actual number of peaks (based on 0.01° scanning resolution)
15	**3**	**0**	**3**
30	**1**	**0**	**1**
45	**1**	**0**	**1**
60	**1**	**0**	**1**
75	**1**	**0**	**1**

Table A.2- 4 Peak detection results for Scan 2 (Magruder Hall Expansion Project) at scanning resolution 0.08°

Scales	Number of peaks correctly identified	Number of peaks incorrectly identified or failed to identify	Actual number of peaks (based on 0.01° scanning resolution)
15	**3**	**0**	**3**
30	**1**	**0**	**1**
45	**1**	**0**	**1**
60	**1**	**0**	**1**
75	**1**	**0**	**1**

Table A.2- 5 Peak detection results for Scan 2 (Magruder Hall Expansion Project) at scanning resolution 0.10°

Scales	Number of peaks correctly identified	Number of peaks incorrectly identified or failed to identify	Actual number of peaks (based on 0.01° scanning resolution)
15	**3**	**0**	**3**
30	**1**	**1**	**1**
45	**1**	**0**	**1**
60	**1**	**0**	**1**
75	**1**	**0**	**1**

Table A.2- 6 Peak detection results for Scan 1 and Scan 2 (Magruder Hall Expansion Project), each at scanning resolution 0.02°

Scales	Number of peaks correctly identified	Number of peaks incorrectly identified or failed to identify	Actual number of peaks (based on 0.01° scanning resolution)
15	**3**	**0**	**3**
30	**1**	**0**	**1**
45	**1**	**0**	**1**
60	**1**	**0**	**1**
75	**1**	**0**	**1**

Table A.2- 7 Peak detection results for Scan 1 and Scan 2 (Magruder Hall Expansion Project), each at scanning resolution 0.04°

Scales	Number of peaks correctly identified	Number of peaks incorrectly identified or failed to identify	Actual number of peaks (based on 0.01° scanning resolution)
15	**3**	**0**	**3**
30	**1**	**0**	**1**
45	**1**	**0**	**1**
60	**1**	**0**	**1**
75	**1**	**0**	**1**

Table A.2- 8 Peak detection results for Scan 1 and Scan 2 (Magruder Hall Expansion Project), each at scanning resolution 0.06°

Scales	Number of peaks correctly identified	Number of peaks incorrectly identified or failed to identify	Actual number of peaks (based on 0.01° scanning resolution)
15	**3**	**0**	**3**
30	**1**	**0**	**1**
45	**1**	**0**	**1**
60	**1**	**0**	**1**
75	**1**	**0**	**1**

Table A.2- 9 Peak detection results for Scan 1 and Scan 2 (Magruder Hall Expansion Project), each at scanning resolution 0.08°

Scales	Number of peaks correctly identified	Number of peaks incorrectly identified or failed to identify	Actual number of peaks (based on 0.01° scanning resolution)
15	**3**	**0**	**3**
30	**1**	**0**	**1**
45	**1**	**0**	**1**
60	**1**	**0**	**1**
75	**1**	**0**	**1**

Table A.2- 10 Peak detection results for Scan 1 and Scan 2 (Magruder Hall Expansion Project), each at scanning resolution 0.10°

Scales	Number of peaks correctly identified	Number of peaks incorrectly identified or failed to identify	Actual number of peaks (based on 0.01° scanning resolution)
15	**3**	**0**	**3**
30	**1**	**0**	**1**
45	**1**	**0**	**1**
60	**1**	**0**	**1**
75	**1**	**0**	**1**

A.3: Vista Logistics park project:

Table A.3- 1 Peak detection results for Scan 1 + Scan 2 (Vista Logistics Park Project) at scanning resolution 0.02°

Scales	Number of peaks correctly identified	Number of peaks incorrectly identified or failed to identify	Actual number of peaks (based on 0.01° scanning resolution)
15	**2**	**3**	**3**
30	**1**	**0**	**1**
45	**1**	**0**	**1**
60	**1**	**0**	**1**
75	**1**	**0**	**1**

Table A.3- 2 Peak detection results for Scan 1 + Scan 2 (Vista Logistics Park Project) at scanning resolution 0.04°

Scales	Number of peaks correctly identified	Number of peaks incorrectly identified or failed to identify	Actual number of peaks (based on 0.01° scanning resolution)
15	**1**	**3**	**3**
30	**1**	**0**	**1**
45	**1**	**0**	**1**
60	**1**	**0**	**1**
75	**1**	**0**	**1**

Table A.3- 3 Peak detection results for Scan 1 + Scan 2 (Vista Logistics Park Project) at scanning resolution 0.06°

Scales	Number of peaks correctly identified	Number of peaks incorrectly identified or failed to identify	Actual number of peaks (based on 0.01° scanning resolution)
15	**0**	**4**	**3**
30	**1**	**0**	**1**
45	**1**	**0**	**1**
60	**1**	**0**	**1**
75	**1**	**0**	**1**

Table A.3- 4 Peak detection results for Scan 1 + Scan 2 (Vista Logistics Park Project) at scanning resolution 0.08°

Scales	Number of peaks correctly identified	Number of peaks incorrectly identified or failed to identify	Actual number of peaks (based on 0.01° scanning resolution)
15	**0**	**4**	**3**
30	**1**	**0**	**1**
45	**1**	**0**	**1**
60	**1**	**0**	**1**
75	**1**	**0**	**1**

Table A.3- 5 Peak detection results for Scan 1 + Scan 2 (Vista Logistics Park Project) at scanning resolution 0.10°

Scales	Number of peaks correctly identified	Number of peaks incorrectly identified or failed to identify	Actual number of peaks (based on 0.01° scanning resolution)
15	**0**	**4**	**3**
30	**1**	**1**	**1**
45	**1**	**0**	**1**
60	**1**	**0**	**1**
75	**1**	**1**	**1**

Table A.3- 6 Peak detection results for Scan 1 + Scan 2 + Scan 4 (Vista Logistics Park Project) at scanning resolution 0.02°

Scales	Number of peaks correctly identified	Number of peaks incorrectly identified or failed to identify	Actual number of peaks (based on 0.01° scanning resolution)
15	**1**	**3**	**3**
30	**1**	**0**	**1**
45	**1**	**0**	**1**
60	**1**	**0**	**1**
75	**1**	**0**	**1**

Table A.3- 7 Peak detection results for Scan 1 + Scan 2 + Scan 4 (Vista Logistics Park Project) at scanning resolution 0.04°

Scales	Number of peaks correctly identified	Number of peaks incorrectly identified or failed to identify	Actual number of peaks (based on 0.01° scanning resolution)
15	**2**	**1**	**3**
30	**1**	**0**	**1**
45	**1**	**0**	**1**
60	**1**	**0**	**1**
75	**1**	**0**	**1**

Table A.3- 8 Peak detection results for Scan 1 + Scan 2 + Scan 4 (Vista Logistics Park Project) at scanning resolution 0.06°

Scales	Number of peaks correctly identified	Number of peaks incorrectly identified or failed to identify	Actual number of peaks (based on 0.01° scanning resolution)
15	**3**	**2**	**3**
30	**1**	**0**	**1**
45	**1**	**0**	**1**
60	**1**	**0**	**1**
75	**1**	**0**	**1**

Table A.3- 9 Peak detection results for Scan 1 + Scan 2 + Scan 4 (Vista Logistics Park Project) at scanning resolution 0.08°

Scales	Number of peaks correctly identified	Number of peaks incorrectly identified or failed to identify	Actual number of peaks (based on 0.01° scanning resolution)
15	**1**	**3**	**3**
30	**1**	**0**	**1**
45	**1**	**0**	**1**
60	**1**	**0**	**1**
75	**1**	**0**	**1**

Table A.3- 10 Peak detection results for Scan 1 + Scan 2 + Scan 4 (Vista Logistics Park Project) at scanning resolution 0.10°

Scales	Number of peaks correctly identified	Number of peaks incorrectly identified or failed to identify	Actual number of peaks (based on 0.01° scanning resolution)
15	**0**	**3**	**3**
30	**1**	**0**	**1**
45	**1**	**0**	**1**
60	**1**	**0**	**1**
75	**1**	**1**	**1**

Table A.3- 11 Peak detection results for Scan 1 + Scan 2 + Scan 3 + Scan 4 (Vista Logistics Park Project) at scanning resolution 0.02°

Scales	Number of peaks correctly identified	Number of peaks incorrectly identified or failed to identify	Actual number of peaks (based on 0.01° scanning resolution)
15	**3**	**0**	**3**
30	**1**	**0**	**1**
45	**1**	**0**	**1**
60	**1**	**0**	**1**
75	**1**	**0**	**1**

Table A.3- 12 Peak detection results for Scan 1 + Scan 2 + Scan 3 + Scan 4 (Vista Logistics Park Project) at scanning resolution 0.04°

Scales	Number of peaks correctly identified	Number of peaks incorrectly identified or failed to identify	Actual number of peaks (based on 0.01° scanning resolution)
15	**2**	**2**	**3**
30	**1**	**0**	**1**
45	**1**	**0**	**1**
60	**1**	**0**	**1**
75	**1**	**0**	**1**

Table A.3- 13 Peak detection results for Scan 1 + Scan 2 + Scan 3 + Scan 4 (Vista Logistics Park Project) at scanning resolution 0.06°

Scales	Number of peaks correctly identified	Number of peaks incorrectly identified or failed to identify	Actual number of peaks (based on 0.01° scanning resolution)
15	**3**	**2**	**3**
30	**1**	**0**	**1**
45	**1**	**0**	**1**
60	**1**	**0**	**1**
75	**1**	**0**	**1**

Table A.3- 14 Peak detection results for Scan 1 + Scan 2 + Scan 3 + Scan 4 (Vista Logistics Park Project) at scanning resolution 0.08°

Scales	Number of peaks correctly identified	Number of peaks incorrectly identified or failed to identify	Actual number of peaks (based on 0.01° scanning resolution)
15	**1**	**3**	**3**
30	**1**	**0**	**1**
45	**1**	**0**	**1**
60	**1**	**0**	**1**
75	**1**	**0**	**1**

Table A.3- 15 Peak detection results for Scan 1 + Scan 2 + Scan 3 + Scan 4 (Vista Logistics Park Project) at scanning resolution 0.10°

Scales	Number of peaks correctly identified	Number of peaks incorrectly identified or failed to identify	Actual number of peaks (based on 0.01° scanning resolution)
15	**0**	**4**	**3**
30	**1**	**1**	**1**
45	**1**	**0**	**1**
60	**1**	**0**	**1**
75	**1**	**1**	**1**